

2016-01-01

Geology, Geochemistry, and 3D Geological Modelling of the Independencia - Los Bancos Ag-Au Epithermal Vein Systems in the Palmarejo District, Chihuahua, Mexico

Arturo Ramirez

University of Texas at El Paso, art23ram@gmail.com

Follow this and additional works at: https://digitalcommons.utep.edu/open_etd



Part of the [Geochemistry Commons](#), and the [Geology Commons](#)

Recommended Citation

Ramirez, Arturo, "Geology, Geochemistry, and 3D Geological Modelling of the Independencia - Los Bancos Ag-Au Epithermal Vein Systems in the Palmarejo District, Chihuahua, Mexico" (2016). *Open Access Theses & Dissertations*. 928.
https://digitalcommons.utep.edu/open_etd/928

This is brought to you for free and open access by DigitalCommons@UTEP. It has been accepted for inclusion in Open Access Theses & Dissertations by an authorized administrator of DigitalCommons@UTEP. For more information, please contact lweber@utep.edu.

GEOLOGY, GEOCHEMISTRY AND 3D GEOLOGICAL MODELLING OF
THE INDEPENDENCIA – LOS BANCOS AG-AU EPITHERMAL VEIN
SYSTEMS IN THE PALMAREJO DISTRICT,
CHIHUAHUA, MEXICO

ARTURO RAMIREZ

Master's Program in Geological Sciences

APPROVED:

Philip C. Goodell, Ph.D., Chair

Mark A. Engle, Ph.D.

William X. Chavez, Ph.D.

Charles Ambler, Ph.D.
Dean of the Graduate School

Copyright ©

by

Arturo Ramirez

2016

Dedication

Le dedico esta tesis a mis padres, muchos de mis logros se los debo a ustedes, incluyendo esta Maestría; a mi familia y a todos los que me han apoyado; finalmente a Yvette Pereyra por brindarme su apoyo incondicional y compañía a lo largo de este proyecto.

GEOLOGY, GEOCHEMISTRY AND 3D GEOLOGICAL MODELLING OF
THE INDEPENDENCIA – LOS BANCOS AG-AU EPITHERMAL VEIN
SYSTEMS IN THE PALMAREJO DISTRICT,
CHIHUAHUA, MEXICO

by

ARTURO RAMIREZ, B.S.

THESIS

Presented to the Faculty of the Graduate School of
The University of Texas at El Paso
in Partial Fulfillment
of the Requirements
for the Degree of

MASTER OF SCIENCE

Department of Geological Sciences
THE UNIVERSITY OF TEXAS AT EL PASO

May 2016

Acknowledgements

I would like to thank The Department of Geological Sciences, especially my advisor Dr. Philip Goodell for his guidance and support in this project and instilling in me his passion for the mineral deposits of Chihuahua, Dr. Mark A. Engle for providing guidance in the statistical analysis aspects and forming part of this graduate committee, Dr. William X. Chavez, whom I met in a field trip to Northern Chile and accepted to be my outside committee member. I also want to thank Dr. Munazzam Ali Mahar for providing guidance through various important aspects of this project, Liza Ortega and Manuel Moncada, who aided in the sample collection phase. I want to express my gratitude to Castulo Molina and Enrique Fuentes for their invaluable support providing data, the Coeur Mining Inc. Exploration Department for their willingness in sharing their insights, and Yenlai Chee for her assistance in the geologic modelling aspects of this project.

Abstract

The Sierra Madre Occidental (SMO) is a Cretaceous-Tertiary silicic ignimbrite province in northwestern Mexico. It is the result of tectonic and magmatic events produced by the subduction of the Farallon plate under North America (80-40 Ma) and the opening of the Gulf of California (14-12 Ma), thus forming the SMO metallogenic provinces. The Late Eocene to Oligocene was a major period of metallic mineralization hosting various deposit types, principally Ag-Au (\pm Pb-Zn-Cu) epithermal veins, which have been economically significant.

The study area lies in the Palmarejo district, operated by Coeur Mining Inc., which was the world's fifth largest silver producer in 2013. Coeur Mining Inc. increased its resources with the acquisition of Paramount Gold and Silver Corp. as they shared property boundaries where the Independencia deposit is contiguous to the Don Eze deposit. Currently, mining activities are increasing in the Independencia deposit.

It is important to understand the geochemical characteristics, sources, transport mechanisms, and depositional controls of mineralizing fluids for the application of mineral exploration. This study aims to provide new insights about the metallogenesis in this region by analyzing the: 1) geochemistry, 2) timing and origin of the ignimbrites (UVS) by providing zircon U-Pb ages and ϵ Hf (t) compositions by LA-ICP-MS, 3) statistical results of multi-element geochemical drill core data from the Independencia epithermal system, and 4) construct a 3D geological model of the Independencia – Los Bancos Ag-Au epithermal vein systems to evaluate the deposit and metal distributions.

Recent studies in the northwest SMO have shown evidence which indicate that the Late Oligocene and Early Miocene volcanic activity, which produced the ignimbrite flare-up (UVS) is largely syn-genetic with the post-Laramide Tertiary extension. The U-Pb geochronological data

in this study record ages at ~ 28 Ma in the San Francisco area and at ~ 23 Ma in the Guerra Al Tirano and Guadalupe Norte areas. The $\epsilon_{\text{Hf}}(t)$ compositions varying from -0.6 to +7.8 are indicative that the origin of magmas which generated large volumes of silicic volcanic rocks may have been evolved from mantle derived sources and mixing between sub-continental lithospheric mantle (SCLM) and evolved non-radiogenic crustal fluids, possibly stemming from the widespread hydrothermal activity associated to epithermal mineralization.

The extensional periods in northwest Mexico provided the framework for the shallow emplacement of Ag-Au \pm (Pb, Zn, Cu) epithermal vein deposits along NW-SE structural trends. The extensional fractures served as the migration paths for the ore fluids and eventual deposition. The mineralization age at the Independencia – Los Bancos deposit is determined to be ~ 23 Ma on the basis of the cross-cutting relationships between the mineralized veins and the district rhyolitic porphyry bodies, domes and dykes of similar origin. The statistical treatments conducted in this study show comparable results which revealed ore fluid characteristics of an intermediate-sulfidation epithermal deposit. The mineral assemblages of silver sulfosalts, electrum, sphalerite, are distinguished by the high proportional relationships between Ag-Au and Pb-Zn. The ore mineralogy of an intermediate-sulfidation epithermal deposit is partly controlled by the ore fluid composition and salinities ranging from 3.5 to 7.5 wt. % NaCl equivalent. Salinities of ore fluids observed in the Palmarejo district range from 1.3 to 7.8 wt. % NaCl equivalent. The geologic model aids to visualize the geometry of the deposit and observe the variability and distribution of precious metals which has many implications for exploration and mining.

Table of Contents

| | |
|--|------|
| Acknowledgements | v |
| Abstract | vi |
| Table of Contents | viii |
| List of Tables | x |
| List of Figures | xi |
| List of Illustrations | xiv |
| 1. Introduction | 1 |
| 1.1 Statement of the Problem | 3 |
| 1.2 Research Objectives | 3 |
| 2. Background | 4 |
| 2.1 Location | 4 |
| 2.1.1 Access | 4 |
| 2.1.2 Climate | 4 |
| 2.1.3 History | 5 |
| 2.2 About the Company | 5 |
| 2.3 Previous Studies | 6 |
| 2.4 Regional Geologic and Tectonic Framework | 8 |
| 2.4.1 Magmatism | 9 |
| 2.4.2 Tectonism | 10 |
| 2.5 Regional Metallogeny | 11 |
| 2.6 Palmarejo District Geology | 11 |
| 2.6.1 Independencia – Los Bancos Geology | 13 |
| 3. Methodology | 15 |
| 3.1 Sample Collection and Data Acquisition | 15 |
| 3.2 Igneous Petrology and Geochemistry | 15 |
| 3.3 Geochronology and Isotopic Signatures | 16 |
| 3.3.1 Sample Preparation and Processing | 16 |
| 3.3.2 Analytical Methods | 18 |

| | | |
|-------|---|-----|
| 3.4 | Statistical Data Analysis | 18 |
| 3.4.1 | Statistical Data Treatment..... | 18 |
| 3.4.2 | Data Analysis Methods | 19 |
| 3.5 | Geological Modelling | 20 |
| 3.5.1 | Geologic Model | 21 |
| 3.5.2 | Interpolation Models | 22 |
| 4. | Data | 24 |
| 4.1 | Igneous Petrology and Geochemistry | 24 |
| 4.1.1 | Rock Classifications Using Major Element Data | 24 |
| 4.1.2 | Rock Discriminations Using Trace Element Data | 25 |
| 4.2 | Geochronology and Isotopic Signatures | 26 |
| 4.2.1 | Zircon U-Pb Ages of Ignimbrites | 26 |
| 4.2.2 | Zircon $\epsilon\text{Hf}(t)$ compositions | 27 |
| 4.3 | Statistical Data Analysis | 28 |
| 4.3.1 | Univariate Analysis..... | 28 |
| 4.3.2 | Bivariate Scatterplot Matrix..... | 29 |
| 4.3.3 | Multivariate Treatment | 29 |
| 4.4 | Geological Model..... | 31 |
| 4.4.1 | Metal Distribution..... | 32 |
| 5. | Discussion | 34 |
| 5.1 | Previous Understanding of the Ignimbrite Flare-up and Related Tectonism | 34 |
| 5.2 | Timing of The Ignimbrite Flare-Up in the Palmarejo District..... | 35 |
| 5.3 | Origin of Magmas | 36 |
| 5.4 | Tectonic Implication | 38 |
| 5.5 | Timing of Epithermal Mineralization in Northern Mexico | 38 |
| 5.5.1 | Geochemical Processes | 41 |
| 6. | Conclusion | 43 |
| | References | 45 |
| | Vita..... | 109 |

List of Tables

| | |
|---|----|
| Table 1. List of studied samples and type of analyses performed..... | 54 |
| Table 2. Major and trace element geochemical analysis by the Fusion ICP/MS methodology at Activation Laboratories Ltd. | 55 |
| Table 3. Summary statistics of untransformed geochemical assay data from the Independencia vein. MIN - Minimum; Q0.05 - 5% quartile; Q1 - 1st quartile; MED - median; Q3 - 3rd quartile; Q0.95 - 95% quartile; SD - standard deviation; MAD - median absolute deviation; IQR- interquartile range; MAX - maximum. | 56 |
| Table 4 – A-D. Variation matrices of centered-log ratio (clr) transformed geochemical assay data from the Independencia deposit to investigate proportional relationship between variables (Reimann et al., 2008)..... | 57 |
| Table 5. U-Pb age data and ϵHf (t) compositions summary table..... | 58 |

List of Figures

| | |
|---|----|
| Figure 1. Correlation between temperature and sulfur fugacity for the sulfidation states related to hydrothermal fluids in the porphyry and epithermal domains, defined by stability fields of key minerals. Modified from Einaudi et al., (2003). Sulfur relationships are taken from Barton and Skinner (1979). | 59 |
| Figure 2. Comparative scheme (not to scale) of the structure, processes, alteration types, released volatiles, temperatures, pH, types of fluids and reactions involved in the formation of acidic (high sulfidation) and alkaline (low and intermediate sulfidation) epithermal deposits, and their relationship with magmatic rocks as the source of heat, fluids and chemical components for these deposits, from a magmatic chamber in a cooling process, leading to the formation of metallic deposits related to porphyries (Cu-Au-Mo), up to the epithermal environment (modified from Sillitoe, 1995a; based on data from Hedenquist and Lowenstern, 1994; Gammons y Williams-Jones, 1997; Corbett and Leach, 1998). The brittle-ductile transition boundary is placed at ~400 ⁰ C and at 5-7 km depth (i.e. Fournier, 1991; Nielson et al., 1999). | 60 |
| Figure 3. Distribution map of epithermal-type deposits in Mexico in a NW trending metallogenic belt (modified from Camprubi and Albinson, 2007). | 61 |
| Figure 4. Location map of study area in the Palmarejo District, Chihuahua, Mexico in relation to major cities in the state of Chihuahua and highway networks (INEGI, 2005). | 62 |
| Figure 6. Geographic extent map of the Sierra Madre Occidental in northwestern Mexico and its southern intersection with the Trans-Mexican Volcanic Belt (modified from McDowell and Keizer, 1977; Bryan at al., 2008). | 64 |
| Figure 7. Regional stratigraphic profile of the northern SMO and rock constituents of the UVS (Upper Volcanic Supergroup) and LVS (Lower Volcanic Supergroup) (modified from Ferrari et al. 2007). The UVS and LVS are terms introduced by McDowell and Keizer (1977). | 65 |
| Figure 8. Tectono-stratigraphic terrane map of Mexico in relation to the Sierra Madre Occidental (modified from Sedlock et al., 1993). Red star – Palmarejo district. <i>CUI</i> – <i>Cuicateco Terrane</i> ; <i>M</i> – <i>Mixteco Terrane</i> ; <i>TMVB</i> – <i>Trans-Mexican Volcanic Belt</i> ; <i>Z</i> – <i>Zapoteco Terrane</i> | 66 |
| Figure 9. Geographic extent map of the Tertiary ignimbritic pulses in northwestern Mexico underlain by Cretaceous volcanic and plutonic rocks (modified from Ferrari et al., 2007). Red star –Palmarejo district. | 67 |
| Figure 10. Regional tectonic setting of northwestern Mexico showing the transtensional plate boundary of the Gulf of California along with the geographical extent of the Basin and Range and Gulf extensional provinces (modified from Parsons, 1995; Ferrari et al., 2007; Alvarez et al., 2009). | 68 |
| Figure 11. Structural trend map of the Chihuahua-Sonora-Sinaloa border region showing structural lineaments interpreted as the boundaries of pull-apart basins with the Palmarejo and Sauzal mines as reference (modified from the Servicio Geológico Mexicano, 2015). | 69 |
| Figure 12. Distribution map of metallic mineralization related to porphyry, epithermal and carbonate replacement deposits in Mexico in relationship to the Cretaceous plutonic intrusions associated to the Laramidic magmatic arc (modified from Clark and Fitch, 2009; Ortega-Gutierrez et al., 2014) | 70 |
| Figure 13. Palmarejo District regional geologic map (modified from the Servicio Geológico Mexicano, 2015). | 71 |
| Figure 14. Stratigraphic section of the Palmarejo district lithologic units (Kerr et al., 2015). | 72 |

| | |
|---|----|
| Figure 15. Geologic and alteration map of the Los Bancos – Independencia epithermal vein deposits. | 73 |
| Figure 16. Regional fluid inclusion map of the Palmarejo district showing homogenization temperatures and salinities of significant quartz-veins (Miller, 1988 (red box); Galvan-Gutierrez, 2012 (green boxes)). | 74 |
| Figure 17. Location map of studied samples from the Palmarejo district. | 75 |
| Figure 18. Location map of drill-holes provided by Coeur Mining Inc. from the Los Bancos – Independencia deposits. | 76 |
| Figure 19. Photos of studied samples with sample identification as reference.*Geochronology and isotopic analyses..... | 77 |
| Figure 20 – A-C. Major element variation diagrams..... | 79 |
| Figure 20 – D-F. Major element variation diagrams. | 80 |
| Figure 20 – G-I. Major element variation diagrams. | 81 |
| Figure 21. Total Alkali-Silica diagram showing volcanic rock classifications of samples from the Palmarejo district (LeBas et al., 1986)..... | 82 |
| Figure 22. Alkaline and sub-alkaline magma series classification diagram based on major element concentrations in samples from the Palmarejo district (Irvine and Barragar, 1971)..... | 83 |
| Figure 23. Feldspathic igneous rock classification diagram based on major element concentrations in samples from the Palmarejo district (Frost and Frost, 2008). | 84 |
| Figure 24. Altered volcanic island rock discrimination diagram based on trace element concentrations in samples from the Palmarejo district (Hastie et al., 2006)..... | 85 |
| Figure 25. Tectonic setting discrimination diagram based on trace element concentrations in samples from the Palmarejo district (Pearce et al., 1984)..... | 86 |
| Figure 26 – A-C. U-Pb Tera-Wasserburg plots and weighted mean age plots for the Guerra Al Tirano samples. | 87 |
| Figure 26 – D-E. U-Pb Tera-Wasserburg plots and weighted mean age plots for the San Francisco (SF1) and Guadalupe Norte (GPN2) samples. | 88 |
| Figure 27 – A-F. Weighted mean $\epsilon_{\text{Hf}}(t)$ compositions of the Guerra Al Tirano (GAT1, GAT2, and GAT3), San Francisco (SF1), Guadalupe Norte (GPN2) and all Palmarejo ignimbrites samples..... | 89 |
| Figure 28. Epsilon Hf (t) against age plot of Palmarejo samples. <i>DM – depleted mantle; CHUR – chondritic undepleted reservoir.</i> | 90 |
| Figure 29 – A-B. Univariate density histograms, one-dimension density plots and box plots for Ag and As logit transformed concentration data (Reimann et al., 2008). | 91 |
| Figure 29 – C-D. Univariate density histograms, one-dimension density plots and box plots for Au and Ba logit transformed concentration data (Reimann et al., 2008). | 92 |
| Figure 29 – E-F. Univariate density histograms, one-dimension density plots and box plots for Cu and Fe logit transformed concentration data (Reimann et al., 2008). | 93 |
| Figure 29 – G-H. Univariate density histograms, one-dimension density plots and box plots for Mn and Pb logit transformed concentration data (Reimann et al., 2008). | 94 |
| Figure 29 – I-J. Univariate density histograms, one-dimension density plots and box plots for Sb and Zn logit transformed concentration data (Reimann et al., 2008). | 95 |
| Figure 30. Ten variable scatterplot correlation matrix for logit transformed geochemical assay data from the Independencia vein (Reimann et al., 2008). Red color represents mineralized bodies, green color the rhyolitic porphyry, blue color the andesitic porphyry and purple color andesitic rocks..... | 96 |

| | |
|---|-----|
| Figure 31 – A-D. Robust Principal Component Analysis (PCA) compositional biplots of centered-log ratio (clr) transformed assay data from the Independencia deposit showing loading vectors (arrows) and scores (gray + signs) (Reimann et al., 2008). A. – mineralized structures. B. rhyolitic rocks. C. andesitic rocks. D. andesitic porphyry. | 97 |
| Figure 32 – A-D. Dendrograms for hierarchical cluster analysis of the Independencia vein (Reimann et al., 2008). A. – mineralized structures (EM). B. rhyolitic rocks (RHYO). C. andesitic rocks (ANDE). D. andesitic porphyry (Ktap). | 98 |
| Figure 34. Independencia Ag and Au Interpolation Model, looking SW. | 100 |
| Figure 35. Los Bancos Ag and Au Interpolation Model, looking NE. | 101 |
| Figure 36. Total Alkali-Silica diagram (after LeBas et al., 1986) showing volcanic rock classifications of samples from the Palmarejo district (red squares). The field of the Sierra Guazapares and Temoris Formation ignimbrites, based on Figure 7 of Murray et al., (2013), is included as a reference (blue dashed line). The field of the main Sierra Madre Occidental rocks, based on Figure 3A of McDowell (2007) is also included (black dashed line). | 102 |
| Figure 37. Age data map and $\epsilon\text{Hf}(t)$ across the Palmarejo and Guazapares mining districts (red boxes – this study). Age data from Galvan-Gutierrez (2012) (blue boxes) and Murray et al. (2013) (green boxes). | 103 |
| Figure 38. Slab roll-back schematic model for extension, asthenospheric upwelling, partial melting of the sub-continental lithospheric mantle (SCLM) and differentiation of basaltic magma to generate the ignimbrite flare-up. | 104 |
| Figure 39. Cross-section of the Independencia – Los Bancos showing cross-cutting relationships of the rhyolitic porphyry (ToPr) with respect to the Independencia and Los Bancos veins. <i>STWK</i> – stockwork; <i>EM</i> – mineralized structures; <i>ToPr</i> – porphyritic rhyolite; <i>Ktat</i> – lithic andesites; <i>Ktap</i> – porphyritic andesite; <i>Ktam</i> – amygdular basaltic andesites; <i>Ktal</i> – laminar andesites. | 105 |
| Figure 40. Stratigraphic column correlation between the Guazapares and Palmarejo district suggesting the Upper Volcanic Supergroup (UVS) as the host rock for mineralization based on zircon U/Pb age data from Murray et al. (2013). | 106 |

List of Illustrations

| | |
|---|-----|
| Illustration 1. Sample processing steps for zircon extraction. 1) outcrop selection, 2) sampling fresh rock, 3) cutting sample, 4) crushing rock, 5) 500 μm mesh sieve, 6) gravity separation, 7) magnetic mineral separation, and 8) heavy-liquid separation. | 107 |
| Illustration 2. LaserChron laboratory of the University of Arizona. Laser Ablation Induced Coupled Plasma Mass Spectrometry (LA-ICP-MS) analytical instrument. 1) laser beam focused on the sample surface to generate fine particles, 2) ablated particles are then transported to the secondary excitation source of the ICP-MS instrument for digestion and ionization of the sampled mass. The excited ions in the plasma torch are subsequently introduced to a mass spectrometer detector for both elemental and isotopic analysis. | 108 |

1. Introduction

Mineral exploration is the process of finding ore by the application of remote sensing, geological, geophysical and geochemical methods in order to investigate the minerals or elements of interest. An ideal approach to mineral exploration may involve analyzing satellite imagery to make interpretations of possible targets. When a target is identified, geophysical methods are then used to define any geophysical anomalies at the exploration site. The following stage involves a geochemical survey of outcrop, soil, and stream sediment samples to find areas anomalous in the commodity of interest, or in elements associated with a specific deposit type. Anomalous concentrations of elements of interest or pathfinder elements then have to be drilled in order to test for the existence of economic mineralization (Moon, 2006). Drilling programs return large geochemical data sets that require further analysis to make interpretations of geochemical processes. Core logging is then used to measure and record as much information from the cylindrical rock drilled to determine the lithology, mineral and alteration assemblages, vein cross-cutting relationships and structures from the potential deposit. All this geological knowledge may be integrated to produce a 3D geological model of the deposit. Resource estimation and mining strategy are determined by having a clear understanding of the 3D geometry and metal distribution within an ore body. Therefore, a successful exploration campaign is conducted by integrating various analyses to adequately assess an ore body. Determining the tectonic setting is also important as the origin of ore deposits directly relates to the regional volcano-tectonic evolution.

It is generally accepted that epithermal deposit types are associated with subduction-related arc terranes (Sawkins, 1972). However, a few epithermal deposits are associated to post-subduction extensional regimes characterized locally by bimodal volcanism (Sillitoe, 1977;

Sillitoe and Hedenquist, 2003). Since the early recognition of volcanic-hosted epithermal deposits there have been many schemes to classify them. These classification schemes are based on dominant elements and minerals (Emmons, 1918). Further studies in deposit style variations, from tectonic setting to mineralogy (e.g., Bogie and Lawless, 1987; White et al., 1995; Einaudi et al., 2002), led to the identification of three environments, based on sulfidation state, where hypogene sulfide assemblages occur (Figure 1). The three epithermal environments include high-sulfidation, intermediate-sulfidation, and low-sulfidation types, as introduced by Hedenquist (1987) and Hedenquist et al. (2000). Figure 2 shows a schematic comparison of the structure and processes involved in the formation of epithermal type deposits.

Epithermal deposits in Mexico are mostly of Tertiary age (Albinson et al., 2001; Camprubi et al., 2003; Clark and Fitch, 2009) and have a close relationship with the continental arc volcanism of the SMO silicic ignimbrite province (Staude and Barton, 2001). The majority of epithermal deposits in Mexico belong to the intermediate- or low-sulfidation deposit types with a few occurrences of the high-sulfidation type (Camprubi and Albinson, 2007) (Figure 3). Moreover, an empirical reclassification by Camprubi and Albinson (2007) grouped deposits that show a combination of characteristics, in time and space, of both the low- and intermediate-sulfidation types, and in some cases the high-sulfidation type. The most common mineralization style of the Mexican epithermal deposits includes dominant low-sulfidation characteristics but have polymetallic (Zn-Pb-Cu) intermediate-sulfidation roots (Camprubi and Albinson, 2007). This is the mineralization style observed across the Palmarejo district where the main mineral deposits are dominated by polymetallic silver-gold mineralization. This study focuses on the geological relationship between the Independencia and the Los Bancos intermediate-sulfidation

epithermal deposits in the Palmarejo district and the regional tectonic setting, of these deposits, in the Sierra Madre Occidental (SMO) in southwest Chihuahua, Mexico (Figure 4).

1.1 STATEMENT OF THE PROBLEM

The motivation for this Master's thesis research project is to better understand the geochemical processes involved in the formation of epithermal vein type deposits in southwest Chihuahua. It is important to understand the geochemical characteristics, sources, transport mechanisms, and depositional controls of mineralizing fluids for the application of mineral exploration. This study aims to evaluate the Independencia and the Los Bancos Ag-Au intermediate-sulfidation epithermal vein deposits in the Palmarejo district to provide new insights about the metallogensis in this region. Southwest Chihuahua is an area with limited geologic knowledge, very rich in precious metals, and with a great potential for exploration, discovery and mining.

1.2 RESEARCH OBJECTIVES

The objectives of this research project are to analyze the: 1) igneous petrology and geochemistry, 2) timing and origin of the ignimbrites (UVS) by providing zircon U-Pb age and ϵHf (t) compositions by LA-ICP-MS, 3) statistical results of multi-element geochemical drill core data from the Independencia epithermal system, and 4) construct a 3D geological model of the Independencia – Los Bancos Ag-Au epithermal vein systems to evaluate the deposit and metal distributions.

2. Background

2.1 LOCATION

The study area is located in the Coeur Mining Inc. Palmarejo property, latitude $27^{\circ} 23'N$, longitude $108^{\circ} 24'W$, in the state of Chihuahua, Mexico, within the Temoris and Guazapares mining districts of northern Mexico. The study area sits on the western margin of the Sierra Madre Occidental physiographic province and within the Chihuahuan Great Plateaus and Canyons sub-province (Figure 5). The main drainage features of this sub-province are the Urique Canyon, the Batopilas Canyon, and the Sinforosa Canyon, as well as the Otero River, the Chinipas River, and the Septentrion River (INEGI, 2005).

2.1.1 Access

The Palmarejo district is 420 km southwest of the capital city of Chihuahua, and 15 km northwest of the town of Temoris. It can be accessed from the city of Chihuahua via state highway 16, the road to Creel, the road to Bahuichivo and the road to Temoris, or by the Chihuahua-Pacific Railway, also known as El Chepe, which departs from the city of Chihuahua to the city of Los Mochis, Sinaloa making a stop in the town of Temoris (Figure 3).

2.1.2 Climate

This region has a temperate, sub-humid climate. The average minimum temperature is $10^{\circ}C$ and the maximum temperature is $34^{\circ}C$. Annual rainfall is approximately 800 to 1100 mm, with most rainfall between the months of July and September. Vegetation is mainly forests. The dominant soil type is a regosol. Land use is dominated by small-scale subsistence farming (INEGI, 2005).

2.1.3 History

Mining activities in the Palmarejo district date back to the early 17th century. The oldest production information comes from 1886 when the English Palmarejo company and Mexican Goldfields Limited acquired the mine. Since then, the district has seen intermittent exploration and mining activities. In 1964 the Mexican company Minas de Uruapa S.A. acquired the mine but did not see production until 1985 (Masterman et al., 2005). Minera Tecpan S.A. de C.V., operated by Jim Patterson, a UTEP alumni, was in operation since 1985, where the production came from high silica precious-metal ore from the Llanitos deposit. The Australian company Bolnisi Gold NL began exploring in 2003, leading to the discovery of new Ag-Au resources at Palmarejo, Guadalupe and La Patria (Galvan-Gutierrez, 2012). Coeur Mining Inc. acquired Bolnisi Gold NL in 2007, and continued to develop the Palmarejo mine. The mine became the world's fifth largest silver producer in 2013, making it a world-class silver producer. Currently, mining activities in the Palmarejo district are transitioning to Guadalupe. Coeur Mining's Inc. acquisition of Paramount Gold and Silver Corp. began in 2014 as they share property boundaries where the Independencia deposit is contiguous to the Don Eze deposit. Once the merger of both companies was completed in 2015, the vein retained the name of Independencia (News Release, 2014)

2.2 ABOUT THE COMPANY

The company started with the name of Coeur d'Alene Mines in 1928 from where they mined near Coeur d'Alene, Idaho, USA. Since then it has been in the business of mining precious metals. The company changed its name to Coeur Mining Inc. in 2013. Currently, it operates in the US, Mexico, Bolivia, and Australia and has feasibility stage projects in Mexico,

and Argentina. The 2015 production results were 15.9 million ounces of silver and 327,908 ounces of gold totaling 35.6 million ounces of silver equivalent, making it the largest US-based primary silver producer and a significant gold producer (Coeur Mining Inc., <http://www.coeur.com>).

2.3 PREVIOUS STUDIES

Previous studies in the Palmarejo district and adjacent properties include regional scale mapping and stream sediment sampling conducted by the *Servicio Geológico Mexicano* (SGM), as well as exploration reports and mining feasibility studies completed by Minera Tecpan, Bolnisi Gold NL, Coeur Mining, and Paramount Gold & Silver. In addition, other authors have dedicated time and effort to further understand the metallogensis, magmatism, and crustal deformation of the SMO.

Miller (1988) mapped and described the deposits in the Llanitos district, constructed rough models for the tectonism of the SMO and emplacement of associated magma and mineralization, and identified areas of high grade mineralization by conducting metal ratio analyses. She found that metal zoning, with respect to the dacite porphyry intrusive body in the district, increases to the west of the porphyry where she observed an increase in log Ag/log Au ratios along fissure-veins in the Llanitos district. She determined homogenization temperatures of fluid inclusion from the Sulema ore shoot and found three temperatures of fluids active during mineralization – 173 to 180°C, 200 to 210°C, 240 to 244°C, suggesting evidence for boiling. In addition, she proposed a genetic model for emplacement of vein mineralization.

Dr. Richard H. Sillitoe (2010), along with personnel from Coeur Mining Inc., examined key open-pit, underground, and surface exposures, as well as representative drill core from the Palmarejo district. He advised and offered recommendations on ore-forming and supergene

processes. He identified characteristics of advanced argillic alteration in the Espinazo Del Diablo zone and advised to define the full extent of the lithocap as it implies the possibility for high-sulfidation mineralization in the region.

A more detailed understanding of the Ag-Au deposits in the Palmarejo district was provided by Galvan-Gutierrez (2012). He identified three major stages of vein- and breccia-hosted mineralization by examining vein stratigraphy and paragenesis, spatial and temporal distribution of alteration assemblages, composition and evolution of mineralizing fluids, and sulfide trace element mineral chemistry. Fluid inclusions in quartz had homogenization temperatures from ranging from 236 to 366⁰C and salinities from 0.5 to 6.6 wt. percent NaCl equivalent in the Palmarejo vein. Fluid inclusions in quartz had homogenization temperatures ranging from 226 to 389⁰C and salinities from 3.0 to 7.6 wt. percent NaCl equivalent in the Guadalupe vein. Fluid inclusions in quartz had homogenization temperatures ranging from 222 to 348⁰C and salinities from 3.5 to 7.0 wt. percent NaCl equivalent. The temperature and salinity ranges include different stages of mineralization where Stage 1 and 3 provided evidence for fluid mixing, whereas results from Stage 2 were consistent with a boiling scenario.

To the east of the Palmarejo project lies the Guazapares mining district where Murray et al. (2013) present evidence for synvolcanic crustal extension from the Guazapares fault zone. Three synextensional formations were identified in the district and extensional faulting is interpreted as part of a regional-scale Middle Eocene to Early Miocene southwestward migration of active volcanism and extension in the northern SMO. Murray and Busby (2015) show that epithermal mineralization in the Guazapares district is controlled by synextensional magmatism.

2.4 REGIONAL GEOLOGIC AND TECTONIC FRAMEWORK

The study area lies within the SMO, a Cretaceous to Tertiary silicic ignimbrite province in northwestern Mexico (McDowell and Keizer, 1977; Bryan et al., 2008) (Figure 6). It is the result of tectonic and magmatic events produced by the subduction of the Farallon plate under North America (80-40 Ma) and the opening of the Gulf of California (14-12 Ma), thus forming the SMO metallogenic provinces (Ferrari et al., 2007). The SMO covers an area of 200 to 500 km wide by more than 2000 km long. It extends from the US-Mexico border to its intersection with the Trans-Mexican Volcanic Belt. McDowell and Keizer (1977) divided the SMO into two lithological groups – the Lower Volcanic Supergroup (LVS) and the Upper Volcanic Supergroup (UVS). The regional stratigraphic sequence provided by Ferrari et al. (2007) is composed of Upper Cretaceous to Miocene crustal granodioritic batholiths, Cretaceous to Paleocene andesites designated to the LVS, and Eocene to Miocene rhyolitic ignimbrites assigned to the UVS (Figure 7). The region corresponds to the tectono stratigraphic Guerrero terrane described by Campa and Coney (1983). In the interpretation by Sedlock et al., (1993), the region is located at the boundary of the Seri and Tahoe terranes (Figure 8). The terrain boundaries have been changed and a new interpretation by Centeno-Garcia et al. (2003) places the study area in the Cortes Terrain. The Cortes Terrain is composed of Precambrian basement rocks overlain by Early Cretaceous sedimentary rocks of the Bisbee Group (González-Leon et al., 2000). This group is composed of the Morita Formation, Mural Limestone Formation, and Cintura Formation. This study will refer to the interpretation by Sedlock et al. (1993).

2.4.1 Magmatism

Ferrari et al. (2007) have recognized five magmatic and tectonic events during the Late Cretaceous to the Paleocene (Figure 9). The first event during this period was caused by the Laramide arc magmatism which produced plutonic and volcanic rocks with ages between 90 to 40 Ma (Damon et al., 1983), dominated by andesitic lavas grouped into the LVS. The first ignimbritic pulse took place during the Eocene, which began at 46 Ma and continued until 42 Ma. (McDowell and McIntosh, 2012). The next events were the Oligocene to Early Miocene ignimbritic pulses which were significant volcanic episodes that produced large volumes over a great extend in a relatively short period of time. This thick sequence of rhyolitic ignimbrites, air-fall tuffs, silicic to intermediate lavas, and lesser mafic lavas are group into the UVS, which is unconformably emplaced on top of the LVS (McDowell and Keizer. 1977). There were periods of magmatism characterized by bimodal and discontinuous volcanism after each ignimbritic episode (Figure 9). The ages of these rocks range from 33 to 17.6 Ma (Cameron et al., 1989). The magma sources of the Late Cretaceous to Tertiary batholiths remains controversial with regard to the contributions of mantle versus crustal melts in the final emplacement of the batholiths (e.g. Best and Christiansen, 1991; Ward, 1991; Bohannon and Parsons, 1995; Dickinson, 2002; McQuarrie and Oskin, 2010). However, insights from whole rock Sr and Nd isotope compositions suggest both, fractional crystallization of mantle magmas and partial melting of Proterozoic to Mesozoic crust, as the source of the silicic magmas, primarily in the mantle wedge above the Farallon plate (Mahar, 2015).

2.4.2 Tectonism

The compressional deformation structures in the SMO are not apparent due to the intense normal faulting from different episodes of extensional deformation between the Oligocene and the Eocene (Ferrari et al., 2007). However, Henry et al. (2003) recognized foliated rocks from pre-, syn-, and post-tectonic plutons in Sinaloa that were deformed between 101 and 89 Ma. According to McDowell and Mauger (1994) the transition from a compressional to extensional regime occurred at or before approximately 33 Ma, which was recorded by the first occurrences of peralkaline ignimbrites and transitional basalts. The Basin and Range province extends from the western US into Mexico. The broadest stage of extensional deformation in the southern Basin and Range province took place during the middle Miocene at about 13 Ma (Parsons, 1995). The opening of the Gulf of California accompanied normal faulting in Mexico from about 12 to 10 Ma (Stock and Hodges, 1989). Basin and Range deformational structures such as block faulting are widespread in Chihuahua. In contrast, extension in Sonora was more intense causing metamorphic core complexes subparallel to the SMO (Davis and Coney, 1979). The regional tectonic framework of northwestern Mexico provides a context of the relative stress regimes responsible for extension (Figure 10). Goodell (In Prep.) has interpreted pull-apart basin geometries along the western margin of the SMO (e.g. Temoris-Guazapares Basin, El Sauzal - Cuenca de Oro) where the northern and southern boundaries are coincident with the trends of the transform faults in the Gulf of California, suggesting that early stages of extensional deformation was a contributing factor for the emplacement of mineralization. The structural trend in southwest Chihuahua has a dominant NW-SE orientation which has been favorable for the epithermal type mineralization (Figure 11).

2.5 REGIONAL METALLOGENY

The SMO rich metallogenic province is host to the formation of a variety of ore deposits. Staude and Barton (2001) synthesize Mexico's northwestern metallic mineralization where they recognized >2500 metal occurrences. The Jurassic to Early Cretaceous deposit types were mainly intrusion-related Cu, skarns, volcanogenic Fe, and shear-zone Au-bearing quartz veins. During the mid-Cretaceous, Cu (\pm Au) porphyries, W skarns, and mesothermal Au-bearing quartz veins were deposited. The Laramide was a period of abundant mineral deposits. Numerous porphyry Cu (\pm Mo), W and Pb-Zn skarns, and Au-Ag quartz veins are distributed in the eastern margin of the LVS (Damon et al., 1983; Staude and Barton, 2001; Clark and Fitch, 2009). The Late Eocene to Oligocene was another major period of metallic mineralization hosting various deposit types of significant economic importance, principally low-sulfidation Ag-Au (\pm Pb-Zn-Cu) epithermal veins, high-sulfidation Au-(Cu), and high-temperature carbonate-hosted deposits (Staude and Barton, 2001; Clark and Fitch, 2009). Mineral distribution follows the NW-SE trend as the magmatic arc of the Laramide (Figure 12). The regional metallogeny and geologic setting provides a context for the local geology in the Palmarejo district which consists of multiple Ag-Au quartz vein occurrences in several structural belts trending NW to SE hosted by Cretaceous to Paleocene andesites of the LVS.

2.6 PALMAREJO DISTRICT GEOLOGY

The largest known deposits in the Palmarejo district are the Palmarejo, Guadalupe and La Patria occurrences. The genetic classification of Palmarejo is consistent with the characteristics of the intermediate-sulfidation type described by Hedenquist et al. (2000). The epithermal deposits in the district are hosted in the LVS along fissure zones and appear to be related to the

silicic plug-type intrusions (Rasmussen et al., 2014). The association between silicic intrusions and mineralization in the SMO is discussed by Bryan et al. (2008). Figure 13 shows the geologic mapping by the *Servicio Geológico Mexicano* (SGM) placing andesitic rock with lesser amounts of rhyodacite volcanic tuffs and related intrusions of the LVS in the western margin of the district. Other exposed units of the LVS consist of rhyolitic flows, volcanoclastics, and related shallow intrusions overlain by andesitic flows with related andesitic porphyry intrusions.

The stratigraphic column in the Palmarejo district (Figure 14) is based on field mapping conducted by Coeur Mining Inc. The unit names, descriptions, and classification format has remained identical to the company's reports. At the base it consists of a Cretaceous limestone - sandstone sequence (KaCz-Ar) overlain by an andesitic conglomerate (KtalCg). Above these units are Cretaceous laminated andesitic siltstones and fine-grained sandstones (Ktal) interbedded by andesitic epiclastic tuffaceous rhyolites (KtalRHY) and amygdaloidal andesites (Ktam). Overlaying these units are Cretaceous andesitic sandstones and gritstones with polymict conglomerates (Ktat). These Cretaceous volcano-sedimentary units correspond to the LVS and are overlain by Tertiary rhyolites and rhyolitic tuffs (ToTR), rhyodacites (ToRD), and basalts (TmB) of the UVS covered by Quaternary alluvium (Qho). The intrusive units found in the district are Cretaceous granodioritic plutons (KsGd), Cretaceous andesitic porphyries (Ktap), and a Tertiary rhyolitic porphyries (ToPR) (Figure 14). The dacitic and rhyolitic intrusions appear to be closely associated with mineralization (Kerr et al., 2015).

In this region, mineralization is controlled by NW to SE trending structures, dipping about 45° to 70° either southwest or northeast, which served as the migration paths for metalliferous fluids leading to the formation of ore deposits (Figure 13). The intersection of structures have demonstrated to be important zones and an increase in mineralization takes place

at inflection points (Sillitoe, 2010; Birak and Blair, 2012). Regional extensional structures trending NW to SE resulted in the formation of horsts and grabens throughout the SMO. Murray and Busby (2015) discuss silicic intrusions and intrusion-related epithermal deposits being hosted by normal faults in the region. Although, certain host rock characteristics, such as brittleness, has proven to be favorable for vein formation as it is the case in silicified laminated sandstones (Kerr et al., 2015).

2.6.1 Independencia – Los Bancos Geology

At the Independencia deposit, lithic volcanic andesites overlie amygdular basalts with a sequence of laminar andesites present as the host-rock, with younger porphyritic rhyolites cross-cutting porphyritic andesites (Figure 14). Alteration includes propylitization, argillization, and silicification. The mineralization is controlled by a NW trending structural zone that generally dips 60° to 70° to the northeast (Kerr, 2015). The surface expression of the Independencia structure may be indicated by brecciation and argillic alteration zones (Figure 15). The mineralization is comprised of quartz veins, quartz-vein breccias, hydrothermal breccias, and hematitic tectonic breccias. The dominant sulfide minerals in unoxidized portions of the vein include silver sulfosalts, pyrite, sphalerite, and galena (Wilson et al., 2013). High concentrations of gold, as electrum, are very common in highly oxidized portions of the vein, it is disseminated and often associated with goethite and hematitic limonites. A gold characterization report by Pérez Segura (2013) suggests that goethite comes from the oxidation of pyrite indicated by millimeter-size boxworks with gold included in the pyrite. However, careful examination of drill-core at a macroscopic level did not revealed evidence of pyrite suggesting a different scenario where the hematitic limonite may have evolved from primary high temperature and

gold-bearing solutions. A detailed petrographic analysis as well as a fluid inclusion study may provide insights about the conditions in which precipitated gold.

The Los Bancos deposit is located 500 m west of Independencia and both deposits share similar geology. The Los Bancos vein also has a NW structural trend dipping approximately 70° to 80° to the west. Field evidence suggests the structure has a continuation to the south where it may have an extension with the Dana structure, drilled by Paramount Gold & Silver Corp. in 2014 (Coeur, 2015).

3. Methodology

3.1 SAMPLE COLLECTION AND DATA ACQUISITION

Coeur Mining Inc. and Paramount Gold & Silver Corp. granted permission for us to collect samples from their properties in the summer of 2014. With the collaboration of Liza Ortega and Manuel Moncada, UTEP Geology students, 11 surface rock samples were collected from rhyolitic, andesitic, and basaltic outcrop exposures throughout the Palmarejo district and in selected locations outside the district (Figure 17). Additionally, samples from five drill cores in the Guazapares district were provided by Paramount Gold & Silver Corp. The samples are geochemically analyzed and five of the samples are selected to conduct a zircon U-Pb geochronology and $\epsilon\text{Hf}(t)$ isotopic studies by the laser ablation inductively coupled plasma mass spectrometry (LA-ICP-MS) (Table 1).

An additional geochemical data set was provided by Coeur Mining Inc. from the Independencia and the Los Bancos deposits. These data sets includes survey and collar data, lithology, and geochemical assay values for 1094 samples collected at selected intervals from 103 drill cores from the Independencia vein and for 565 samples collected at selected intervals from 65 drill cores from the Los Bancos vein (Figure 18). Samples from the Independencia system were analyzed for 36 chemical elements. The geochemical assay data from the Independencia system is used to conduct a multivariate data analysis. The entire drill core data set (survey, collar, lithology and assay) is used to construct a 3D geological model.

3.2 IGNEOUS PETROLOGY AND GEOCHEMISTRY

A geochemical analysis for major and trace elements is conducted on 10 volcanic outcrop samples collected in the Palmarejo district and on five drill core samples from the Guazapares

area (Figure 19). Major and trace elements were analyzed by the Fusion ICP/MS methodology at Activation Laboratories Ltd (Table 2). The geochemical signatures from the 15 volcanic rock samples collected may provide clues about the regional geologic processes involved in the evolution of southwest Chihuahua. The main control over the chemistry of a rock is the chemical composition and mineralogy of the source region, as well as the type of melting process and the degree of partial melting (Rollinson, 1993). Weathering and hydrothermal fluids may affect all aspects of the rock chemistry, therefore, studies in isotopic compositions may help to further investigate rocks that have undergone alteration (Rollinson, 1993). The rocks analyzed in this research show some degree of alteration due to regional hydrothermal activity. Major element – Al, Ca, Fe, K, Mg, Mn, Na, P, Ti, and Si – chemistry data, listed as oxides in weight percent, is used for the construction of variation and rock classification diagrams. In addition, trace elements, listed in parts per million, are used for the construction of discrimination diagrams.

3.3 GEOCHRONOLOGY AND ISOTOPIC SIGNATURES

The time constraint and origin of extrusive rocks is analyzed by performing zircon U-Pb geochronology and ϵHf (t) isotopic studies by LA-ICP-MS on five rhyolitic ignimbrites collected in the Palmarejo district (Figure 19). One of the major advantages of zircon is its ability to survive magmatic, metamorphic and erosional processes that destroy most other common minerals (Corfu et al., 2003). It is because of this property that zircon is one of the most widely used minerals to extract information on the genesis of volcanic rocks.

3.3.1 Sample Preparation and Processing

The sample preparation and processing was conducted at the Department of Geological Sciences at The University of Texas at El Paso (UTEP) under the guidance of Dr. Munazzam Ali

Mahar, whose area of expertise focuses on provenance studies and post collisional magmatism based on geochronology and isotopic signatures in zircons (e.g., Mahar et al., 2014; Mahar et al., 2016). The zircon extraction from rock samples was done by standard mineral separation techniques. Rock samples were cut into approximately 2 inches (in) blocks with a rock saw. Cut samples were washed to remove any dust and contaminants and dried using a hot plate. A representative sub-sample was taken at this stage for the geochemical analysis. The samples were further reduced into rock chips and powder in a jaw crusher then sieved with a 500 microns (μm) mesh. To reduce cross-contamination, the equipment was cleaned thoroughly after every use and between each sample with the use of a wire brush, vacuum cleaner, compressed air and then wiped over with acetone to remove any remaining residue.

After preparing the samples, approximately 200-300 grams (g) of sample was considered for the mineral separation procedures. First, the samples are placed on a clean surface to run a hand magnet through the sample to remove any metal filings introduced from the crusher. The first separation procedure was a gravity separation with water and gold panning techniques. This process eliminates light minerals such as clays, quartz, and feldspars leaving behind the denser minerals. Zircon, the target mineral can be found in this dense fraction along with pyroxenes, micas, amphiboles, magnetite, pyrite, and apatite. The samples were dried using a heat lamp. The second procedure involved separating minerals according to their magnetic properties by using the Frantz Magnetic Separator which induces magnetic fields at various electrical current and inclination settings. This procedure discriminates minerals with a high magnetic susceptibility such as magnetite, amphiboles, pyroxenes, and biotite which were collected in a container. Zircon, a non-magnetic mineral was collected in a separate container along with muscovite, apatite, and any remaining quartz and feldspars. The last gravity separation was done with

lithium heterotungstate (LST) heavy liquid to separate minerals lighter than 2.86 specific gravity such as quartz, feldspar and in some cases muscovite. Zircon has a specific gravity of 4.6-4.7 and therefore it sinks in the heavy liquid allowing for the recovery. Unfortunately, other minerals with high specific gravities such as pyrite and apatite, which can be mistaken for zircon, sink as well. The separated samples of zircon concentrate were rinsed thoroughly several times to remove LST residue. The final step was to analyze the mineral grains with the aid of a stereo microscope to hand-pick zircons for the analytical procedure (Illustration 1).

3.3.2 Analytical Methods

The zircon U-Pb and ϵHf (t) measurements were conducted by the LA-ICP-MS method at the LaserChron laboratory (<http://laserchron.org>) of the University of Arizona (Illustration 2). The analytical methods used for the U-Pb measurements are described by Gehrels et al. (2008), whereas the Hf isotopic measurements are described by Cecil et al. (2011).

3.4 STATISTICAL DATA ANALYSIS

Exploratory Data Analysis (EDA) techniques aid in the visualization of statistical data with the use of graphical outputs, as explained by Reimann et al. (2008). The statistical distribution of data may provide insights about geochemical processes or trends involved in the ore body formation. In this study, a statistical data analysis was conducted on the geochemical assay data set from the Independencia vein system.

3.4.1 Statistical Data Treatment

Statistical treatments were conducted on drill core samples from the Independencia vein. The statistical analysis was done using R with code provided by Dr. Mark Engle, Research

Geologist with the United States Geological Survey (USGS). Variables were >50% of the observations recorded with concentrations less than the detection limits were discarded for analysis. Non-detect observations were treated by applying multiplicative lognormal replacements for data imputation (Palarea-Albaladejo et al., 2014). A logit transformation was applied to data, as required for proper treatment of compositional data. The Independencia geochemical assay data was also treated based on lithology. A bivariate treatment was conducted on concentrations from the mineralized structure, andesites, and rhyolites. In order to open the data, thus properly treating the compositional nature of the dataset, a centered-log-ratio (clr) transformation was applied for the multivariate treatments.

3.4.2 Data Analysis Methods

The variables of interest were analyzed in order to observe the relationship of Ag with other elements and the geochemical processes involved in an intermediate-sulfidation epithermal system. A combination of histogram, one-dimensional scatter plot, and box-plot are used to analyze the distribution of each element from the Independencia system. A variation matrices and clr biplots are constructed for all elements which were considered. A univariate summary statistics table for logit-transformed data was constructed in order to observed similar values for the compositional analysis. A variation matrix on log-transformed data is constructed in order to analyze the proportionality or the lack of proportional relationships between variables. A principal component analysis (PCA) is used to reduce the number of dimensions of clr-transformed data in order to interpret trends and variations in the data set (Levitan et al., 2014). The results of the PCA are represented with a robust biplot of compositional data. A hierarchical cluster analysis is conducted on log-transformed data to evaluate relationships between groups of

clusters of the most similar elements (Levitan et al., 2014). The results from the hierarchical cluster analyses are represented with dendrograms.

3.5 GEOLOGICAL MODELLING

A 3D geological model of the Independencia – Los Bancos Ag-Au epithermal vein systems is constructed in order to evaluate the deposits, metal distribution and resources. The model is constructed using Leapfrog Geo, a 3D implicit modelling software developed by ARANZ Geo Ltd (<http://www.leapfrog3d.com>). Leapfrog has become an important tool for exploration geologists as it has dramatically reduced the time spent modelling by the traditional explicit method. An implicit geological model is generated by computer algorithms directly from a combination of imported drill-hole data and the user's geological interpretations (Cowan et al., 2003). The incredibly fast speeds in which an implicit geological model is constructed, allows geologists to spend more time working on interpretations and evaluations of the deposit, as well as having multiple or alternative models and quickly updating with the latest available data.

The Independencia – Los Bancos drill-core data set was provided by Coeur Mining Inc. for the construction of the 3D geological model. This data set includes survey and collar data, lithology, and geochemical assay values for 1094 samples collected at selected intervals from 103 drill cores from the Independencia vein and for 565 samples collected at selected intervals from 65 drill cores from the Los Bancos vein. The Palmarejo district stratigraphic column (Figure 14) was used to define the geochronological order of lithological units that were modelled.

3.5.1 Geologic Model

The first step in the process of constructing a 3D model is to clean and edit the working database of the project. This database consists of excel files for: 1) collar data, which includes drill-hole ID with X, Y and Z coordinates, as well as drill-hole depth, 2) survey data, which includes azimuth and dip information measured at approximately 50 m intervals down the drill-hole, 3) lithologic data, with information on rock types correlated with stratigraphic units measured at selected intervals, and 4) assay data, which includes geochemical values for 36 elements, sampled at approximately 1.5 m intervals in mineralized zones. Additional data includes shapefiles of the surface lithology contacts and a digital elevation model (DEM) of the study area. Leapfrog Geo is capable of rapidly producing 3D contours based on drill-hole data without the need of spending numerous days creating and manipulating polylines to construct models from cross-sections as it is the case with other modelling softwares.

The shapefiles of the surface lithology contacts are used to construct the geologic map in ArcGIS to later import the map into Leapfrog Geo. The DEM is converted into a point file which holds high resolution X, Y, and Z data that can be extracted into an excel file to import into Leapfrog Geo as elevation points for the topography construction. From the imported elevation points a new topography is created and the geologic map is draped onto the new topography. A polyline is created by digitizing the trace of the Independencia structure. This polyline is then used to construct a mesh that is used to create the structural trend of the geologic model. The geologic model is digitized in Leapfrog Geo by creating GIS lines of the different lithologies. At this point the drill-hole data (collar, survey, lithology, and assay) is imported. The lithologic units that are modelled consist of the mineralized structure (EM), the stockwork (STWK), rhyolitic porphyries (ToPR), andesitic porphyries (Ktap), amygdaloidal andesites (Ktam),

andesitic sandstones and gritstones with polymict conglomerates (Ktat), and a sequence of andesitic conglomerate (KtalCg) overlain by laminated andesitic siltstones and fine-grained sandstones (Ktal) interbedded by andesitic epiclastic tuffaceous rhyolites (KtalRHY), these three units were combined and modelled as Ktal. Differentiating the Los Bancos vein from the Independencia veins is done by adding the drill-hole data and only making visible the EM intercepts to do an interval selection to create a Los Bancos vein unit and an Independencia vein unit. This process is repeated for the stockwork intercepts.

A geologic model is created with the drill-hole data as the boundary extent. The first units to model are the vein structures by creating a new vein under surface chronology. The midpoints of the veins are extracted to create 100 m buffer of these points to reshape the vein model based on the buffer enclosing areas where there is lithological data. A few adjustments are made on the hanging wall and foot wall points of the vein to make it continuous. The same process is repeated to create the stockwork model which is an envelope of the veins. Units ToPR, Ktap, Ktat, and Ktam are modeled as new intrusions. Output volumes are created based on a spheroidal interpolant which respects the structural tendency given by the defined structural trend. The Ktal is model as background lithology, therefore it behaves as the host rock and it will fill-in the areas where no lithology data is present. Units are placed in chronological order according to the stratigraphic column under the surface chronology and the output volumes are activated here to create the geologic model.

3.5.2 Interpolation Models

An interpolation model for Ag (ppm), Ag equivalent, Au (ppm) and Au equivalent is created under the interpolants field. A first pass Ag interpolant is created to see how the isosurfaces behave. This first pass is an unrealistic model as parameters (e.g. compositing, sill,

base range, nugget effect, and drift) have not been modified at this point. To refine the interpolation model, the compositing length is set to 4 m because the down-hole sample interval space is on average every 1.4 m. The minimum coverage is set to 100 % meaning that length at the end of the drill-hole must be 100 % of the composite length in order to be considered. In this case, anything less than 4 m at the end of a drill-hole is discarded. The following changes are made to the interpolation parameters. The base range should be set to 2 to 2.5 times the distance between drill-holes. The distance between the Independencia – Los Bancos drill-holes is approximately 100 m, therefore the base range is set to 200 m. The sill is set to 3,590, which is the total variance of the data. The nugget is set to 0.219, which is a value determined by Coeur Mining Inc. (Kerr et al., 2015). The drift is set to none and the alpha is set to 9, as it gives the best approximation to the spheroidal variogram. The resolution is set to 4 m which is the composite length. Volumes enclosed is set to intervals. Modifying these parameters creates a refined interpolation model. The last step is to clip the interpolation to the mineralized structures. This process is repeated for the Au interpolation. Silver and Au equivalent calculations are done in excel to later import into Leapfrog Geo as a new table before creating the interpolation models.

4. Data

4.1 IGNEOUS PETROLOGY AND GEOCHEMISTRY

The following petrological representations were obtained from the geochemical data set in Table 2 for the 15 volcanic rock samples collected from the Palmarejo district. In general, variation diagrams show a decreasing slope as silica increases, with the exception of the SiO_2 vs. K_2O and the SiO_2 vs. Na_2O plots where no apparent trend is observable. The data are discontinuous: samples CH1 from Chinipas, SA from San Antonio and SJ from San Jose show relatively low SiO_2 values and high Fe_2O_3 (T), MgO and CaO values. These three samples are distinguished from the rest of the samples which show values ranging from approximately 67 to 80 wt. % SiO_2 and with variable major element values. Sample SC is quartz-vein material as it contains above 95 wt. % SiO_2 , therefore it is not considered for interpretations (Figure 20 – A-I).

4.1.1 Rock Classifications Using Major Element Data

The chemical classification of these volcanic rocks is based on the total alkali-silica diagram for volcanic igneous rocks by LeBas et al. (1986). The total alkali content of these samples ranges from 5.31 to 12.08 $\text{Na}_2\text{O} + \text{K}_2\text{O}$ wt. % and the silica content ranges from 56.1 to 79.76 SiO_2 wt. %. Based on this classification, sample CH1 is a basaltic andesite, samples SA and SJ are trachyandesites, sample SF2 is a trachydacite, and samples GAT1, GAT2, GAT3, MC1, MC2, MC3, SF1, SF2, SL1, and SL2 are rhyolites (Figure 21).

To differentiate these samples between an alkaline magma series and a sub-alkaline magma series the classification diagram by Irvine and Barragar (1971) was used. Samples are discriminated against their silica and total alkali content. Sample SF3 plots above the curve in the alkaline series region while the rest of the samples plot below the curve in the sub-alkaline series

range. Sample SJ plots along the curve (Figure 22). The feldspathic igneous rock classification diagram by Frost and Frost (2008) was used to further discriminate samples between four gradations of calcic to alkaline rocks. Discriminations are made based on the silica and the total alkali content subtracted by CaO wt. %. Under this classification, the two trachyandesites, samples SA and SJ, plot in the alkalic region whereas the trachydacite, sample SF2, plots along the boundary between the alkalic-calcic and the alkalic classifications. The basaltic andesite, sample CH1 with the lowest silica content, plots in the calc-alkalic region. The rhyolitic samples with higher silica content plot in the alkali-calcic and calc-alkalic region with the exception of sample SL2 which plots in the calcic boundary (Figure 23).

4.1.2 Rock Discriminations Using Trace Element Data

Trace elements provide further information about petrological processes and are more capable of discriminating between igneous processes and tectonic environments than major elements (Rollinson, 1993). For the following discriminations, the trace elements Th, Co, Rb, Nb and Y (ppm) were used as these elements are relatively immobile in aqueous solutions, therefore are stable under hydrothermal conditions (Rollinson, 1993).

A classification diagram of altered volcanic island arc rocks by Hastie et al. (2006) was used to discriminate samples on a basis of rock type and magma series by using the immobile trace elements Th and Co. Based on this discrimination plot, samples MC1, SL1 and SL2 plot above calc-alkaline curve in the high-K and shoshonitic region and are classified as dacitic-rhyolitic-latitic-trachytic rocks. Sample SJ plots within the calc-alkaline region and is classified as a basaltic rock. Samples CH1 and SA plot in the calc-alkaline region and are classified as basaltic andesite-andesitic rocks. The rest of the samples plot within the calc-alkaline region and are classified as dacitic-rhyolitic-latitic-trachytic rocks (Figure 24). This diagram validates the

results obtained from the rock and magma series classifications based on the major element data. Sample SJ was the only sample with inconsistent results between the classifications.

The tectonic discrimination diagram by Pearce et al. (1984) was used to interpret the tectonic setting associated to these volcanic rock samples based on the Rb-Y-Nb variations. Samples SF3, SL2, MC1 and MC3 are interpreted to be associated to a syn-collisional setting, however they plot near the volcanic arc setting boundary. Sample SA also plots near the volcanic arc setting boundary and it is associated to a within-plate tectonic setting. The rest of the samples are interpreted to be associated to a volcanic arc setting (Figure 25).

4.2 GEOCHRONOLOGY AND ISOTOPIC SIGNATURES

The U–Pb and Lu–Hf isotopic analyses were done by multicollector laser ablation inductively coupled plasma mass spectrometry (LA–ICP–MS) at the LaserChron Center at the University of Arizona (Table 5). Before analysis, zircons were imaged by Cathodoluminescence (CL) at the LaserChron SEM lab facility. Cathodoluminescence imaging is critical to identify internal domains within the grains, grain cracks, mineral inclusions and two-dimensional growth and recrystallization textures to guide spot placement onto least disturbed growth domains.

4.2.1 Zircon U-Pb Ages of Ignimbrites

A total of five samples were dated from ignimbritic rhyolites exposed in the Guerra Al Tirano (GAT1, GAT2 and GAT3), Guadalupe Norte (GPN2) and San Francisco (SF1) areas. The zircons are exclusively magmatic with strong oscillatory zoning from core to rim; sector zoning is also observed. Zircon morphology observed under the CL and U–Pb dating revealed no inherited or xenocrystic cores. Generally, all the samples yielded concordant ages. Samples GAT1, GAT2 and GAT3, the southern-most ignimbrites, yielded a weighted mean age of $23.1 \pm$

0.4 Ma (MSWD = 0.41, n = 13), 23.4 ± 0.4 Ma (MSWD = 0.36, n = 19), 23.7 ± 0.4 Ma (MSWD = 0.39, n = 13), respectively (Figure 26 – A-C). The majority of the individual dates varies from 21 Ma to 23 Ma. One grain yielded the oldest age of 32.1 ± 5.6 Ma. The overall variation in the 45 individual analyses range from 21 to 32 Ma with majority (89 %) of the total analyses yielding ages between 21 to 23 Ma. Only 5 individual analyses out of 45, yielded older ages varying from 24 to 32 Ma. Sample GPN2, collected ~ 4 km north of the Guerra Al Tirano area, yielded a weighted mean age of 23.7 ± 1.1 Ma (MSWD = 0.71, n = 4) (Figure 26 - E). Sample SF1, from the San Francisco area approximately ~ 9 km northeast of Guadalupe Norte, yielded a weighted mean age of 28.1 ± 1.0 Ma (MSWD = 1.2, n = 13) (Figure 26 - D). The majority of the individual dates varies from 24 to 30 Ma. One grain yielded the oldest age of 32.6 ± 4.0 Ma.

4.2.2 Zircon ϵHf (t) compositions

The weighted mean zircon initial Hf isotope composition (ϵHf (t)) is calculated at the individual U-Pb crystallization dates of each zircon spot. It should be noted that Hf isotope compositions are at 1σ level. All the 49 analyses on selected zircons yielded ϵHf (t) composition varying from -0.6 to +7.8 with a majority (85%) of the samples ranging from +1.0 to +5.8. Four analyses yielded extreme positive values ranging from 6.0 to 7.8 (Figure 27 – F). Only three analyses yielded negative values close to unity, ranging from -0.6 to -0.5. Three samples from the southern-most ignimbrites, located at Guerra Al Tirano (GAT1, GAT2 and GAT3), yielded radiogenic and positive weighted mean ϵHf (t) of 4.6 ± 1.0 (MSWD = 1.8, n = 10), 3.3 ± 0.8 (MSWD = 2.0, n = 13), and 4.7 ± 0.9 (MSWD = 1.4, n = 10), respectively (Figure 27 – A-C). Four analyses (rim to core) on two grains from the Guadalupe Norte ignimbrite (GPN2) yielded the evolved weighted mean ϵHf (t) of 0.6 ± 2.2 (MSWD = 2.2, n = 4) (Figure 27 – E). Sample

SF1, from the San Francisco area, yielded a weighted mean $\epsilon_{\text{Hf}}(t)$ of 1.6 ± 0.9 (MSWD = 1.7, $n = 12$) (Figure 27 – D).

4.3 STATISTICAL DATA ANALYSIS

A statistical treatment was applied to the geochemical assay data from the Independencia vein. The variables Ag, As, Au, Ba, Cu, Fe, Mn, Pb, Sb, and Zn are analyzed to observe the statistical distribution of these elements which may help define trends or geochemical processes involved in the ore body formation. The measure for central value is represented with the mean and median. The measure for spread is represented with the standard deviation (SD) and the interquartile range (IQR). These values, along with other statistical parameters, are summarized in Table 3.

4.3.1 Univariate Analysis

The statistical data is expressed with similar values by applying a logit transformation to all variables. Results from the univariate analyses are presented as density histograms, one-dimension scatter plots and box-plots (Figure 29 – A-J). Overall, the elements show a normal distribution characterized by the bell-shape curve. The influence of values below the detection limit is observed in the Au histogram which displays two peaks in its distribution (Figure 29 – C). The distribution of Sb continues to be heavily right skewed as it is controlled by a low value population (Figure 29 – H). The box-plots for As, Cu, Fe, Mn, Pb, Sb, and Zn are indicating which values are considered outliers (Figure 29 – B and E-J).

4.3.2 Bivariate Scatterplot Matrix

The scatterplot matrix displays correlations between the variables which are grouped based on lithology. The groups consist of mineralized bodies such as the quartz vein, stockwork, and hydrothermal breccias represented in red color, rhyolitic rocks in green, andesitic rocks in blue and an andesitic porphyry in purple (Figure 30). Observations from this scatterplot matrix shows that within the mineralized bodies, Ag has a positive correlation with As, Au, Cu, Mn, Pb Sb, and Zn. The highest correlations are between Ag and Au, Pb and Zn with correlation coefficients of 0.922, 0.686 and 0.697, respectively. These high correlations of Ag are consistent and across andesitic porphyry. The most significant observation in Au is its weak correlation with Fe. High correlations between Au and Pb and Zn, with correlation coefficients of 0.723 and 0.695, respectively, are observed. Correlations between other variables are in general positive, although the correlation coefficients are not as high. Most notable is the high correlation coefficient of 0.863 between Pb and Zn. The density plots of Ag and Au against their own variables indicate distinct populations of Ag and Au within the mineralized bodies, andesitic and rhyolitic rocks where the distribution of the mineralized body is left skewed and different than the distribution in andesites and rhyolites.

4.3.3 Multivariate Treatment

In order to observe proportional relationships between element log-ratios, variation matrices on clr-transformed data are constructed for the ten variables from the Independencia geochemical assay data set. Four variation matrices are constructed based on grouped lithologies consisting of mineralized bodies, rhyolitic rocks, andesitic rocks and andesitic porphyries. The log-ratios between the variables are calculated in each variation matrix using the robust median

absolute deviation (MAD) of the log-ratios (upper triangle), as well as the variables log-ratio mean (lower triangle) (Table 4 – A-D). High values show high variance between the ratios of two elements, indicating disproportional relationships. Low values indicate low variability suggesting the two elements are proportional (Levitan et al., 2014). Results from the variation matrix for the mineralized Independencia structure indicate proportional relationships by the relative low log-ratio variances, of values below one, between Ag/Au, As/Fe, Fe/Mn, Cu/Pb, Cu/Zn, Fe/Sb, Mn/Zn, Pb/Zn and Sb/Zn. The highest proportionalities are between Ag/Au and Pb/Zn with variation coefficients of 0.68 and 0.44, respectively. The highest log-ratio variances are between Ag/As, Ag/Fe, Au/As with coefficients above 7 and Au/Fe with a coefficient of 9.03 (Table 4 – A). Gold has a higher correlation with Fe with the rhyolitic rock, andesitic rocks and the andesitic porphyry, with low variation coefficients of 0.31, 0.77, and 0.31, respectively (Table 4 – B-D). Moreover, the highest dispersion in the mineralized structure data is seen in Ag and Au which show high clr-MAD coefficients of 1.87 and 1.98, respectively.

The primary goal of a PCA is to reduce dimensionality, as describe by Reimann et al. (2008). Four compositional biplots of clr-transformed data are constructed for the PCA (Figure 31 – A-D). The principal components (PC) plotted for the ten variables from the Independencia data are represented as loading vectors (arrows). Since the PCA is done with clr-transformed data, links between vectors can be used to interpret processes as explain in Levitan et al. (2008). Short links suggest a low log-ratio variance between two elements, whereas, long links suggest disproportional relationships. Links can also be compared to one another. Parallel links or links with low angles between them indicate correlation between the pairs of elements. Perpendicular links suggest independence between the pairs of elements, which may be verified with the variation matrix (Levitan et al., 2014). For instance, the low variability between Ag and Au and

between Pb and Zn (as noted in Table 4) is suggested as the links between the element pairs are short. Within the mineralized structure, high variability is indicated by the long Ag-Fe, Ag-As, Au-Fe and Au-As links (Figure 31 – A). These observations are consistent with results from the variation matrix (Table 4 – A). Barium seems disassociated within the data as its loading vector points towards the negative PC 2.

A cluster analysis was conducted to evaluate similarities between the ten variables from the Independencia vein. Results from the cluster analysis are presented with hierarchical dendrograms (Figure 32 – A-D). The y-axis, labeled as height, is a measure of closeness of individual variables or clusters. The cluster analysis, within the mineralized structure (Figure 32 – A), divided the elements into three groups. Group 1 consists of Ag, Au, Pb and Zn, elements associated to epithermal-type mineralization. Group 2 consists of As, Sb, pathfinder elements in geochemical exploration and Mn and Cu. Group 3 consists of Fe, element from common oxide minerals in this environment and Ba. In this figure, Ba and Fe continue to appear disassociated with the rest of the variables as it has greatest height. The low heights of Ag-Au and Pb-Zn indicate the proportionality of these element pairs (Figure 32 – A).

4.4 GEOLOGICAL MODEL

The main objective in constructing the geologic model of the Independencia – Los Bancos deposit is to determine the geometry and placement of lithologic units and intrusive bodies with respect to the mineralized structures hosting the economic concentrations of precious metals. To accomplish this, geologic and geochemical components from drill-hole data are combined to generate volumes based on the distribution of categorized intervals. Leapfrog Geo is used to create the geological model for its implicit 3D counteracting capability. 3D counteracting of

assay data may help highlight structural controls of fluid flows or zonation patterns of mineralized domains.

The Independencia – Los Bancos deposit comprises laminated andesitic flows, volcano-sediments with polymict conglomerates, and intercalated amygdular basalts to andesites (Ktal, Ktam, Ktat and Ktap) which are intruded by an andesitic porphyry (Ktap2) and a younger rhyolitic porphyry body (ToPR). The Ktal, Ktam and Ktat units are subdivided into a second category of each to illustrate thin depositional layers within different lithologies, these thin layers are grouped into Ktal2, Ktam2 and Ktat2. The relationship observed in the geologic model has the laminated andesitic flows (Ktal) deposited at the base, followed by thick sequence of amygdular basalts, which are intercalated by thin layers (Ktal2 and Ktam2). The top units comprise andesitic sandstones with polymict conglomerates divided into two volcano-sedimentary units (Ktat and Ktap). A thin layer of a lithic andesite (Ktat2) is intercalated within the Ktat. In a later phase, the andesitic porphyry (Ktap2) cross-cuts these volcano-sediments. The younger rhyolitic porphyry (ToPR) is cross-cutting all the units (Figure 14). The mineralization is inferred to be younger than this last intrusive body, therefore the Independencia and Los Bancos veins were place on top in the geochronological order of events. The Independencia vein is then wrapped by the stockwork. The Independencia and Los Bancos veins have a general NW orientation of $\sim 325^{\circ}$ which is congruent with the general trend observed in the Palmarejo district (Figure 33).

4.4.1 Metal Distribution

The distribution of Ag and Au along the veins is observed by constructing interpolation models of metal assay data. To generate volumes for Ag the following iso-values (ranges) are used: <10.0, 10-35, 35-150, and >150; for Au <0.15, 0.15-1.0, 1.0-1.5, 1.5-3.0, and >3.0,

expressed in ppm. At Independencia, the highest concentration of Ag and Au is observed in the southern sector of the vein where a high grade intercept from drill-hole VIDH-048 cut 8.47 m at 627 g/ton Ag and 12.4 g/ton Au. Values tend to decrease towards the northern sector of the vein (Figure 34). The mineralization at Los Bancos is less continuous, however higher concentrations of Ag and Au are present in the northern sector of the vein (Figure 35).

5. Discussion

5.1 PREVIOUS UNDERSTANDING OF THE IGNIMBRITE FLARE-UP AND RELATED TECTONISM

Recent U-Pb geochronological data suggest that the Late Oligocene (32 to 28 Ma) and Early Miocene (24 to 20 Ma) volcanic activity, which produced the large-scale ignimbrite flare-up, is largely syn-genetic with the post-Laramidic Tertiary extension (e.g. Ferrari et al., 2002; Murray et al., 2013; Murray and Busby, 2015). The extensional stress regimes in the region have created pull-apart basin geometries, bounded by large-scale lineaments (e.g., Goodell, 1995; Galvan-Gutierrez, 2005; Feinstein, 2007), where world-class ore deposits were emplaced (e.g. Palmarejo and El Sauzal). This ignimbrite flare-up overlaps in space and time with the Basin and Range extensional deformation, which occurred between 32 Ma and 12 Ma (Aguirre-Diaz and McDowell, 1993; Aranda-Gomez et al., 2000). The early stages of extension in the Gulf of California, recorded at approximately 29 Ma, marks the initiation of the opening of the Gulf of California (Ferrari et al., 2013). The general consensus states that the opening of the Gulf began from 14 to 12.5 to Ma at the final stage subduction of the Farallon Plate (Stock and Hodges, 1989). However, new insights from the plutonic record in the Gulf of California suggest that rifting was initiated in the Early Miocene (25 Ma to 18 Ma) (Ferrari et al., 2013; Duque-Trujillo, 2014). Differentiation between Gulf extensional structures and Basin and Range extension is difficult in parts of northwestern Mexico, as they spatially coincide. The time constraint for extension in the northern SMO in relation to the ignimbrite flare-up is limited. Studies by Dreier (1984) in western North America and Mexico have inferred that extension may have begun as early as the Eocene, based on the orientation and age of epithermal deposits (Murray et al., 2013). Other authors suggest that the start of the Early Oligocene flare-up records the initial

extension (e.g., Aguirre-Diaz and McDowell, 1993). Different mechanisms or a combination of forces are attributed to the ignimbrite flare-up and extension of the Basin and Range province of North America (Ferrari et al., 2013). There are boundary forces, such as trench retreat, rollback and steepening of the subducting Farallon plate (e.g., Best and Christiansen, 1991; Ward, 1991; Bohannon and Parsons, 1995; Dickinson, 2002; McQuarrie and Oskin, 2010), which provide the conditions to produce the gravitational collapse of a thickened crust, extensional deformation, mantle upwelling and large-scale silicic volcanism (e.g. Gans et al., 1989; Harry et al., 1993; Leeman and Harry, 1993; Axen et al., 1993; Humphreys, 1995; Wilson et al., 2005; Wong et al., 2010). These processes or combination of forces were probably active in northwest Mexico, which led to the ignimbrite flare-up of the UVS.

5.2 TIMING OF THE IGNIMBRITE FLARE-UP IN THE PALMAREJO DISTRICT

The ignimbrite flare-up of the UVS has been recognized to have occurred in two main pulses throughout the SMO. The episodic nature of silicic volcanism is recorded in the Early Oligocene (32 to 28 Ma) and Early Miocene (24 to 23 Ma) ages (Ferrari et al., 2002, and the references therein). Available U-Pb age data (e.g., Murray et al., 2013) from the Guazapares mining district record the Early Oligocene pulse (27.5 Ma) of silicic ignimbrites of the Parajes formation and the Early Miocene pulse (24.5 Ma) of mafic to intermediate volcanic rocks and rhyolitic ignimbrites from the Temoris and Sierra Guazapares formations, respectively. Within the Palmarejo district, U-Pb age data also record Early Miocene dates from the rhyolitic in composition La Patria dike (23.0 ± 0.5 Ma) and the Guadalupe dome (24.2 ± 0.4 Ma) (Galvan-Gutierrez, 2012). The new U-Pb age data from this study are consistent with the ignimbrite ages observed in the Guazapares and Palmarejo regions. Figure 36 is the TAS diagram for the samples analyzed in this study with respect to the Sierra Guazapares and Temoris formations (U-Pb age

24.5 to 23 Ma) (blue dashed line) of Murray et al. (2013). The geochemical compositions of the Basaseachic-Tomochic area samples (Ar-Ar ages 33.4 to 28.1 Ma) of McDowell, (2007) are also included for reference. The U-Pb age data from Guerra Al Tirano at 23.4 ± 0.4 Ma and Guadalupe Norte at 23.7 ± 1.1 (Figure 26 – A-C) are attributed to the Early Miocene ignimbritic pulse (Figure 26 – E). Age data from the San Francisco area recorded at 28.1 ± 1.0 Ma is consistent with Early Oligocene ignimbritic pulse (Figure 26– D). The timing of the ignimbrite pulses coincide with the ages observed in the Palmarejo district and adjoining areas of the northern SMO (Figure 37). Therefore, the timing of the ignimbrite flare-up in the Palmarejo district is confine to the Early Oligocene to Early Miocene.

5.3 ORIGIN OF MAGMAS

The origin of magmas which generated large volumes of silicic volcanic rocks in North America during the Cenozoic has been a controversial topic amongst researchers. Many hypotheses evolve around the crustal and mantle contributions with respect to the plate tectonic configuration at the time of the ignimbrite flare-up of the SMO (e.g. Ferrari et al., 2002, 2007; Bryan et al., 2008, 2013). One interpretation is that the ignimbrite flare-up was produced by solely by a fractional crystallization process from basaltic parental magmas (e.g. Cameron et al., 1980a). It is suggested that the rhyolitic ignimbrites were produced from crystal fractionation of andesitic parental magmas (e.g. Smith et al., 1996). On the contrary, others have suggested that the generated rhyolites are entirely due to partial melting of the crust (e.g., Ruiz et al., 1988a, 1990). Zircon inheritance age data indicate that multiple crustal contributions from Proterozoic, Mesozoic (xenoliths), and Tertiary sources were likely involved in the ignimbrite flare-up (e.g. Bryan et al., 2008). Another interpretation is that the ignimbrite flare-up is not a product of

assimilation and fractional crystallization processes alone, but rather was dominantly produced by intrusion of large amount of mafic melt in the crust (Ferrari et al., 2013).

The petrological, geochemical, and Hf isotopic data give insights into the origin, source and tectonic setting associated to these ignimbrites. Magma sources may be derived from crustal melts and mantle melts (fractional crystallization) or mixing of both processes (assimilation). A crustal melt component results in negative $\epsilon_{\text{Hf}}(t)$ compositions with inheritance from pre-existing crust. On the contrary, a mantle melt component results in positive $\epsilon_{\text{Hf}}(t)$ compositions. An inheritance poor magma is much hotter than an inheritance rich magma, therefore crustal melting is less likely as it would ascend much faster and at very shallow depths. No zircon inheritance was observed as the overall variation of individual analyses ranged from 21 to 32 Ma with majority (89 %) of the total analyses yielding ages between 21 to 23 Ma. Also, Murray et al. (2013) did not report any inheritance in his Guazapares age data. Overall the 49 analyses on selected zircons yielded $\epsilon_{\text{Hf}}(t)$ composition varying from -0.6 to +7.8 (Figure 28). The combined samples collected in Palmarejo and Guazapares yielded a radiogenic and positive weighted mean $\epsilon_{\text{Hf}}(t)$ of 3.3 ± 0.5 (MSWD = 3.0, $n = 47$) (Figure 27 – F). In general, the MSDW is greater than 1.4. This indicates large scattering in the data, which may be indicative of mixing of different sources rather than a uniform, heterogeneous source. During the post-Laramidic extension, there is contribution of mantle-derived sources through asthenospheric decompression which may mix with sub-continental lithospheric mantle (SCLM). Another end-member which can influence magma composition is evolved, non-radiogenic crustal fluids from the widespread hydrothermal activity associated with epithermal mineralization.

5.4 TECTONIC IMPLICATION

The origin of magmas and the observed positive $\epsilon_{\text{Hf}}(t)$ compositions have direct tectonic implications for the subducting plate margin configuration at the time of the emplacement of plutons and the post-Laramidic ignimbrites. Mahar and Goodell (In-revision) proposed a model for the emplacement of Cretaceous granodioritic plutons from the Cuenca De Oro (CDO) region. Based on a Sr/Y vs Y plot they determined the CDO plutons are not oceanic slab derived, therefore the generated heat from the subducting Farallon slab partially melted the SCLM producing basaltic magmas which differentiate and ascend to generate the inheritance-poor granodioritic plutons with zircon $\epsilon_{\text{Hf}}(t)$ compositions varying from 0 to 6.5 and U/Pb ages from 90 to 65 Ma (Mahar and Goodell, In-revision). The extinction of the Farallon plate was followed by the post-Laramidic extension which generated the ignimbrite flare-up. A slab roll-back model (Figure 38) is proposed as the boundary force which produced asthenospheric upwelling, thus partially melting the SCLM to produce basaltic magmas which differentiated and ascended to generate the ignimbritic pulses observed in the Palmarejo district with $\epsilon_{\text{Hf}}(t)$ compositions varying from 0.6 to 4.7 and U/Pb ages from 28 to 23 Ma.

5.5 TIMING OF EPITHERMAL MINERALIZATION IN NORTHERN MEXICO

Epithermal deposit types have proven to be of significant importance, as they are very rich in Ag, regularly placing Mexico on the top list of major Ag producers year after year. The tectonic history of Mexico has been favorable for the economic mineralization of epithermal deposit types (Staude and Barton, 2001). Extensional periods in the geologic record have provided the framework for the shallow emplacement of Ag-Au \pm (Pb, Zn, Cu) epithermal vein deposits along NW-SE structural trends in northwest Mexico (Staude and Barton, 2001).

Constraining the timing and genesis of the Mexican epithermal deposits has been the subject of extensive studies (e.g. Staude and Barton, 2001; Albinson et al., 2001; Camprubi et al., 2003; Camprubi and Albinson 2006; Clark and Fitch, 2009). Direct dating of adularia and sericite is limited; therefore, it is assumed that the age of the volcanic host rocks is the approximate age of epithermal deposits (Camprubi et al., 2003). Three main phases of mineralization have been proposed following volcanic activity in the SMO: phase 1 is related to the Laramide magmatism between 48 and 40 Ma; phase 2 is related to Early Oligocene ignimbritic pulse between 40 and 27 Ma; and a third phase related to the Early Miocene ignimbritic pulse between 20 and 18 Ma (Camprubi et al., 2003).

Geological investigations of host rocks in the Palmarejo district by Galvan-Gutierrez (2012) indicate that Late Cretaceous to Eocene volcano-sedimentary mudstones, sandstones, breccias intercalated with distinctive amygdaloidal basalts of the LVS are unconformably overlain by Oligocene ignimbrites of the UVS. U-Pb age data established that rhyolitic dykes and domes intruded the LVS in the Late Oligocene to Early Miocene. The Guadalupe rhyolite dome was emplaced at 24.2 ± 0.4 Ma and the La Patria rhyolite dyke intruded at 23.0 ± 0.5 Ma (Galvan-Gutierrez, 2012). The cross-cutting relationships between mineralization and the rhyolite dyke at La Patria and the Guadalupe dome helped constrain the age of epithermal mineralization in the Palmarejo district to the Late Oligocene to Early Miocene. The Guadalupe Norte dome dated in this study is closely related and contemporaneous to the rhyolitic intrusions which cross-cut the Independencia and Los Bancos veins. Sample GPN2 is dated at 23.7 ± 1.1 Ma. Therefore, on the basis of the cross-cutting relationships observed in the district, the mineralization at the Independencia – Los Bancos is inferred to be of Late Oligocene to Early Miocene age (Figure 39).

The general agreement is that the mineralization is hosted in the LVS and is contemporaneous to the volcanic activity of the UVS. However, studies in the Guazapares district, 9 km NW of Guadalupe Norte, have raised doubts about whether the host rocks in fact are part of the LVS (e.g., Murray et al., 2013; Murray and Busby, 2015). Previous workers placed the andesitic rocks that underlie the silicic volcanic rocks into the LVS (e.g., Minjarez-Sosa et al., 2002; Ramírez-Tello and García-Peralta, 2004). However, new mapping and geochronological data determined that the andesitic rocks are within the silicic rocks of the UVS (Murray and Busby, 2015). The andesitic rocks dated in the Guazapares district, specifically from the Temoris formation, have emplacement ages between 27 to 24.5 Ma. The Temoris formation is characterized by having a basal section of amygdaloidal basalts, basaltic andesites, and andesitic intrusions, lavas and autoclastic flow breccias, with locally interbedded silicic tuffs. It consists of a middle section of andesite intrusions and flow-banded andesite lavas and an upper section of distal thin non-welded rhyolitic ignimbrites and tuffaceous volcanoclastic deposits (Murray et al., 2013). These characteristics are similar to the stratigraphic sequence (Figure 14) from the Ktal to Ktat units of the Palmarejo district, which are interpreted as Cretaceous to Eocene andesites, volcano-sediments, amygdaloidal basalts to andesites, andesitic intrusions and interbedded rhyolitic tuffs of the LVS. These rocks may correspond to the same lithologic sequence as they are in short proximity from each other, which infers that mineralization is actually hosted in the UVS. Similarities are apparent in the stratigraphic sequence correlation (Figure 40) between the lithologic units from Palmarejo and Murray et al. (2013) Guazapares district section. To provide validity to these observations, further geochronological data is needed to constrain the ages of the andesitic rocks from the Palmarejo district.

5.5.1 Geochemical Processes

The statistical data provides clues about the geochemical processes or trends involved in the ore body formation. Results from the multivariate analyses of the Independencia vein show the behavior of elements within the ore fluids as they were being deposited. The variation matrices (Table 4 – A-D) indicate the proportional relationships observed by the relative low log-ratio variances (values below one) between Ag/Au, As/Fe, Fe/Mn, Cu/Pb, Cu/Zn, Fe/Sb, Mn/Zn, Pb/Zn and Sb/Zn within the mineralized structure. The highest proportionalities are between Ag/Au and Pb/Zn with variation coefficients of 0.68 and 0.44, respectively. These behaviors are consistent in the PCA biplots (Figure 28 – A-D) which displays low variability between Ag and Au and between Pb and Zn as the links between the element pairs are short. High variability is displayed between Ag-Fe, Ag-As, Au-Fe and Au-As. The highest proportionality comes from Ag and Au which display a short link between them suggesting a close association within the Independencia deposit. The high clr-variance of Ag and Au may suggest that either the way they are deposited or leached, causes their variability to be much higher than all the other elements. This behavior may be explained by the mineral assemblages of silver sulfosalts, Au as electrum, sphalerite and galena found within the Independencia, which is classified as an intermediate-sulfidation epithermal vein deposit (Figures 1 and 2).

The ore mineralogy is largely controlled by the composition of the ore fluids, partially caused by the differences in solubilities of Au, Ag and base metals as a function of the available sulfide or chloride complexes as the transportation means (Sillitoe and Hedenquist, 2003). Another correlation with ore fluid is observed between salinity and metal content. There is a general increase in salinity with increasing base metal content and Ag/Au ratio (Albinson et al., 2001). The maximum salinity of individual Zn-Pb-Ag deposits is 12 to 23 wt. percent NaCl eq.,

the Ag rich Zn-Pb occurrences range from 7.5 to 12 wt. % NaCl eq. in contrast with the Ag-rich precious metal deposits which have maximum salinities of 3.5 to 7.5 wt. percent NaCl eq. (Albinson et al., 2001). Salinities of ore fluids from the Palmarejo district (Figure 16) range from 1.3 to 7.8 wt. % NaCl equiv. (Miller, 1988; Galvan-Gutierrez, 2012). The Ag, Au and base metal correlations observed in the statistical data analysis along with the general range in salinities give insights into district-scale ore fluid processes involved in the precipitation of precious metals.

The Independencia – Los Bancos deposit is defined as an intermediate-sulfidation epithermal vein deposit located in the Palmarejo district. The regional stress regimes that affected the Palmarejo district region in southwest Chihuahua, allowed for the NW-SE trending emplacement of mineralization along normal faults caused by Tertiary extension in the northwestern SMO. The Independencia – Los Bancos geologic model is constructed considering this general NW trend. The veins and intrusive bodies follow the tendency of the structural trend observed in the Palmarejo district. The Independencia structure acts as a normal fault dipping $\sim 70^\circ$ to the NE, offsetting the east block downwards. The geologic model helps to visualize the 3D geometry of ore bodies, whereas interpolation models helps to investigate the spatial distribution of metals and see the relationships between them.

6. Conclusion

Recent studies in the northwest SMO occidental have shown evidence indicating that the Late Oligocene (32 to 28 Ma) and Early Miocene (24 to 20 Ma) volcanic activity, which produced the ignimbrite flare-up, is largely syn-genetic with the post-Laramidic Tertiary extension (e.g. Murray et al., 2013; Murray and Busby, 2015). The U-Pb geochronological data in this study record ages of the distinctive Late Oligocene and Early Miocene pulses. These ignimbritic pulses are recorded at 28.1 ± 1.0 Ma in the San Francisco area and at 23.7 ± 0.4 Ma and 23.7 ± 1.1 Ma at Guerra Al Tirano and Guadalupe Norte, respectively. The timing of these pulses coincide with the ages observed in the Palmarejo district and adjoining areas (Figure 37).

The origin of magmas which generated large volumes of silicic volcanic rocks in North America during the Cenozoic has been a topic of debate topic and the basis for many studies and interpretations. Insights into the origin, source and tectonic setting associated to these ignimbrites are obtained from petrological, geochemical, and Hf isotopic data. Selected zircons yielded ϵ_{Hf} (t) composition varying from -0.6 to +7.8 with majority (85%) of the samples ranging from +1.0 to +5.8. Since no zircon inheritance is observed, a crustal melting scenario is discarded. It is inferred that during the post-Laramide extension, there is contribution of mantle derived sources through asthenospheric decompression which may mix with sub-continental lithospheric mantle (SCLM) to produce basaltic magmas which differentiate and ascend to generate the ignimbrite flare-up. Another possible end-member which influences the magma composition may be evolved non-radiogenic crustal fluids from the widespread hydrothermal activity associated to epithermal mineralization.

The extensional periods in northwest Mexico provided the framework for the shallow emplacement of Ag-Au \pm (Pb, Zn, Cu) epithermal vein deposits along NW-SE structural trends

(Staude and Barton, 2001). The extensional fractures served as the migration paths for the ore fluids and eventual deposition. Direct dating of adularia and sericite is limited, therefore it is inferred that the age of the volcanic host rocks is an approximation of the age of epithermal deposits based on cross-cutting relationships. The mineralization age at the Independencia – Los Bancos deposit is determined to be approximate 23 Ma on the basis of the cross-cutting relationships between the mineralized veins and the district rhyolitic porphyry bodies, domes and dykes (23.7 ± 1.1 Ma, 24.2 ± 0.4 Ma, and 23.0 ± 0.5 Ma, respectively) of similar origin.

The different statistical treatments conducted in this study show comparable results which revealed ore fluid characteristics of an intermediate-sulfidation epithermal deposit. The PCA suggest that Ag-Au mineralization is distinct from the Pb-Zn mineralization, possibly a different stage of mineralization. The mineral assemblage of silver sulfosalts, electrum, sphalerite, and galena are consistent with the statistical data results which show proportional relationships between Ag and Au and Pb and Zn. The most proportional ratios were those of Ag/Au and Pb/Zn with variation. The ore mineralogy of an intermediate-sulfidation epithermal deposit is controlled by the ore fluid composition and salinities ranging from 3.5 to 7.5 wt. percent NaCl eq. Salinities of ore fluids from the Palmarejo district range from 1.3 to 7.8 wt. % NaCl equiv. The geologic model aids to visualize the geometry of the deposit and characterized the variability and distribution of precious metals, which has many implications for exploration and mining. This study explored the geochemical characteristics, magma sources, transport conduits, and depositional controls of mineralizing fluids to provide new insights about the metallogenesis in southwest Chihuahua area.

References

- Aguirre-Díaz, G. J. & Labarthe-Hernandez, G., 2003. Fissure ignimbrites: fissure-source origin for voluminous ignimbrites of the Sierra Madre Occidental and its relationship with basin and range faulting. *Geology*. v. 31, p. 773-776.
- Aguirre-Díaz, G.J. and McDowell, F.W., 1993. Nature and timing of faulting and synextensional magmatism in the southern Basin and Range, central-eastern Durango, Mexico. *Geological Society of America Bulletin*, v. 105, p. 1435 - 1444.
- Albinson, T., Norman, D.I., Cole, D., Chomiak, B.A., 2001. Controls on formation of low-sulfidation epithermal deposits in Mexico: constraints from fluid inclusion and stable isotope data. *Society of Economic Geologists, Special Publication*, 8, 1-32.
- Alvarez, L.G., Suarez-Vidal, F., Mendoza-Borunda, R., Gonzalez-Escobar, M., 2009. Bathymetry and Active Geological Structures in the Upper Gulf of California. *Boletín de la Sociedad Geológica Mexicana*. v. 61, p.129-141.
- Aranda-Gomez, J.J., Henry, C.D., Luhr, J.F., 2000. Evolucion tectonomagmatica post-paleocena de la Sierra Madre Occidental y de la porcion meridional de la provincia tectonica de Cuencas y Sierras, Mexico. *Boletín de la Sociedad Geológica Mexicana*. v. 53, p. 59-71.
- Axen, G., 1995. Extensional segmentation of the main gulf escarpment, Mexico and United States. *Geology*. v. 23, p. 515-518.
- Best, M. G. & Christiansen, E. H., 1991. Limited extension during peak Tertiary volcanism, Great Basin of Nevada and Utah. *Journal of Geophysical Research*. v. 96, p. 13509-13528.
- Birak, D. J., and Blair, K., 2012. Technical Report for the Palmarejo Project SW Chihuahua State, Mexico. Prepared for Coeur d'Alene Mines Corp.
- Bryan, S. E., Ferrari, L., Reiners, P. W., Allen, C. M., Petrone, C. M., Ramos Rosique, A.R., Campbell, I.H., 2008. New Insight into Crustal Contributions to Large-volume Rhyolite Generation in the Mid Tertiary Sierra Madre Occidental Province, Mexico, Revealed by U-Pb Geochronology. *Journal of Petrology*, v. 49, p. 47-77.
- Bogie, I., Lawless, J.V., 1987. Controls on the hydrology of large volcanically hosted geothermal systems: implications for exploration for epithermal mineral deposits, in Proceedings Pacific Rim Congress87: Parkville, Victoria, Australia, *Australasian Institution of Mining and Metallurgy*, 57-60.

- Bohannon, R., and Parsons, T., 1995. Tectonic implications of post–30 Ma Pacific and North American relative plate motions. *Geological Society of America Bulletin*. v. 107, p. 937–959.
- Cameron, K. L., Nimz, G. J., Kuentz, D., Niemeyer, S., and Gunn, S., 1989. Southern Cordilleran basaltic andesite suite, southern Chihuahua, Mexico: A link between Tertiary continental arc and flood basalt magmatism in North America. *Journal of Geophysical Research*. v. 94, p. 7817–7840.
- Cameron, M., Bagby, W. C. & Cameron, K. L., 1980a. Petrogenesis of voluminous mid-Tertiary ignimbrites of the Sierra Madre Occidental. *Contributions to Mineralogy and Petrology*. v. 74, 271–84.
- Campa, M. F., and Coney, P. J., 1983. Tectono-stratigraphic terranes and minerals resource distributions in Mexico. *Canadian Journal of Earth Sciences*, v. 20, p. 1040–1051.
- Camprubi, A., and Albinson, T., 2007. Epithermal deposits in México: Update of current knowledge, and an empirical reclassification. *Geological Society of America Special Papers*, 2007, 422, p. 377–415,
- Camprubi, A., Ferrari, L., Cosca, M., Cardellach, E., and Canals, A., 2003. Age of epithermal deposits in Mexico: Regional significance and links with the evolution of Tertiary volcanism. *Economic Geology and the Bulletin of the Society of Economic Geologists*, v. 98, p. 1029–1037.
- Cecil, R., Gehrels, G., Patchett, J., Ducea, M., 2011. U–Pb–Hf characterization of the central Coast Mountains batholith: implications for petrogenesis and crustal architecture. *Lithosphere* v. 3, p. 247–260.
- Centeno-García, E., Olvera-Carranza, K., Corona Esquivel, R., Camprubi, A., Tritlla, J., and Sanchez-Martinez, S., 2003a. Depositional environment and paleogeographic distribution of the Jurassic-Cretaceous arc in the western and northern Guerrero Terrane, Mexico. *GSA 99th Cordilleran Section Annual Meeting Abstracts with Programs*, v. 35, n. 4, p. 76.
- Clark, K. F., & Fitch, D. C., 2009. Evolución de los depósitos metálicos en el tiempo y el espacio en México. In: Clark, K. F., Salas-Piza, G., & Cubillas-Estrada, R. (Eds.), *Geología Económica de México*, II Edición, Servicio Geológico Mexicano, p. 62–133.
- Craig, J.R., Vaughan, D.J., Skinner, B.J., 1996, *Resources of the Earth. Origin, use, and environmental impact*, Segunda edición: New Jersey, New Jersey, E.U.A., Prentice Hall, 472 p.
- Coeur Mining Inc., *Coeur Mining to Acquire Paramount Gold and Silver*. *Coeur Mining to Acquire Paramount Gold and Silver*. News Release. 17 Dec. 2014. Web. 4 Apr. 2015.

- Coeur Mining Inc., <http://www.coeur.com/company/fact-sheet#.VxFmhjBrjIU>. Web. 4 Apr. 2015.
- Corfu F., Hanchar, J.M., Hoskin, P.W.O., Kinny, P., 2003. Atlas of Zircon Textures. *Reviews in Mineralogy and Geochemistry*, v. 53, p. 469-500.
- Damon, P.E., Shafiqullah, M., and Clark, K., 1983. Geochronology of the porphyry copper deposits and related mineralization in Mexico. *Canadian Journal of Earth Sciences*. v. 20, p. 1052–1071.
- Davis, G.H., and Coney, P.J., 1979. Geological development of metamorphic core complexes. *Geology*. v. 7, p. 120–124. doi: 10.1130/0091-7613(1979)7<120:GDOTCM>2.0.CO;2.
- Dickinson, W.R., 2002. The Basin and Range Province as a composite extensional domain. *International Geology Review*. v. 44, p. 1–38.
- Dreier, J., 1984. Regional tectonic control of epithermal veins in the Western United States and Mexico. In: Wilkins, J. (Ed.), Gold and Silver Deposits of the Basin and Range Province, Western U.S.A., *Arizona Geological Society Digest*, v. 15, p. 28-50.
- Duque-Trujillo, J., Ferrari, L., Orozco-Esquivel, T., Lopez-Martinez, M., Lonsdale, P., Bryan, S., Kluesner, J., Pinero-Lajas, D., Solari, L., 2014. Timing of rifting in the Southern Gulf of California and its conjugate margins: insights from the plutonic record. *Geological Society of America Bulletin*, B31008-1; doi:10.1130/B31008.1.
- Einaudi, M.T., Hedenquist, J.W., and Inan, E.E., 2003. Sulfidation state of fluids in active and extinct hydrothermal systems: Transitions from porphyry to epithermal environments. *Society of Economic Geologists Special Publication* v. 10.
- Emmons, W.H., 1918. The principles of economic geology. New York, McGraw-Hill, p. 606.
- Feinstein, M.N., 2007. Contributions to the Geology of the Cuenca de Oro: Chihuahua, Mexico. Department of Geological Sciences. University of Texas at El Paso, El Paso, TX, p. 168.
- Ferrari, L., Lopez-Martínez, M., Orozco-Esquivel, T., Bryan, S.E., Duque-Trujillo, J., Lonsdale, P., Solari, L., 2013. Late Oligocene to Middle Miocene rifting and synextensional magmatism in the southwestern Sierra Madre Occidental, Mexico: the beginning of the Gulf of California rift. *Geosphere*, v. 9, p. 1161-1200.
- Ferrari, L., Lopez-Martínez, M., Rosas-Elguera, J., 2002. Ignimbrite flare-up and deformation in the southern Sierra Madre Occidental, western Mexico: implications for the late subduction history of the Farallon plate. *Tectonics*, v. 21, 1-24.

- Ferrari, L., Valencia-Moreno, M. & Bryan, S. E., 2007. Magmatism and tectonics of the Sierra Madre Occidental and their relation to the evolution of the western margin of North America. *Geological Society of America, Special Papers* 442, 1-39.
- Frost, B.R. and Frost, C.D., 2008. A geochemical classification for feldspathic igneous rocks. *Journal of Petrology*, v. 49, p. 1955-1969.
- Galvan-Gutierrez, V.H., 2005. Regional and Local Patterns of Mineralization in the Lower Batopilas and Urique Rivers in Sierra Madre of Chihuahua, Mexico. University of Texas, El Paso, p. 115.
- Galvan-Gutierrez, V.H., 2012. Palmarejo Carbonate-Base Metal Epithermal Ag-Au District, Chihuahua, Mexico: [Ph.D. dissertation] University of Tasmania.
- Gans, P. B., Mahood, G. A. & Schermer, E. R., 1989. Synextensional magmatism in the Basin and Range Province: a case study from the eastern Great Basin. *Geological Society of America Special Papers*. v. 233, 1-53.
- Gehrels, G.E., Valencia, V.A., Ruiz, J., 2008. Enhanced precision, accuracy, efficiency, and spatial resolution of U–Pb ages by laser ablation-multicollector-inductively coupled plasma-mass spectrometry. *Geochemistry, Geophysics, Geosystems* 9, Q03017.
- Gonzalez-Leon, C.M., McIntosh, W.C., Lozano-Santacruz, R., Valencia-Moreno, M., Amaya Martinez, R., and Rodríguez-Castañeda, J.L., 2000. Cretaceous and Tertiary sedimentary, magmatic, and tectonic evolution of north-central Sonora (Arizpe and Bacanuchi quadrangles), northwest Mexico. *Geological Society of America Bulletin*, v. 112, p. 600–610.
- Goodell, P.C., 1995. Porphyry copper deposits along the Batopilas lineament, Chihuahua, Mexico. In: Pierce, F.W., Bolm, J.G. (Eds.), *Porphyry Copper Deposits of the American Cordillera. Arizona Geological Society Digest*, v. 20, p. 544.
- Goodell, P.C., Martinez-Peña, C., Galvan-Gutierrez, V. H., 2015. Lineament Analysis, Mineral Occurrences, and Mines of the Southwest Chihuahua Region. Abstract submitted to the XXXI International Mining Congress, Acapulco, Mexico, 2015.
- Harry, D. L., D. S. Sawyer, and W. P. Leeman, 1993. The mechanics of continental extension in western North America: Implications for the magmatic and structural evolution of the Great Basin. *Earth and Planetary Science Letters*. v. 117, p. 59–71, doi:10.1016/0012-821X(93)90117-R.
- Hastie, A.R., Kerr, A.C., Pearce, J.A., Mitchell, S.F., 2007. Classification of Altered Volcanic Island Arc Rocks using Immobile Trace Elements: Development of the Th-Co Discrimination Diagram. *Journal of Petrology*. v. 48, p. 2341-2357.

- Hedenquist, J.W., 1987. Mineralization associated with volcanic-related hydrothermal systems in the Circum-Pacific Basin, in Horn, M.K., ed., Circum Pacific Energy and Mineral Resources Conference, 4th, Singapore, 1986. *Transactions: American Association of Petroleum Geologists*, p. 513–524.
- Hedenquist, J.W., Arribas, A. Jr., Urien-Gonzalez, E., 2000. Exploration for epithermal gold deposits. *Reviews in Economic Geology*, v. 13, p. 245-277.
- Henry, C.D., McIntosh, W., McDowell, F.W., Lipman, P.W., Chapin, C.E., Richardson, M.T., 2010. Distribution, timing, and controls of the mid-Cenozoic ignimbrite flareup in western North America. *Geological Society of America*. v. 42. P. 144.
- Humphreys, E.D., 1995. Post-Laramide removal of the Farallon slab, western United States. *Geology*. v. 23, p. 987–990, doi: 10.1130/0091-7613.
- Instituto Nacional de Estadística y Geografía, 2005, Marco Geoestadístico Municipal. Consulted on May 6, 2015. <http://www3.inegi.org.mx/sistemas/mexicocifras/datos-geograficos/08/08030.pdf>
- Irvine, T.N., and Baragar, W.R.A., 1971. A guide to the chemical classification of the common volcanic rocks. *Canadian Journal of Earth Sciences*. v. 8, p. 523-548.
- Kerr, P., Gustin, M., Hlorgbe, D., Glanvill, J., Mondragon, R., Hoffer, M., O’Prey, M., 2015. Technical Report for the Palmarejo Complex SW Chihuahua State, Mexico. NI 43-101 Technical Report.
- Le Bas, M., Le Maitre, R., Streckeisen, A., and Zanettin, B., 1986. A chemical classification of volcanic rocks on the total alkali-silica diagram. *Journal of Petrology*. v. 27, p. 745–750.
- Leeman, W. P., and D. L. Harry, 1993. A binary source model for extension- related magmatism in the Great Basin, western North America. *Science*. v. 262, p. 1550–1554.
- Levitan, D.M., Zipper, C. E., Donovan, P., Schreiber, M. E., Seal II, R. R., Engle, M. A., Chermak, J. A., Bodnar, R. J., Johnson, D. K., Aylor Jr., J. G., 2014. Statistical analysis of soil geochemical data to identify pathfinders associated with mineral deposits: An example from the Coles Hill uranium deposit, Virginia, USA. *Journal of Geochemical Exploration*, <http://dx.doi.org/10.1016/j.gexplo.2014.12.012>.
- Mahar, M.A., 2015. Zircon-apatite U–Pb Geochronology, Zircon Hf Isotope Composition and Geochemistry of Granite Batholith in the Northern Mexico: Implications for Tectonomagmatic Evolution of Southern Cordillera. Abstract Submitted to the American Geophysical Union 2015 Conference, San Francisco, USA.
- Mahar, M.A. and Goodell, P.C., In-review. Tectono-magmatic evolution of the Chihuahua-

- Sinaloa border region in northern Mexico: Insights from zircon-apatite U–Pb geochronology, zircon Hf isotope composition and geochemistry of granodiorite intrusions. *Lithos*.
- Mahar, M.A., Mahéo, G., Goodell, P.C., Pavlis, T.L., 2014. Age and origin of post collision Baltoro granites, south Karakoram, North Pakistan: Insights from insitu U–Pb, Hf and oxygen isotopic record of zircons. *Lithos* v. 205, p. 341–358.
- Mahar, M.A., Ibrahim, T.M.M., Goodell, P.C., 2014. Provenance of the heavy mineral-enriched alluvial deposits at the westcoast of the Red Sea. Implications for evolution of Arabian–Nubian crust. *Journal of African Earth Sciences*. v. 100, p. 510–523.
- Mahar, M.A., Mahéo, G., Goodell, P.C., Pavlis, T.L., 2016. Timing and origin of migmatitic gneisses in south Karakoram: Insights from U–Pb, Hf and O isotopic record of zircons. *Journal of Asian Earth Sciences*. v. 120, p. 1–16.
- Minjarez-Sosa, I., Montano-Jimenez, T.R., Ochoa-Granillo, J.A., Grijalva-Noriega, F.J., Ochoa-Landín, L.H., Herrera-Urbina, S., Guzman-Espinosa, J.B., Mancilla-Gutierrez, A.A., 2002. Carta Geologico-Minera Ciudad Obregon G12-3 Sonora, Chihuahua y Sinaloa. Servicio Geologico Mexicano.
- Masterman, G., Phillips, K., Stewart, H., Laurent, I., Beckton, J., Cordery, J., Skeet J., 2005. Palmarejo Silver-Gold Project, Chihuahua, México: Discovery of a Ag–Au Deposit in The Mexican Sierra.
- McQuarrie, N., and Oskin, M., 2010, Palinspastic restoration of NAVDat and implications for the origin of magmatism in southwestern North America. *Journal of Geophysical Research*. v. 115, no. B10, doi: 10.1029/2009JB006435.
- McDowell, F.W., 2007. Geologic Transect across the Northern Sierra Madre Occidental Volcanic Field, Chihuahua and Sonora, Mexico. In: *Geological Society of America Digital Map and Chart Series*, v. 6.
- McDowell, F.W., Clabaugh, S.E., 1979. Ignimbrites of the Sierra Madre Occidental and their relation to the tectonic history of western Mexico. In: Chapin, C.E., Elston, W.E. (Eds.), *Ash-Flow Tuffs: Geological Society of America Special Paper*, v. 180, p. 113–124.
- McDowell, F.W., Keizer, R.P., 1977. Timing of mid-Tertiary volcanism in the Sierra Madre Occidental between Durango City and Mazatlan, Mexico. *Geological Society of America Bulletin*. v.88, p. 1479–1487.
- McDowell, F.W., Mauger, R.L., 1994. K_{Ar} and U_{Pb} zircon chronology of Late Cretaceous and Tertiary magmatism in central Chihuahua State, Mexico. *Geological Society of America Bulletin*. v. 106, p. 118–132.

- McDowell, F.W., McIntosh, W.C., 2012. Timing of intense magmatic episodes in the northern and central Sierra Madre Occidental, western Mexico. *Geosphere*. v. 8, p. 1502-1526.
- Miller, R. A., 1988. Geology of the Llanitos Mining District, Chihuahua, Mexico: [M.S. thesis] The University of Texas at El Paso.
- Moon, C. J., Whateley, M. E. G., Evans, A. M., 2006. Introduction to Mineral Exploration. Blackwell Publishing, Oxford, UK.
- Murray, B. P., Busby, C. J., Ferrari, L., Solari, L. A., 2013. Synvolcanic crustal extension during the mid-Cenozoic ignimbrite flare-up in the northern Sierra Madre Occidental, Mexico: Evidence from the Guazapares Mining District region, western Chihuahua. *Geosphere*, v. 9, no. 5. doi:10.1130/GES00862.1.
- Murray, B. P., and Busby, C. J., 2015. Epithermal mineralization controlled by synextensional magmatism in the Guazapares Mining District of the Sierra Madre Occidental silicic large igneous province, Mexico. *Journal of South American Earth Sciences*, v. 58, p. 54-71.
- Ortega-Gutierrez, F., Elias-Herrera, M., Moran-Zenteno, D.J., Solari, L., Luna-Gonzalez, L., Schaaf, P., 2014. A Review of Batholiths and Other Plutonic Intrusions of Mexico. *Gondwana Research*. v. 26. P. 834-868.
- Palarea-Albaladejo, J., Martín-Fernández, J.A., Buccianti, A., 2014. Compositional methods for estimating elemental concentrations below the limit of detection in practice using R. *Journal of Geochemical Exploration*, v.141, p. 71-77.
- Parsons, T., 1995. The Basin and Range Province, in Continental Rifts: Evolution, Structure, Tectonics, K. H. Olsen (Editor), Elsevier, Amsterdam, 277- 324.
- Pearce, J.A., Harris, N.B.W., and Tindle, A.G., 1984. Trace element discrimination diagrams for the tectonic interpretation of granitic rocks. *Journal of Petrology*. v. 25, p. 956-983.
- Perez-Segura, E., 2013. Caracterización de oro en las muestras: 133676, 79963, 77782, 132877, 134510 y 132629 de Paramount Gold de México. Private Report.
- Ramírez-Tello, E., García-Peralta, _A.A., 2004. Carta Geologico-Minera Temoris G12eB39 Chihuahua. Servicio Geologico Mexicano.
- Rasmussen, H., Nasi, C., Molina, C., Ochoa, P., Hohbach, P., 2014. Geology and Exploration History of the Palmarejo Silver and Gold District, Chihuahua, Mexico. *Society of Economic Geologists Guidebook Series*, v. 42, p. 37-48.
- Reimann, C., Filzmoser, P., Garrett, R.G., Dutter, R., 2008. Statistical data analysis explained: applied environmental statistics with R. John Wiley & Sons, Chichester, UK.

- Rollinson, H., 1993. Using Geochemical Data: Evaluation, Presentation, Interpretation. Longman Group, London, UK.
- Ruiz, J., Patchett, P., and Arculus, R.J., 1988, Nd-Sr isotope composition of lower crustal xenoliths—Evidence for the origin of mid-Tertiary felsic volcanics in Mexico. *Contributions to Mineralogy and Petrology*. v. 99, p. 36–43.
- Sawkins, F.J., 1972. Sulfide ore deposits in relation to plate tectonics. *Journal of Geology*, v. 80, p. 377–397.
- Sedlock, R., and Ortega-Gutierrez, F. & Speed R. C. 1993, Tectonostratigraphic terranes and Tectonic Evolution of Mexico. *Geological Society of America, Special Papers*.
- Sillitoe, R. H., 1977. Metallic mineralization affiliated to subaerial volcanism. *Geological Society [London] Special Publication*, 7, p. 99–116.
- Sillitoe, R. H., 2010. “Comments on Geology and Exploration of the Palmarejo Epithermal Silver-Gold Deposit and Evirons, Chihuahua, Mexico”, private report prepared for Coeur d’Alene Mines Corp.
- Sillitoe, R. H., and Hedenquist, J. W., 2003. Linkages between Volcanotectonic Settings, Ore-Fluid Compositions, and Epithermal Precious Metal Deposits. *Society of Economic Geologists: Special Publication*, 10, p. 315-343.
- Smith, R. D., Cameron, K. L., McDowell, F. W., Niemeyer, S. & Sampson, D. E., 1996. Generation of voluminous silicic magmas and formation of mid-Cenozoic crust beneath north-central Mexico; evidence from ignimbrites, associated lavas, deep crustal granulites, and mantle pyroxenites. *Contributions to Mineralogy and Petrology*. v. 123, 375-389.
- Staude, J.-M. G., and Barton, M. D., 2001. Jurassic to Holocene tectonics, magmatism, and metallogeny of northwestern Mexico, *GSA Bulletin* v. 113; no.10; p. 1357-1374.
- Stock, J.M., and Hodges, K.V., 1989, Pre-Pliocene extension around the Gulf of California and the transfer of Baja California to the Pacific plate. *Tectonics*, v. 8, p. 99–115.
- Ward, P.L., 1991. On plate tectonics and the geologic evolution of southwestern North America. *J. Geophys. Res.* v. 96, p. 12479-12496.
- Wilson, S. E., Gustin, M. M., Brechtel, C., George, T., Pennstrom, W. J., Aguayo, P., 2013. Technical Report and Preliminary Economic Assessment for the San Miguel Project, Guazapares Mining District, Chihuahua, Mexico. Prepared for Paramount Gold and Silver Corp.
- White, N.C., Leake, M.J., McCaughey, S.N., Parris, B.W., 1995. Epithermal gold deposits of the southwest Pacific. *Journal of Geochemical Exploration*, v. 54, p. 87-136.

Wong, M.S., Gans, P.B., Scheier, J., 2010. The $^{40}\text{Ar}/^{39}\text{Ar}$ thermochronology of core complexes and other basement rocks in Sonora, Mexico: implications for Cenozoic tectonic evolution of northwestern Mexico. *J. Geophys. Res.* 115.

Table 1. List of studied samples and type of analyses performed.

| Sample Number | Sample ID | Lithology | Easting | Northing | Sampling Level | Sample Location | Multi-element Geochemical Analysis | LA-ICP-MS U-Pb zircon analysis | LA-ICP-MS ϵ Hf (t) zircon analysis |
|---------------|-----------|----------------------|------------|-------------|----------------|------------------|---------------------------------------|-----------------------------------|--|
| 1 | GAT-1 | rhyolitic ignimbrite | 760403.791 | 3024687.664 | surface | Guerra Al Tirano | x | x | x |
| 2 | GAT-2 | rhyolitic ignimbrite | 760406.637 | 3024710.426 | surface | Guerra Al Tirano | x | x | x |
| 3 | GAT-3 | rhyolitic ignimbrite | 760055.129 | 3024347.904 | surface | Guerra Al Tirano | x | x | x |
| 4 | SC | chalcedony | 770241.032 | 3029602.416 | surface | Santa Clara | x | | |
| 5 | SJ | ignimbrite | 769678.561 | 3031881.904 | surface | San Jose | x | | |
| 6 | SA | ignimbrite | 769441.731 | 3032444.375 | surface | San Antonio | x | | |
| 7 | SF-1 | rhyolite | 766155.715 | 3034857.08 | surface | San Francisco | x | x | x |
| 8 | SL-1 | ignimbrite | 742581.478 | 3040468.826 | surface | San Lorenzo | x | | |
| 9 | SL-2 | feldsite | 742456.602 | 3040477.673 | surface | San Lorenzo | x | | |
| 10 | CH-1 | basalt | 743701.46 | 3033954.85 | surface | Chinipas | x | | |
| 11 | GPN | rhyolitic ignimbrite | 759560 | 3028728 | surface | Guadalupe Norte | | x | x |
| 12 | MC-1 | altered ignimbrite | 767407.257 | 3035508.943 | 131 m | Montecristo | x | | |
| 13 | MC-2 | altered ignimbrite | 767465 | 3035460 | 286 m | Montecristo | x | | |
| 14 | MC-3 | altered ignimbrite | 767063 | 3035664 | 146 m | Montecristo | x | | |
| 15 | SF-2 | altered ignimbrite | 765982 | 3035039 | 43 m | San Francisco | x | | |
| 16 | SF-3 | altered ignimbrite | 766459 | 3034677 | 69 m | San Francisco | x | | |

Table 2. Major and trace element geochemical analysis by the Fusion ICP/MS methodology at Activation Laboratories Ltd.

| Sample ID | SiO ₂ % | Al ₂ O ₃ % | Fe ₂ O ₃ (T) % | MnO % | MgO % | CaO % | Na ₂ O % | K ₂ O % | TiO ₂ % | P ₂ O ₅ % | LOI % | Sc ppm | Be ppm | V ppm |
|-----------|--------------------|----------------------------------|--------------------------------------|-------|-------|-------|---------------------|--------------------|--------------------|---------------------------------|-------|--------|--------|-------|
| GAT-1 | 74.69 | 13.29 | 1.61 | 0.088 | 0.38 | 0.98 | 3.75 | 3.63 | 0.227 | 0.07 | 1.09 | 3 | 3 | 18 |
| GAT-2 | 73.86 | 13.89 | 1.63 | 0.079 | 0.42 | 1.07 | 4.01 | 3.74 | 0.239 | 0.08 | 1.06 | 3 | 2 | 19 |
| GAT-3 | 73.29 | 14 | 1.62 | 0.065 | 0.41 | 0.89 | 4.16 | 3.81 | 0.24 | 0.05 | 1.07 | 3 | 2 | 17 |
| SC | 95.99 | 0.23 | 1.49 | 0.061 | 0.02 | 0.15 | 0.03 | 0.03 | 0.002 | 0.005 | 1.06 | 0.5 | 0.5 | 12 |
| SA | 60.34 | 12.59 | 9.7 | 0.501 | 2.24 | 0.38 | 0.14 | 7.57 | 1.623 | 0.45 | 3.12 | 18 | 2 | 134 |
| SF-1 | 74.71 | 13.55 | 0.96 | 0.007 | 0.03 | 0.05 | 0.91 | 7.07 | 0.294 | 0.03 | 2.23 | 3 | 1 | 13 |
| SL-1 | 77.61 | 11.69 | 1.43 | 0.007 | 0.05 | 0.22 | 3.37 | 4.24 | 0.201 | 0.04 | 1.47 | 4 | 3 | 13 |
| SL-2 | 73.54 | 16.25 | 1.83 | 0.022 | 0.58 | 0.05 | 0.09 | 5.23 | 0.136 | 0.04 | 2.82 | 3 | 3 | 14 |
| CH-1 | 56.1 | 16.1 | 8.5 | 0.151 | 4.55 | 7.22 | 3.59 | 1.72 | 1.212 | 0.3 | 1.42 | 32 | 1 | 313 |
| SJ | 57.82 | 14.29 | 8.66 | 0.656 | 4.46 | 0.7 | 0.14 | 7.33 | 1.192 | 0.45 | 3.82 | 18 | 2 | 160 |
| MC-1 | 79.76 | 10.39 | 0.75 | 0.02 | 0.15 | 0.08 | 0.13 | 8.49 | 0.129 | 0.02 | 0.89 | 2 | 2 | 21 |
| MC-2 | 78 | 11.65 | 1.01 | 0.05 | 0.14 | 0.12 | 1.15 | 7.38 | 0.125 | 0.03 | 0.94 | 2 | 2 | 10 |
| MC-3 | 73.87 | 11.11 | 0.86 | 0.055 | 0.15 | 1.44 | 0.28 | 9.17 | 0.122 | 0.03 | 1.44 | 2 | 0.5 | 18 |
| SF-2 | 69.52 | 14.66 | 2.8 | 0.079 | 0.08 | 0.04 | 0.17 | 11.91 | 0.373 | 0.06 | 1.27 | 4 | 2 | 75 |
| SF-3 | 67.75 | 12.05 | 3.21 | 0.368 | 1.02 | 1.25 | 1.11 | 7.59 | 0.241 | 0.08 | 4.42 | 4 | 2 | 24 |

| Sample ID | Ba ppm | Sr ppm | Y ppm | Zr ppm | Cr ppm | Co ppm | Ni ppm | Cu ppm | Zn ppm | Ga ppm | Ge ppm | As ppm | Rb ppm | Nb ppm |
|-----------|--------|--------|-------|--------|--------|--------|--------|--------|--------|--------|--------|--------|--------|--------|
| GAT-1 | 1428 | 160 | 18 | 99 | 10 | 1 | 10 | 5 | 40 | 14 | 1 | 2.5 | 78 | 7 |
| GAT-2 | 1453 | 177 | 16 | 103 | 10 | 1 | 10 | 5 | 50 | 15 | 1 | 2.5 | 83 | 8 |
| GAT-3 | 1418 | 158 | 15 | 107 | 10 | 2 | 10 | 5 | 40 | 14 | 1 | 2.5 | 82 | 7 |
| SC | 13 | 3 | 5 | 2 | 40 | 0.5 | 10 | 480 | 10000 | 4 | 0.5 | 7 | <2 | 0.5 |
| SA | 3475 | 247 | 46 | 232 | 90 | 20 | 40 | 20 | 1110 | 15 | 1 | 30 | 241 | 14 |
| SF-1 | 2177 | 91 | 12 | 144 | 20 | 0.5 | 10 | 5 | 15 | 11 | 1 | 16 | 180 | 7 |
| SL-1 | 549 | 62 | 18 | 146 | 10 | 0.5 | 10 | 5 | 15 | 14 | 0.5 | 8 | 145 | 10 |
| SL-2 | 484 | 13 | 14 | 93 | 10 | 0.5 | 10 | 5 | 60 | 19 | 1 | 12 | 249 | 13 |
| CH-1 | 664 | 547 | 29 | 126 | 70 | 24 | 30 | 130 | 110 | 20 | 1 | 2.5 | 25 | 5 |
| SJ | 950 | 261 | 23 | 139 | 150 | 33 | 50 | 70 | 3660 | 19 | 2 | 10 | 222 | 5 |
| MC-1 | 1289 | 58 | 17 | 79 | 10 | 0.5 | 10 | 5 | 200 | 10 | 1 | 29 | 250 | 6 |
| MC-2 | 1645 | 78 | 16 | 77 | 10 | 0.5 | 10 | 5 | 90 | 11 | 1 | 21 | 205 | 6 |
| MC-3 | 1599 | 60 | 14 | 73 | 20 | 0.5 | 10 | 5 | 50 | 11 | 1 | 48 | 267 | 7 |
| SF-2 | 1423 | 123 | 25 | 149 | 10 | 2 | 10 | 5 | 90 | 12 | 2 | 138 | 340 | 6 |
| SF-3 | 1979 | 102 | 22 | 122 | 10 | 1 | 10 | 50 | 4420 | 19 | 0.5 | 71 | 184 | 5 |

| Sample ID | Mo ppm | Ag ppm | In ppm | Sn ppm | Sb ppm | Cs ppm | La ppm | Ce ppm | Pr ppm | Nd ppm | Sm ppm | Eu ppm | Gd ppm | Tb ppm |
|-----------|--------|--------|--------|--------|--------|--------|--------|--------|--------|--------|--------|--------|--------|--------|
| GAT-1 | 1 | 0.25 | 0.1 | 0.5 | 0.25 | 1.6 | 21.5 | 39.6 | 4.43 | 15.3 | 2.9 | 0.56 | 2.7 | 0.4 |
| GAT-2 | 1 | 0.25 | 0.1 | 1 | 0.25 | 1.8 | 21.7 | 40.3 | 4.36 | 14.9 | 3 | 0.58 | 2.5 | 0.4 |
| GAT-3 | 1 | 0.25 | 0.1 | 0.5 | 0.25 | 1.5 | 21.2 | 40.3 | 4.33 | 15 | 2.8 | 0.58 | 2.5 | 0.4 |
| SC | 1 | 1.2 | 0.1 | 0.5 | 24 | 0.6 | 0.2 | 0.5 | 0.05 | 0.2 | 0.05 | 0.025 | 0.05 | 0.05 |
| SA | 1 | 7.1 | 0.1 | 1 | 16.9 | 2 | 25.9 | 64.8 | 6.78 | 26.1 | 5.5 | 1.53 | 5.5 | 0.9 |
| SF-1 | 1 | 1.4 | 0.1 | 0.5 | 1 | 1.4 | 8.3 | 16.4 | 1.85 | 6.9 | 1.5 | 0.28 | 1.4 | 0.3 |
| SL-1 | 1 | 0.8 | 0.1 | 0.5 | 0.6 | 1.4 | 6.3 | 11.5 | 1.13 | 4.1 | 1 | 0.13 | 1 | 0.2 |
| SL-2 | 1 | 0.7 | 0.1 | 3 | 6.1 | 10.2 | 33.6 | 57.1 | 5.4 | 16.7 | 2.5 | 0.44 | 2 | 0.3 |
| CH-1 | 1 | 0.6 | 0.1 | 1 | 0.25 | 0.25 | 19.5 | 40.2 | 5.15 | 21.9 | 4.9 | 1.4 | 4.9 | 0.7 |
| SJ | 1 | 0.7 | 0.1 | 0.5 | 9.4 | 1.8 | 12.5 | 28.5 | 3.75 | 16.3 | 3.8 | 1.04 | 3.7 | 0.6 |
| MC-1 | 1 | 2.8 | 0.1 | 1 | 14.1 | 2.7 | 29.3 | 53 | 5.98 | 20.8 | 3.7 | 0.64 | 3 | 0.5 |
| MC-2 | 1 | 0.9 | 0.1 | 1 | 3.8 | 2.7 | 20 | 41.6 | 4.63 | 16.4 | 3.2 | 0.6 | 2.6 | 0.4 |
| MC-3 | 1 | 0.25 | 0.1 | 0.5 | 6.8 | 2.6 | 22.7 | 45 | 5.08 | 17.6 | 3.1 | 0.53 | 2.6 | 0.4 |
| SF-2 | 1 | 2.8 | 0.1 | 1 | 10.3 | 2.6 | 27.3 | 54.8 | 6.31 | 24.1 | 5 | 1.2 | 4.6 | 0.7 |
| SF-3 | 1 | 1 | 0.1 | 1 | 2.3 | 1.4 | 23.5 | 46.5 | 5.37 | 19.2 | 3.9 | 0.8 | 3.4 | 0.6 |

| Sample ID | Dy ppm | Ho ppm | Er ppm | Tm ppm | Yb ppm | Lu ppm | Hf ppm | Ta ppm | W ppm | Tl ppm | Pb ppm | Bi ppm | Th ppm | U ppm |
|-----------|--------|--------|--------|--------|--------|--------|--------|--------|-------|--------|--------|--------|--------|-------|
| GAT-1 | 2.6 | 0.5 | 1.5 | 0.22 | 1.5 | 0.25 | 2.5 | 0.7 | 0.5 | 0.5 | 11 | 0.2 | 5.2 | 2 |
| GAT-2 | 2.4 | 0.5 | 1.5 | 0.21 | 1.4 | 0.25 | 2.7 | 0.7 | 1 | 0.5 | 12 | 0.2 | 5.6 | 2 |
| GAT-3 | 2.4 | 0.5 | 1.4 | 0.22 | 1.5 | 0.23 | 3 | 0.7 | 0.5 | 0.4 | 12 | 0.2 | 5.5 | 1.9 |
| SC | 0.05 | 0.05 | 0.05 | 0.025 | 0.05 | 0.02 | 0.1 | 0.05 | 2 | 0.05 | 128 | 2.2 | 0.05 | 0.05 |
| SA | 5.5 | 1.3 | 4.2 | 0.7 | 4.8 | 0.77 | 4.5 | 0.9 | 2 | 2.2 | 273 | 0.2 | 1.6 | 0.6 |
| SF-1 | 1.8 | 0.4 | 1.4 | 0.25 | 1.9 | 0.33 | 4 | 0.7 | 1 | 1.8 | 11 | 0.2 | 4.1 | 2.2 |
| SL-1 | 2.1 | 0.6 | 2.2 | 0.38 | 3 | 0.47 | 4.7 | 1.1 | 0.5 | 0.5 | 17 | 0.2 | 20 | 6.3 |
| SL-2 | 2.1 | 0.4 | 1.3 | 0.23 | 1.5 | 0.25 | 3 | 1.5 | 2 | 2.1 | 20 | 0.2 | 17.9 | 2.5 |
| CH-1 | 4.6 | 0.9 | 2.7 | 0.38 | 2.4 | 0.38 | 3.4 | 0.3 | 0.5 | 0.4 | 9 | 0.2 | 3.5 | 1.3 |
| SJ | 3.3 | 0.7 | 1.9 | 0.27 | 1.7 | 0.26 | 3.3 | 0.3 | 3 | 2.2 | 686 | 0.2 | 1.3 | 0.6 |
| MC-1 | 2.8 | 0.6 | 1.7 | 0.26 | 1.8 | 0.28 | 2.8 | 0.8 | 4 | 2.1 | 16 | 0.2 | 10 | 2.4 |
| MC-2 | 2.6 | 0.5 | 1.4 | 0.21 | 1.4 | 0.22 | 2.6 | 0.6 | 6 | 1.9 | 14 | 0.2 | 4.8 | 2.6 |
| MC-3 | 2.3 | 0.4 | 1.3 | 0.19 | 1.3 | 0.2 | 2.2 | 0.5 | 2 | 0.9 | 23 | 0.2 | 5.4 | 2.2 |
| SF-2 | 4.3 | 0.8 | 2.5 | 0.37 | 2.4 | 0.4 | 3.8 | 0.6 | 21 | 3 | 78 | 0.2 | 4.7 | 2.6 |
| SF-3 | 3.4 | 0.7 | 2 | 0.31 | 2.1 | 0.32 | 3.1 | 0.6 | 1 | 1.9 | 563 | 0.2 | 4.3 | 2.1 |

Table 3. Summary statistics of untransformed geochemical assay data from the Independencia vein. MIN - Minimum; Q0.05 - 5% quartile; Q1 - 1st quartile; MED - median; Q3 - 3rd quartile; Q0.95 - 95% quartile; SD - standard deviation; MAD - median absolute deviation; IQR- interquartile range; MAX - maximum.

| | MIN | Q 0.05 | Q1 | MED | MEAN | Q3 | Q 0.95 | MAX | SD | MAD | IQR | CV % |
|-----------|------|--------|-------|------|-------|-------|--------|-------|-------|--------|-------|-------|
| Ag | 0.1 | 0.5 | 4.1 | 34.8 | 151.1 | 163 | 546.7 | 5270 | 393 | 50.11 | 117.8 | 260 |
| As | 2 | 5 | 18 | 33 | 64.33 | 71 | 207.5 | 942 | 92.89 | 29.65 | 39.29 | 144.4 |
| Au | 0.01 | 0.01 | 0.03 | 0.29 | 1.865 | 1.645 | 7.542 | 59.7 | 5.238 | 0.4151 | 1.197 | 280.9 |
| Ba | 3 | 10 | 40 | 120 | 286.6 | 350 | 1012 | 5350 | 458.2 | 133.4 | 229.8 | 159.9 |
| Fe | 0.28 | 0.848 | 1.845 | 2.81 | 3.001 | 4.035 | 5.673 | 9.14 | 1.517 | 1.586 | 1.623 | 50.55 |
| Mn | 76 | 523.8 | 1485 | 2788 | 3507 | 4662 | 9137 | 19600 | 2750 | 2242 | 2355 | 78.41 |
| Pb | 1.5 | 7.9 | 24 | 71 | 205 | 157 | 603.7 | 10000 | 650.4 | 78.58 | 98.59 | 317.2 |
| Sb | 2 | 2 | 3 | 4 | 7.889 | 8 | 23 | 303 | 16.43 | 2.965 | 3.706 | 208.2 |
| Sr | 4 | 13 | 33 | 57 | 79.05 | 90 | 221.2 | 897 | 85.11 | 40.03 | 42.25 | 107.7 |
| Zn | 13 | 52 | 110 | 231 | 440.3 | 436.5 | 1221 | 10000 | 926.8 | 206.1 | 242 | 210.5 |

Table 4 – A-D. Variation matrices of centered-log ratio (clr) transformed geochemical assay data from the Independencia deposit to investigate proportional relationship between variables (Reimann et al., 2008).

A.

Mineralized Structure

| | Ag | As | Au | Ba | Cu | Fe | Mn | Pb | Zn | Sb | clr.MAD |
|----|-------|-------|-------|-------|-------|-------|------|-------|------|------|---------|
| Ag | 0 | 7.61 | 0.68 | 6.84 | 5.02 | 7.67 | 3.86 | 3.07 | 3.99 | 5.73 | 1.87 |
| As | -0.38 | 0 | 7.85 | 2.07 | 1.53 | 0.94 | 1.36 | 2.49 | 1.61 | 1.16 | 1.05 |
| Au | 4.66 | 5.05 | 0 | 7.53 | 5.29 | 9.03 | 5.53 | 3.17 | 4.6 | 6.19 | 1.98 |
| Ba | -1.66 | -1.24 | -6.3 | 0 | 2.94 | 3.3 | 2.72 | 2.31 | 2.52 | 1.53 | 1.29 |
| Cu | -0.2 | 0.14 | -4.87 | 1.38 | 0 | 1.09 | 1.3 | 0.8 | 0.67 | 1.24 | 0.74 |
| Fe | 2.27 | 2.63 | -2.42 | 3.85 | 2.47 | 0 | 0.76 | 1.74 | 0.98 | 1.58 | 1.03 |
| Mn | -4.63 | -4.26 | -9.32 | -2.98 | -4.44 | -6.9 | 0 | 1.17 | 0.51 | 1.41 | 0.8 |
| Pb | -0.95 | -0.63 | -5.65 | 0.64 | -0.81 | -3.27 | 3.67 | 0 | 0.44 | 1.15 | 0.6 |
| Zn | -2.2 | -1.86 | -6.9 | -0.58 | -2.03 | -4.46 | 2.46 | -1.21 | 0 | 0.87 | 0.54 |
| Sb | 1.91 | 2.27 | -2.78 | 3.53 | 2.11 | -0.35 | 6.55 | 2.88 | 4.13 | 0 | 0.81 |

B.

Rhyolitic rocks

| | Ag | As | Au | Ba | Cu | Fe | Mn | Pb | Zn | Sb | clr.MAD |
|----|-------|-------|--------|-------|-------|-------|------|-------|------|------|---------|
| Ag | 0 | 1.85 | 1.06 | 1.85 | 1.06 | 1.51 | 2.78 | 1.68 | 1.44 | 1.06 | 0.93 |
| As | -2.81 | 0 | 1.45 | 0.99 | 1.85 | 0.86 | 1.58 | 1.06 | 1.41 | 1.06 | 0.93 |
| Au | 3.82 | 6.63 | 0 | 0.57 | 1.06 | 0.31 | 1.49 | 0.45 | 0.47 | 0 | 0.41 |
| Ba | -5.24 | -2.44 | -9.09 | 0 | 1.12 | 0.51 | 0.42 | 0.62 | 0.55 | 0.49 | 0.56 |
| Cu | -1.39 | 1.38 | -5.23 | 3.85 | 0 | 0.64 | 1.47 | 1.21 | 0.82 | 1.06 | 0.72 |
| Fe | -0.52 | 2.31 | -4.37 | 4.76 | 0.87 | 0 | 0.59 | 0.4 | 0.31 | 0.18 | 0.41 |
| Mn | -6.52 | -3.74 | -10.37 | -1.26 | -5.12 | -6.04 | 0 | 1.11 | 0.62 | 0.9 | 0.82 |
| Pb | -3.67 | -0.86 | -7.52 | 1.56 | -2.31 | -3.17 | 2.86 | 0 | 0.4 | 0.36 | 0.55 |
| Zn | -4.25 | -1.46 | -8.09 | 1.01 | -2.85 | -3.73 | 2.28 | -0.57 | 0 | 0.42 | 0.44 |
| Sb | -1.27 | 1.51 | -5.13 | 3.97 | 0.13 | -0.75 | 5.28 | 2.43 | 2.99 | 0 | 0.42 |

C.

Andesitic rocks

| | Ag | As | Au | Ba | Cu | Fe | Mn | Pb | Zn | Sb | clr.MAD |
|----|-------|-------|--------|-------|-------|-------|------|-------|------|------|---------|
| Ag | 0 | 1.68 | 1.58 | 3.21 | 3.95 | 3.58 | 2.11 | 2.52 | 2.66 | 4.22 | 1.45 |
| As | -2.99 | 0 | 1.06 | 1.58 | 2.07 | 1.47 | 1.05 | 1 | 1.08 | 0.95 | 0.82 |
| Au | 4.16 | 7.17 | 0 | 1.06 | 1.29 | 0.77 | 0.43 | 0.36 | 0.44 | 0.36 | 0.38 |
| Ba | -4.5 | -1.5 | -8.71 | 0 | 1.08 | 0.99 | 1.13 | 0.91 | 0.8 | 1.06 | 0.82 |
| Cu | -3.38 | -0.39 | -7.59 | 1.11 | 0 | 0.51 | 0.95 | 1.03 | 0.59 | 0.79 | 0.83 |
| Fe | -1.85 | 1.19 | -6.08 | 2.65 | 1.56 | 0 | 0.29 | 0.81 | 0.05 | 0.36 | 0.56 |
| Mn | -7.69 | -4.67 | -11.89 | -3.18 | -4.27 | -5.84 | 0 | 0.69 | 0.15 | 0.34 | 0.43 |
| Pb | -2.71 | 0.27 | -6.88 | 1.81 | 0.68 | -0.85 | 4.98 | 0 | 0.49 | 0.45 | 0.54 |
| Zn | -5.05 | -2.05 | -9.26 | -0.54 | -1.63 | -3.16 | 2.65 | -2.32 | 0 | 0.29 | 0.39 |
| Sb | -0.82 | 2.21 | -5 | 3.71 | 2.63 | 1.09 | 6.91 | 1.92 | 4.25 | 0 | 0.4 |

D.

Andesitic porphyry

| | Ag | As | Au | Ba | Cu | Fe | Mn | Pb | Zn | Sb | clr.MAD |
|----|-------|-------|--------|-------|-------|-------|------|-------|------|------|---------|
| Ag | 0 | 1.85 | 1.06 | 1.85 | 1.06 | 1.51 | 2.78 | 1.68 | 1.44 | 1.06 | 0.93 |
| As | -2.81 | 0 | 1.45 | 0.99 | 1.85 | 0.86 | 1.58 | 1.06 | 1.41 | 1.06 | 0.93 |
| Au | 3.82 | 6.63 | 0 | 0.57 | 1.06 | 0.31 | 1.49 | 0.45 | 0.47 | 0 | 0.41 |
| Ba | -5.24 | -2.44 | -9.09 | 0 | 1.12 | 0.51 | 0.42 | 0.62 | 0.55 | 0.49 | 0.56 |
| Cu | -1.39 | 1.38 | -5.23 | 3.85 | 0 | 0.64 | 1.47 | 1.21 | 0.82 | 1.06 | 0.72 |
| Fe | -0.52 | 2.31 | -4.37 | 4.76 | 0.87 | 0 | 0.59 | 0.4 | 0.31 | 0.18 | 0.41 |
| Mn | -6.52 | -3.74 | -10.37 | -1.26 | -5.12 | -6.04 | 0 | 1.11 | 0.62 | 0.9 | 0.82 |
| Pb | -3.67 | -0.86 | -7.52 | 1.56 | -2.31 | -3.17 | 2.86 | 0 | 0.4 | 0.36 | 0.55 |
| Zn | -4.25 | -1.46 | -8.09 | 1.01 | -2.85 | -3.73 | 2.28 | -0.57 | 0 | 0.42 | 0.44 |
| Sb | -1.27 | 1.51 | -5.13 | 3.97 | 0.13 | -0.75 | 5.28 | 2.43 | 2.99 | 0 | 0.42 |

Variables Log-ratio variance Log-ratio mean clr - median absolute deviation

Table 5. U-Pb age data and $\epsilon\text{Hf}(t)$ compositions summary table.

| Sample ID | Lithology | Location | Latitude | Longitude | LA-ICP-MS U-Pb zircon WM age (at 2σ) | LA-ICP-MS WM $\epsilon\text{Hf}(t)$ (at 1σ) |
|-------------|----------------------|------------------|-----------|-------------|--|---|
| GAT1 | rhyolitic ignimbrite | Guerra Al Tirano | 27.320526 | -108.368398 | 23.1 ± 0.4 Ma (MSWD = 0.41, n = 13) | 4.6 ± 1.0 (MSWD = 1.8, n = 10) |
| GAT2 | rhyolitic ignimbrite | Guerra Al Tirano | 27.320731 | -108.368365 | 23.4 ± 0.4 Ma (MSWD = 0.36, n = 19) | 3.3 ± 0.8 (MSWD = 2.0, n = 13) |
| GAT3 | rhyolitic ignimbrite | Guerra Al Tirano | 27.317528 | -108.371991 | 23.7 ± 0.4 Ma (MSWD = 0.39, n = 13) | 4.7 ± 0.9 (MSWD = 1.4, n = 10) |
| SF1 | rhyolitic ignimbrite | San Francisco | 27.411125 | -108.308102 | 28.1 ± 1.0 Ma (MSWD = 1.2, n = 13) | 1.6 ± 0.9 (MSWD = 1.7, n = 12) |
| GPN2 | rhyolitic ignimbrite | Guadalupe Norte | 27.657125 | -108.37606 | 23.7 ± 1.1 Ma (MSWD = 0.71, n = 4) | 0.6 ± 2.2 (MSWD = 2.2, n = 4) |

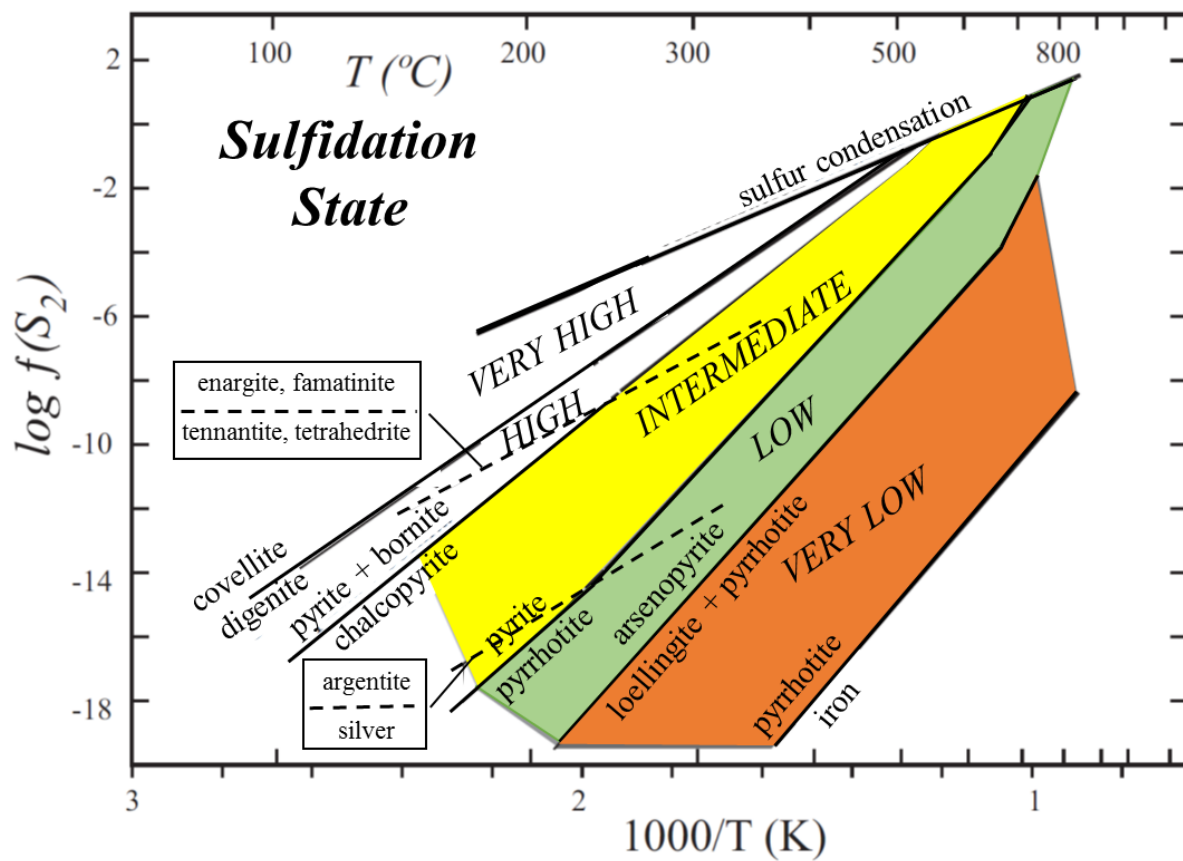


Figure 1. Correlation between temperature and sulfur fugacity for the sulfidation states related to hydrothermal fluids in the porphyry and epithermal domains, defined by stability fields of key minerals. Modified from Einaudi et al., (2003). Sulfur relationships are taken from Barton and Skinner (1979).

**Alkaline epithermal
(low and intermediate sulfidation)**

**Acidic epithermal
(high sulfidation)**

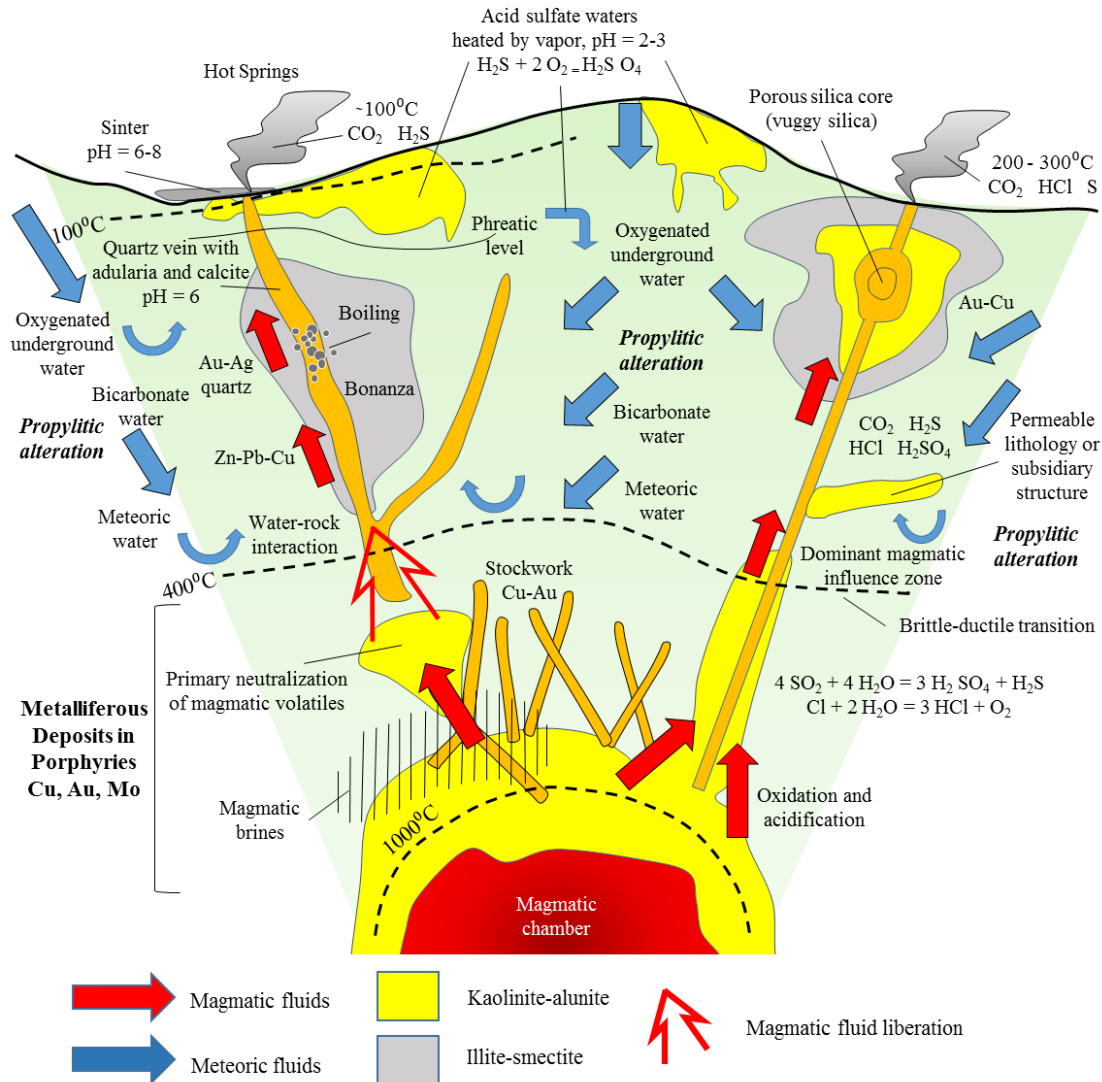
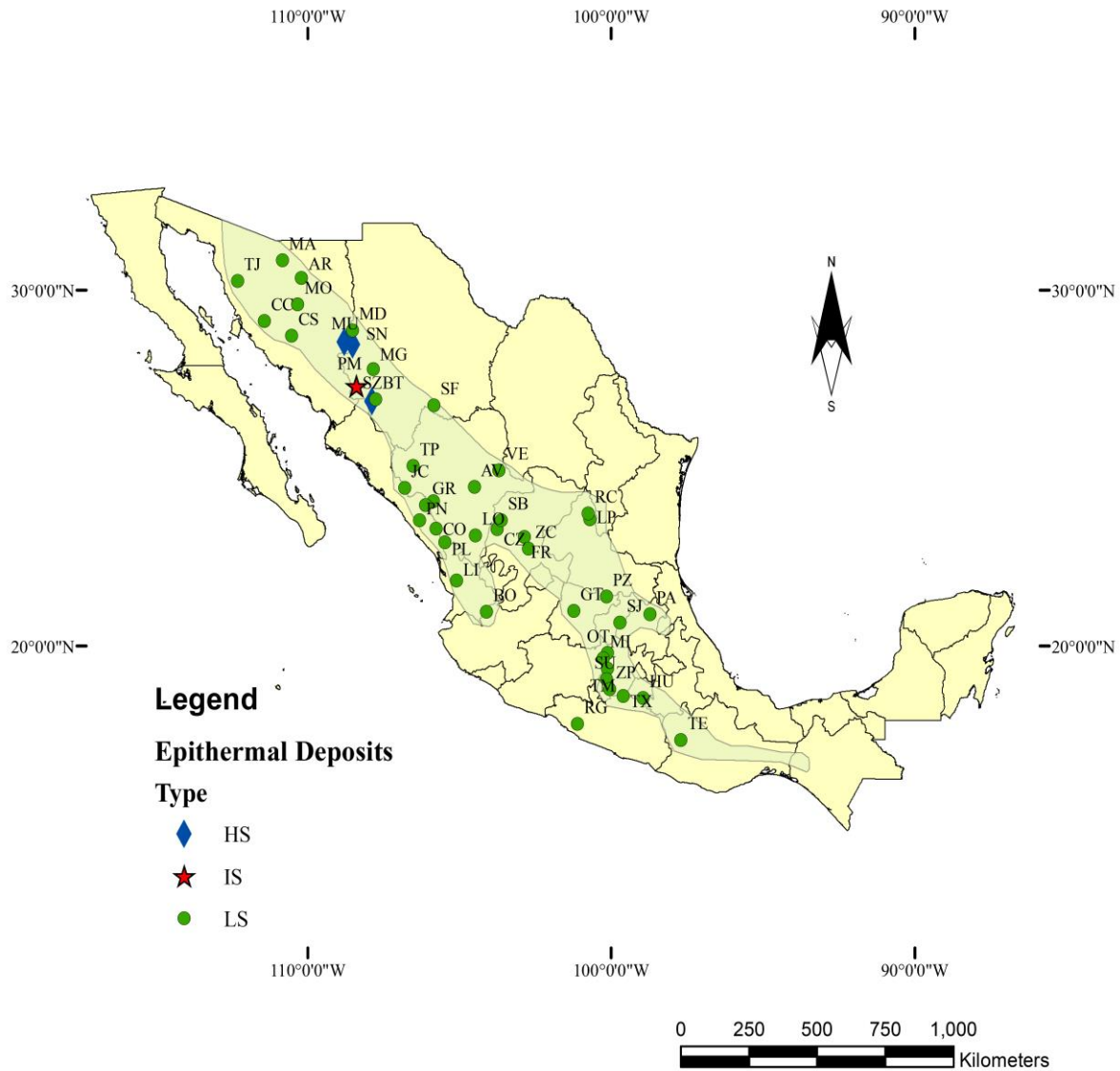


Figure 2. Comparative scheme (not to scale) of the structure, processes, alteration types, released volatiles, temperatures, pH, types of fluids and reactions involved in the formation of acidic (high sulfidation) and alkaline (low and intermediate sulfidation) epithermal deposits, and their relationship with magmatic rocks as the source of heat, fluids and chemical components for these deposits, from a magmatic chamber in a cooling process, leading to the formation of metallic deposits related to porphyries (Cu-Au-Mo), up to the epithermal environment (modified from Sillitoe, 1995a; based on data from Hedenquist and Lowenstern, 1994; Gammons y Williams-Jones, 1997; Corbett and Leach, 1998). The brittle-ductile transition boundary is placed at ~400°C and at 5-7 km depth (i.e. Fournier, 1991; Nielson et al., 1999).



Epithermal Deposits: BT – Batopilas, Chihuahua; SZ - El Sauzal, Chihuahua; MG – Maguarichic, Chihuahua; MD - Mineral de Dolores, Chihuahua; PM – Palmarejo, Chihuahua; SF - San Francisco del Oro, Chihuahua; SN - Santo Niño, Chihuahua; AV – Avino, Durango; LO - Lluvia de Oro, Durango; TY – Tayoltita, Durango; TP – Topia, Durango; VE – Velardeña, Durango; OT - El Oro, Estado de Mexico; MI - Miahuatla e Ixtapan de Oro, Estado de Mexico; SU - Sultepec y Amatepec, Estado de Mexico; TM – Temascaltepec, Estado de Mexico; ZP – Zacualpan, Estado de Mexico; GT – Guanajuato, Guanajuato; PZ – Pozos, Guanajuato; RG - Real de Guadalupe, Guerrero; TX – Taxco, Guerrero; PA - Pachuca Real del Monte, Hidalgo; BO – Bolaños, Jalisco; HU – Huautla, Morelos; LI - El Indio, Nayarit; TE – Tejomulco, Oaxaca; SJ - San Joaquin, Queretaro; LP - La Paz, San Luis Potosi; RC - Real de Catorce, San Luis Potosi; CO – Copala, Sinaloa; GR - Guadalupe de los Reyes, Sinaloa; PN - Panuco, Sinaloa; PL – Plomosas, Sinaloa; JC - San Jose del Cobre, Sinaloa; AR – Arizpe, Sonora; CC - Cerro Colorado, Sonora; CS - La Colorada, Sonora; MA – Magallanes, Sonora; MO – Moctezuma, Sonora; MU – Mulatos, Sonora; TJ – Tajitos, Sonora; FR – Fresnillo, Zacatecas; CZ - La Colorada, Zacatecas; SB – Sombrerete, Zacatecas; ZC – Zacatecas, Zacatecas.

Figure 3. Distribution map of epithermal-type deposits in Mexico in a NW trending metallogenic belt (modified from Camprubi and Albinson, 2007).



Figure 4. Location map of study area in the Palmarejo District, Chihuahua, Mexico in relation to major cities in the state of Chihuahua and highway networks (INEGI, 2005).

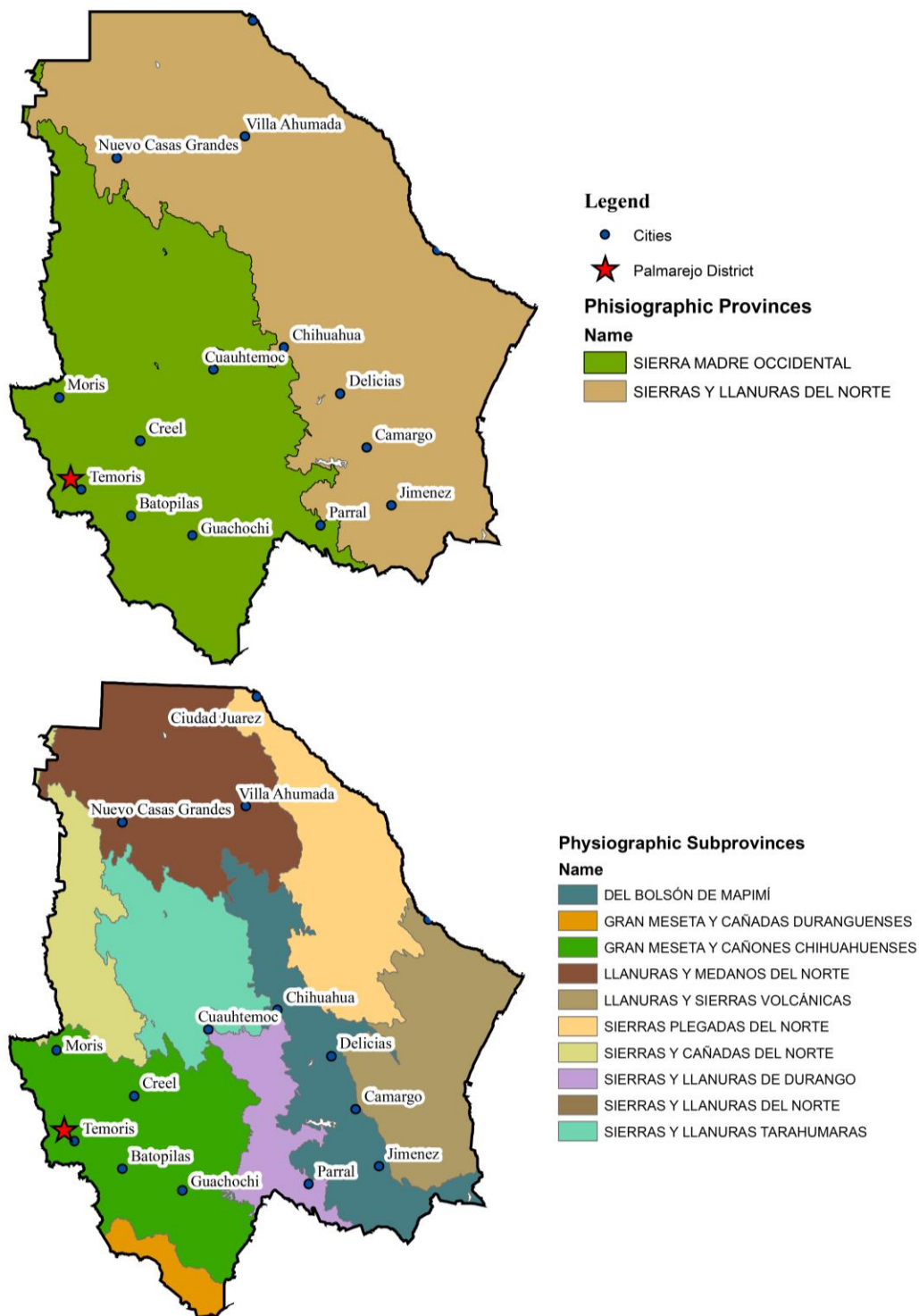


Figure 5. Physiographic provinces map of the state of Chihuahua in relation to the Palmarejo district location (INEGI, 2005).

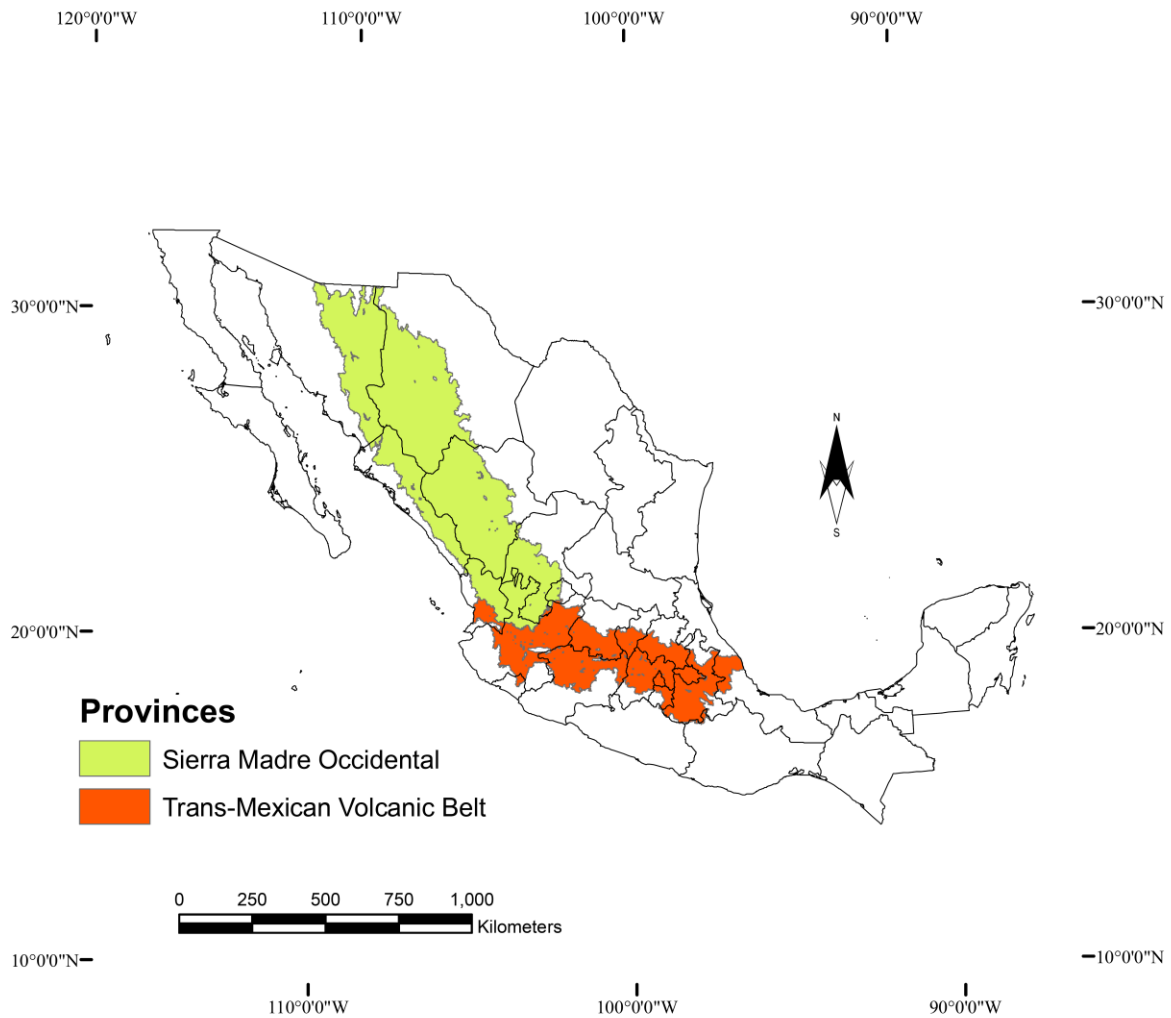


Figure 6. Geographic extent map of the Sierra Madre Occidental in northwestern Mexico and its southern intersection with the Trans-Mexican Volcanic Belt (modified from McDowell and Keizer, 1977; Bryan et al., 2008).

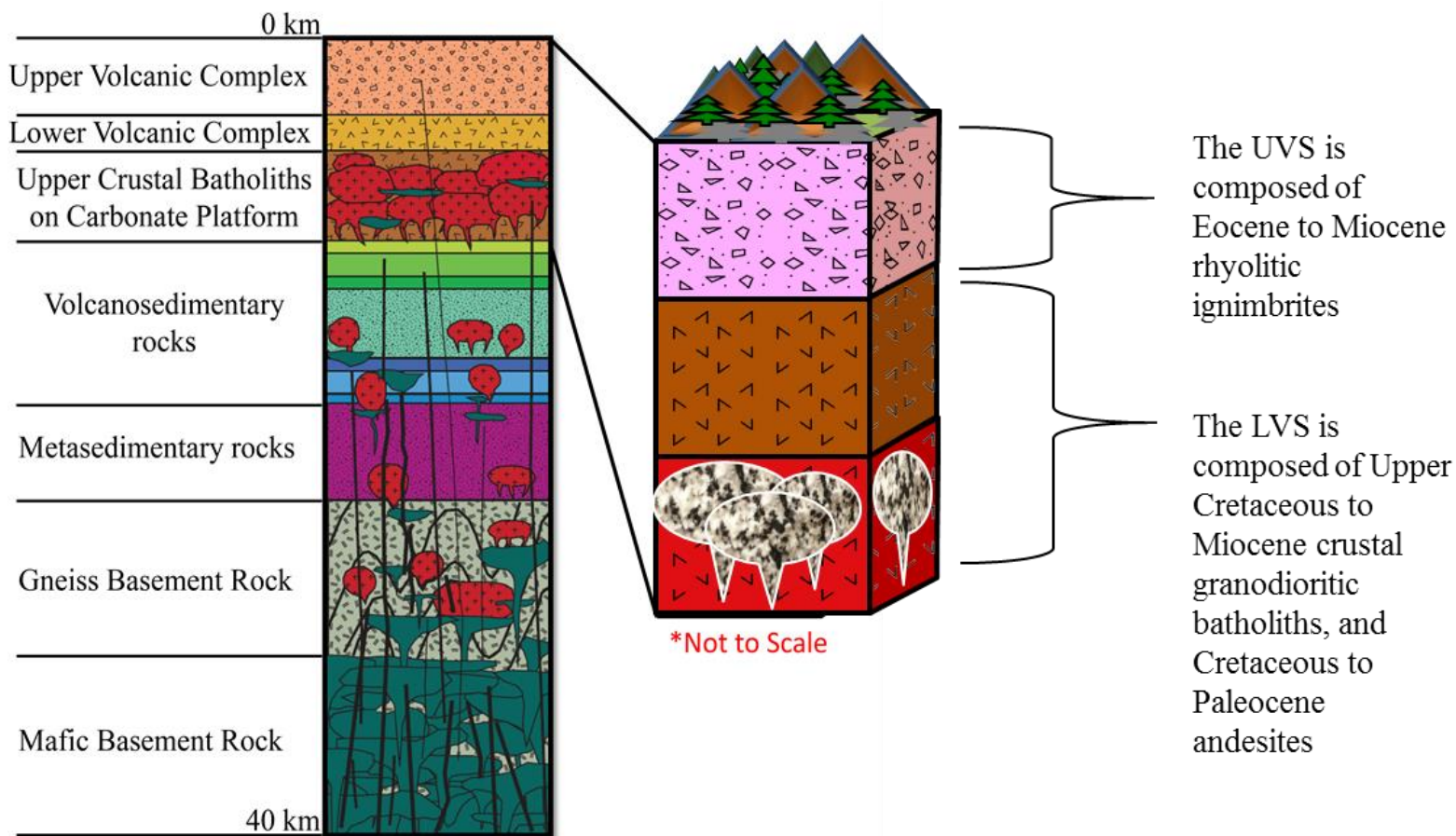


Figure 7. Regional stratigraphic profile of the northern SMO and rock constituents of the UVS (Upper Volcanic Supergroup) and LVS (Lower Volcanic Supergroup) (modified from Ferrari et al. 2007). The UVS and LVS are terms introduced by McDowell and Keizer (1977).

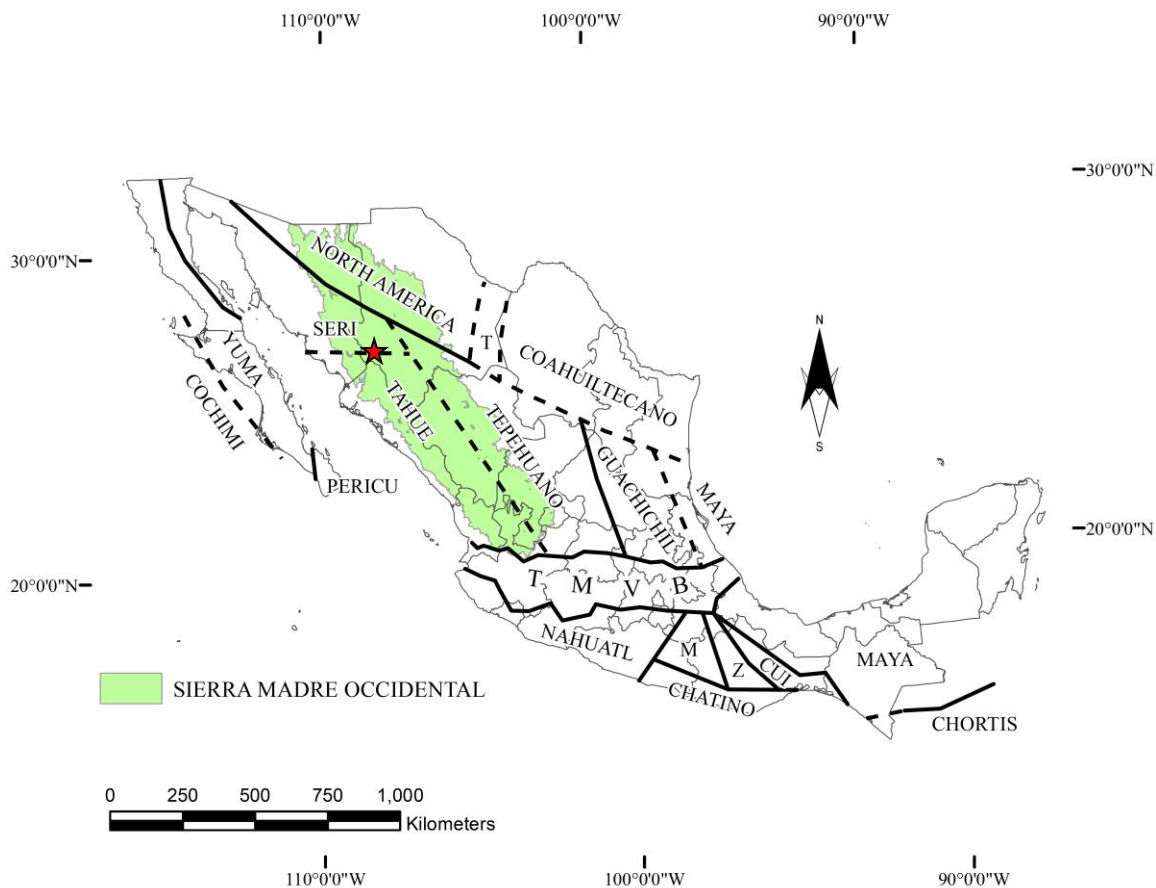


Figure 8. Tectono-stratigraphic terrane map of Mexico in relation to the Sierra Madre Occidental (modified from Sedlock et al., 1993). Red star – Palmarejo district. *CUI* – Cuicateco Terrane; *M* – Mixteco Terrane; *TMVB* – Trans-Mexican Volcanic Belt; *Z* – Zapoteco Terrane.

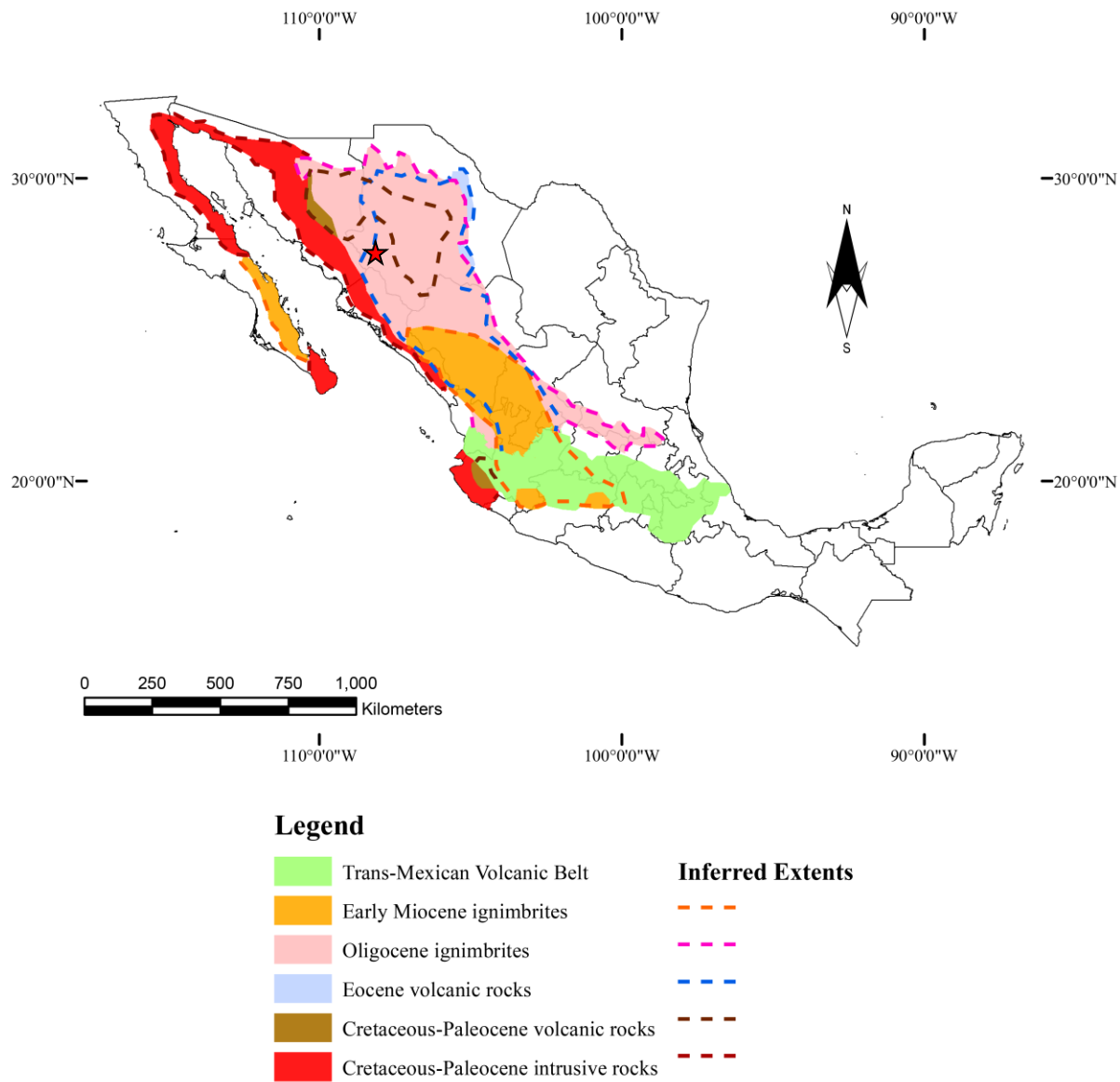


Figure 9. Geographic extent map of the Tertiary ignimbritic pulses in northwestern Mexico underlain by Cretaceous volcanic and plutonic rocks (modified from Ferrari et al., 2007). Red star –Palmarejo district.

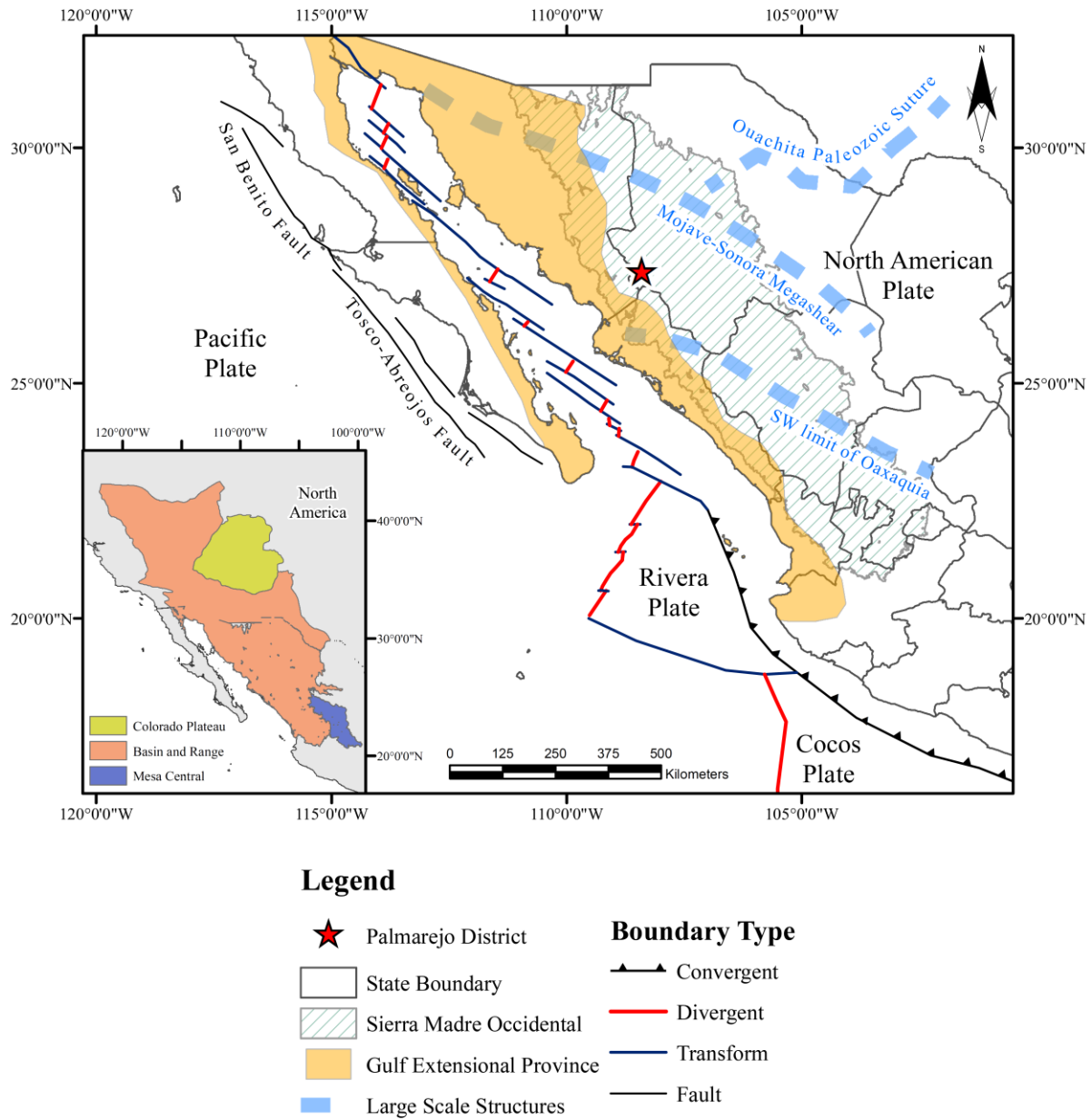


Figure 10. Regional tectonic setting of northwestern Mexico showing the transtensional plate boundary of the Gulf of California along with the geographical extent of the Basin and Range and Gulf extensional provinces (modified from Parsons, 1995; Ferrari et al., 2007; Alvarez et al., 2009).

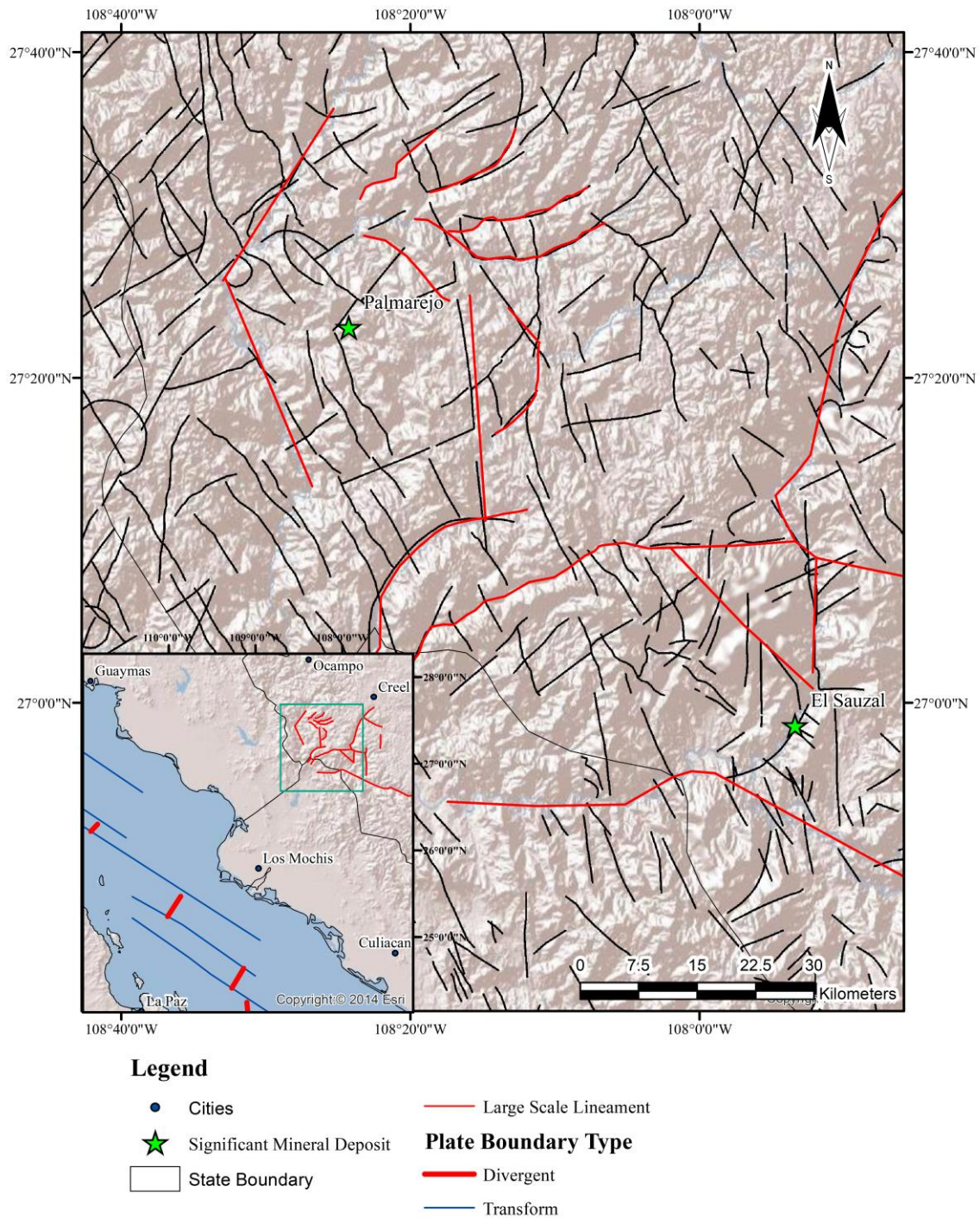
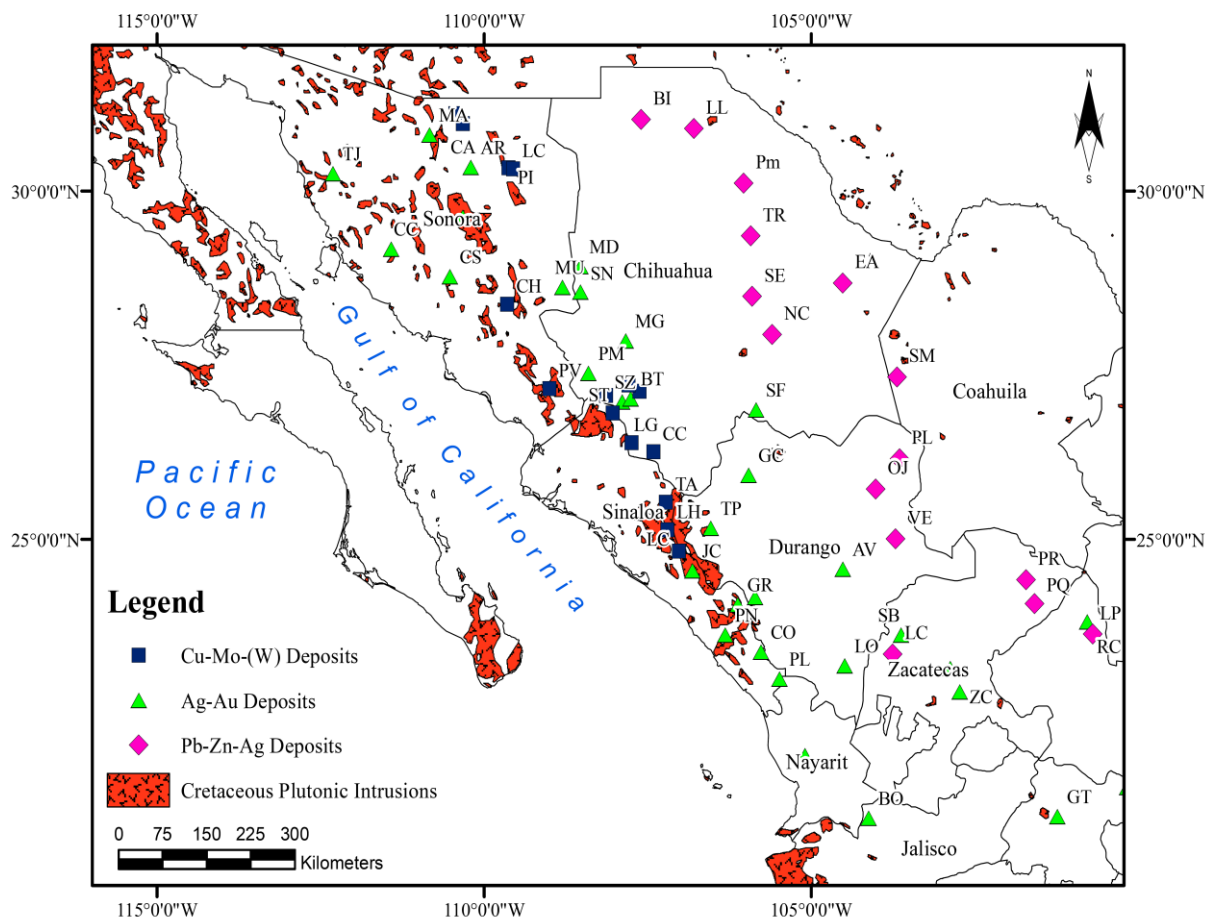
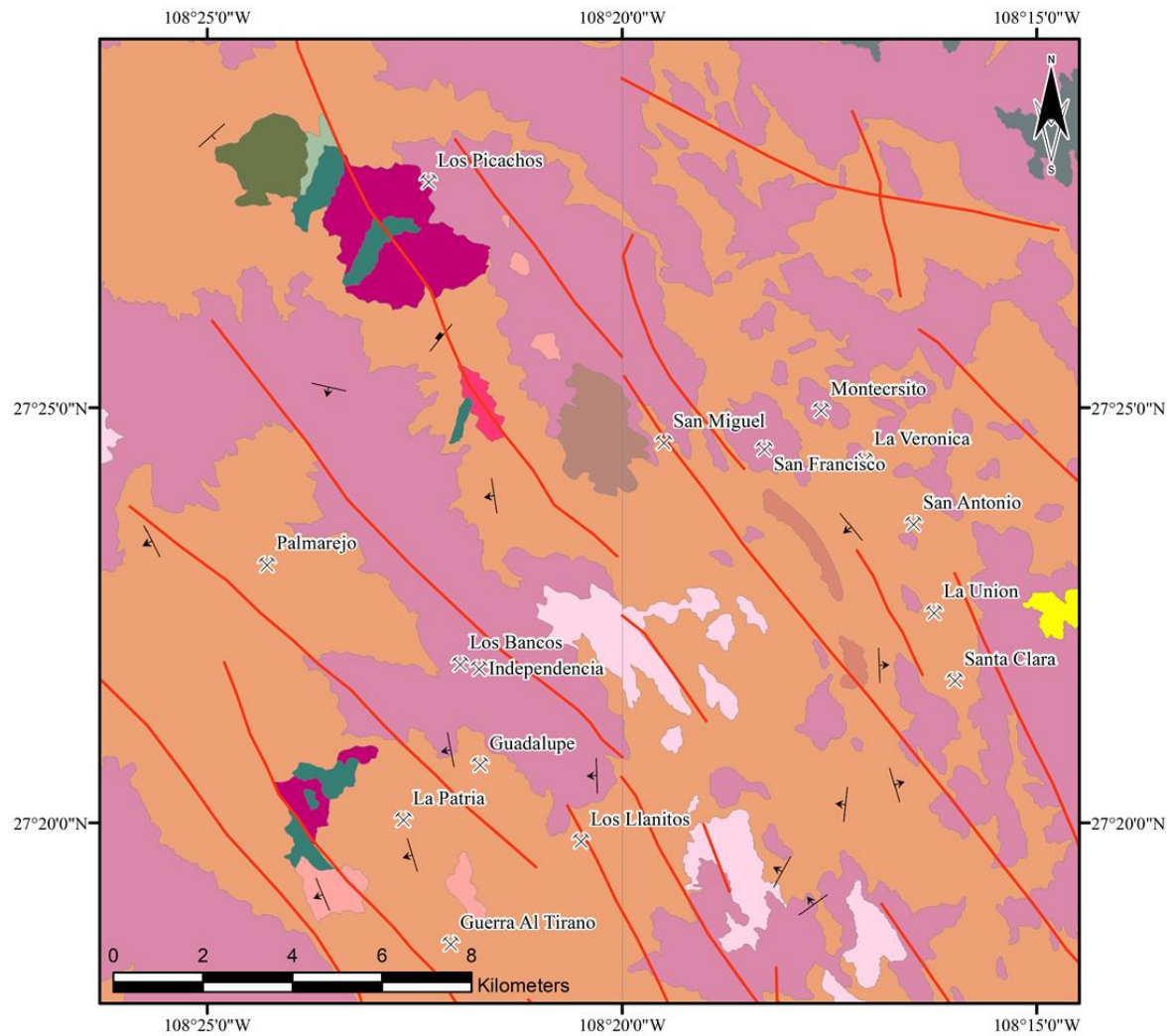


Figure 11. Structural trend map of the Chihuahua-Sonora-Sinaloa border region showing structural lineaments interpreted as the boundaries of pull-apart basins with the Palmarejo and Sauzal mines as reference (modified from the Servicio Geológico Mexicano, 2015).



Porphyry Deposits: CC - Cerro Colorado, Chihuahua; LG - La Guadalupeana, Chihuahua; LB - La Bufa, Chihuahua; BH - Bahuerachi, Chihuahua; St - Satevo, Chihuahua; LH - Las Higueras, Sinaloa; LC - Los Chicharrones, Sinaloa; ST - Santo Tomas, Sinaloa; TA - Tameapa, Sinaloa; MP - Milpillas, Sonora; CA - Cananea, Sonora; PI - Pilaes, Sonora; LC - La Caridad, Sonora; PV - Piedras Verdes, Sonora; CH - Cuatro Hermanos, Sonora. **Epithermal Deposits:** BT - Batopilas, Chihuahua; SZ - El Sauzal, Chihuahua; MG - Maguarichic, Chihuahua; MD - Mineral de Dolores, Chihuahua; PM - Palmarejo, Chihuahua; SF - San Francisco del Oro, Chihuahua; SN - Santo Niño, Chihuahua; AV - Avino, Durango; GC - Guanacevi, Durango; LO - Lluvia de Oro, Durango; TY - Tayoltita, Durango; TP - Topia, Durango; OT - El Oro, Estado de Mexico; MI - Miahuatla e Ixtapan de Oro, Estado de Mexico; SU - Sultepec y Amatepec, Estado de Mexico; TM - Temascaltepec, Estado de Mexico; ZP - Zacualpan, Estado de Mexico; GT - Guanajuato, Guanajuato; PZ - Pozos, Guanajuato; RG - Real de Guadalupe, Guerrero; TX - Taxco, Guerrero; PA - Pachuca Real del Monte, Hidalgo; BO - Bolaños, Jalisco; HU - Huautla, Morelos; LI - El Indio, Nayarit; TE - Tejomulco, Oaxaca; SJ - San Joaquin, Queretaro; RC - Real de Catorce, San Luis Potosi; CO - Copala, Sinaloa; GR - Guadalupe de los Reyes, Sinaloa; PN - Panuco, Sinaloa; PL - Plomos, Sinaloa; JC - San Jose del Cobre, Sinaloa; AR - Arizpe, Sonora; CC - Cerro Colorado, Sonora; CS - La Colorada, Sonora; MA - Magallanes, Sonora; MO - Moctezuma, Sonora; MU - Mulatos, Sonora; TJ - Tajitos, Sonora; FR - Fresnillo, Zacatecas; SB - Sombrerete, Zacatecas; ZC - Zacatecas, Zacatecas. **Replacement-Manto Deposits:** BI - Bismark, Chihuahua; LL - Los Lamentos, Chihuahua; Pm - Plomos, Chihuahua; TR - Terrazas, Chihuahua; SE - Santa Eulalia, Chihuahua.

Figure 12. Distribution map of metallic mineralization related to porphyry, epithermal and carbonate replacement deposits in Mexico in relationship to the Cretaceous plutonic intrusions associated to the Laramidic magmatic arc (modified from Clark and Fitch, 2009; Ortega-Gutierrez et al., 2014)



Legend

| | | |
|--|--|--|
| Miocene Sandy - Rhyolitic Tuff (TmS-RT) | Oligocene Rhyolite (ToR) | Late Cretaceous Granite - Granodiorite (KlGr-Gd) |
| Miocene Sandy - Basalt (TmS-B) | Oligocene Rhyolitic Tuff - Rhyolite (ToRT-R) | Early Cretaceous Sandy Limestone (KeS-Lm) |
| Miocene Basalt (TmB) | Oligocene Rhyodacite - Dacite (ToRd-Da) | Jurassic Sandy Shale (JrS-Sh) |
| Miocene Rhyolite - Rhyolitic Tuff (TmR-RT) | Paleocene-Eocene - Sandy Andesite (TpaeS-A) | Normal Fault |
| Oligocene Rhyolitic Porphyry (ToRP) | Late Cretaceous Sandy Conglomerate (KlS-Cgp) | Strike and Dip |
| | | Deposit |

Figure 13. Palmarejo District regional geologic map (modified from the Servicio Geológico Mexicano, 2015).

Stratigraphy

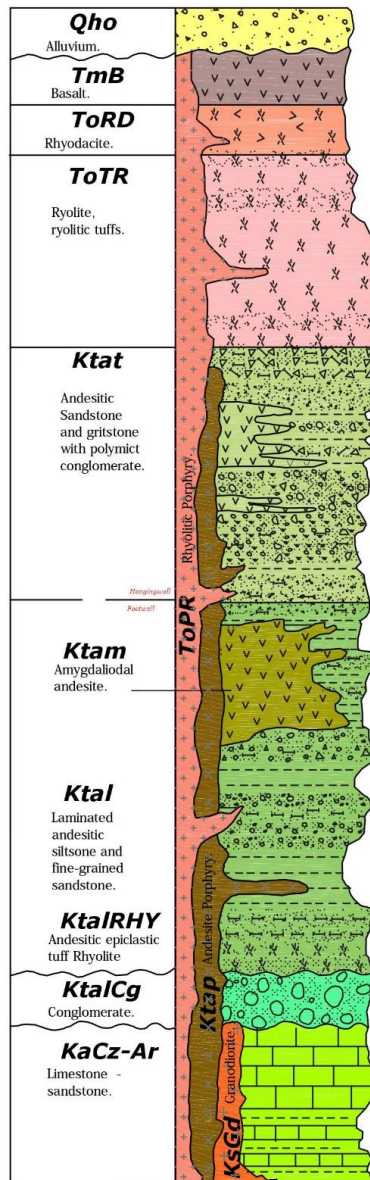


Figure 14. Stratigraphic section of the Palmarejo district lithologic units (Kerr et al., 2015).

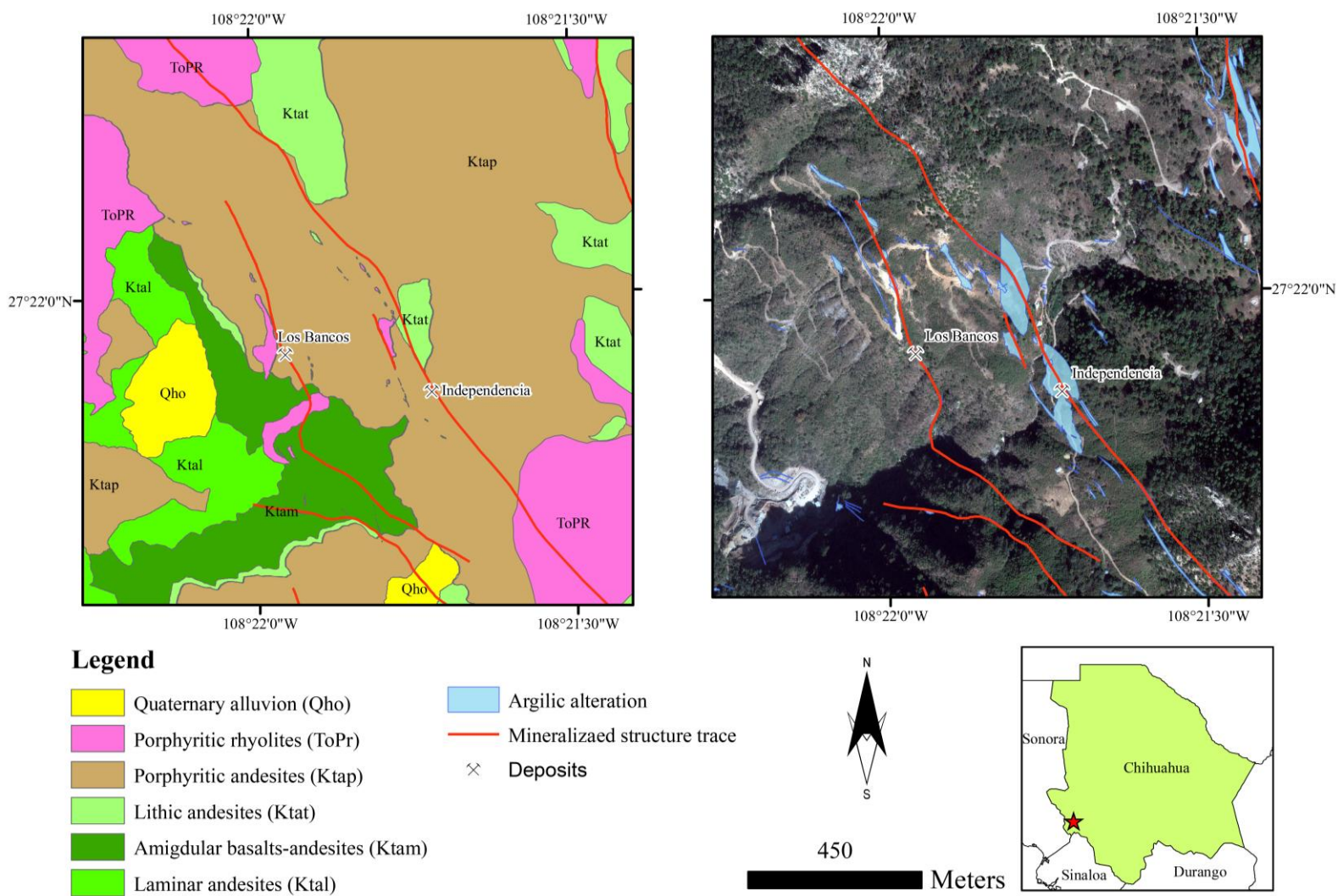


Figure 15. Geologic and alteration map of the Los Bancos – Independencia epithermal vein deposits.

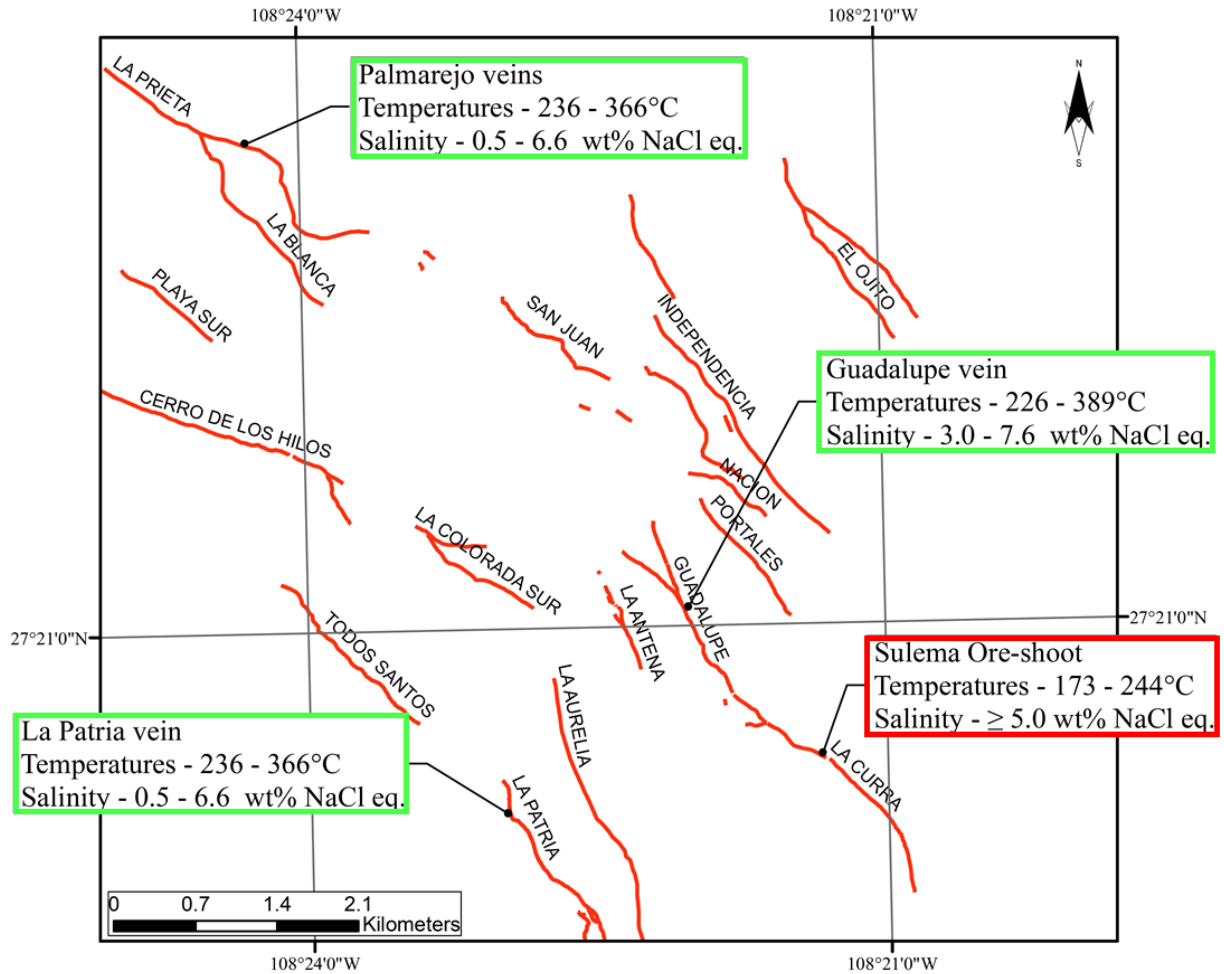


Figure 16. Regional fluid inclusion map of the Palmarejo district showing homogenization temperatures and salinities of significant quartz-veins (Miller, 1988 (red box); Galvan-Gutierrez, 2012 (green boxes)).

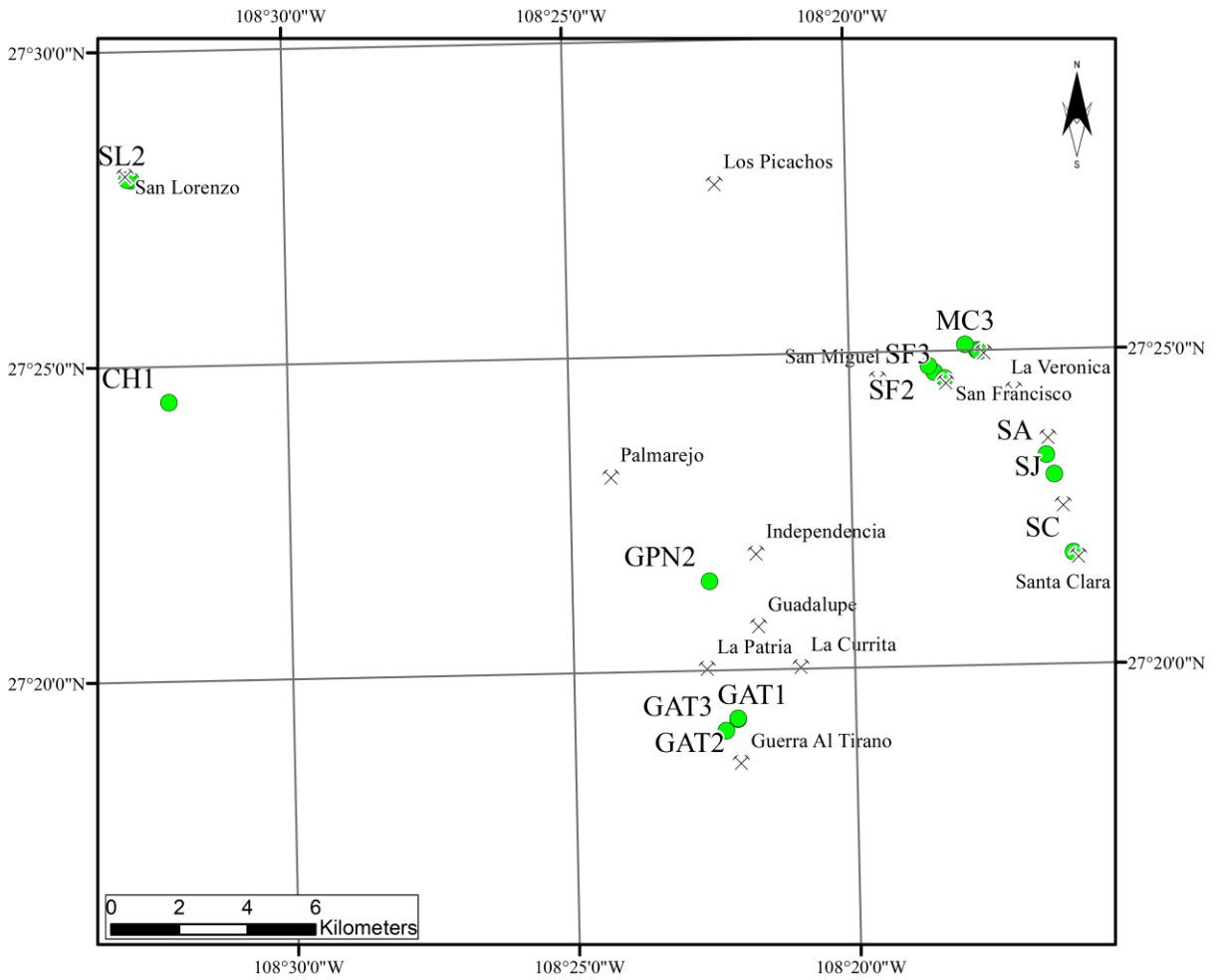


Figure 17. Location map of studied samples from the Palmarejo district.

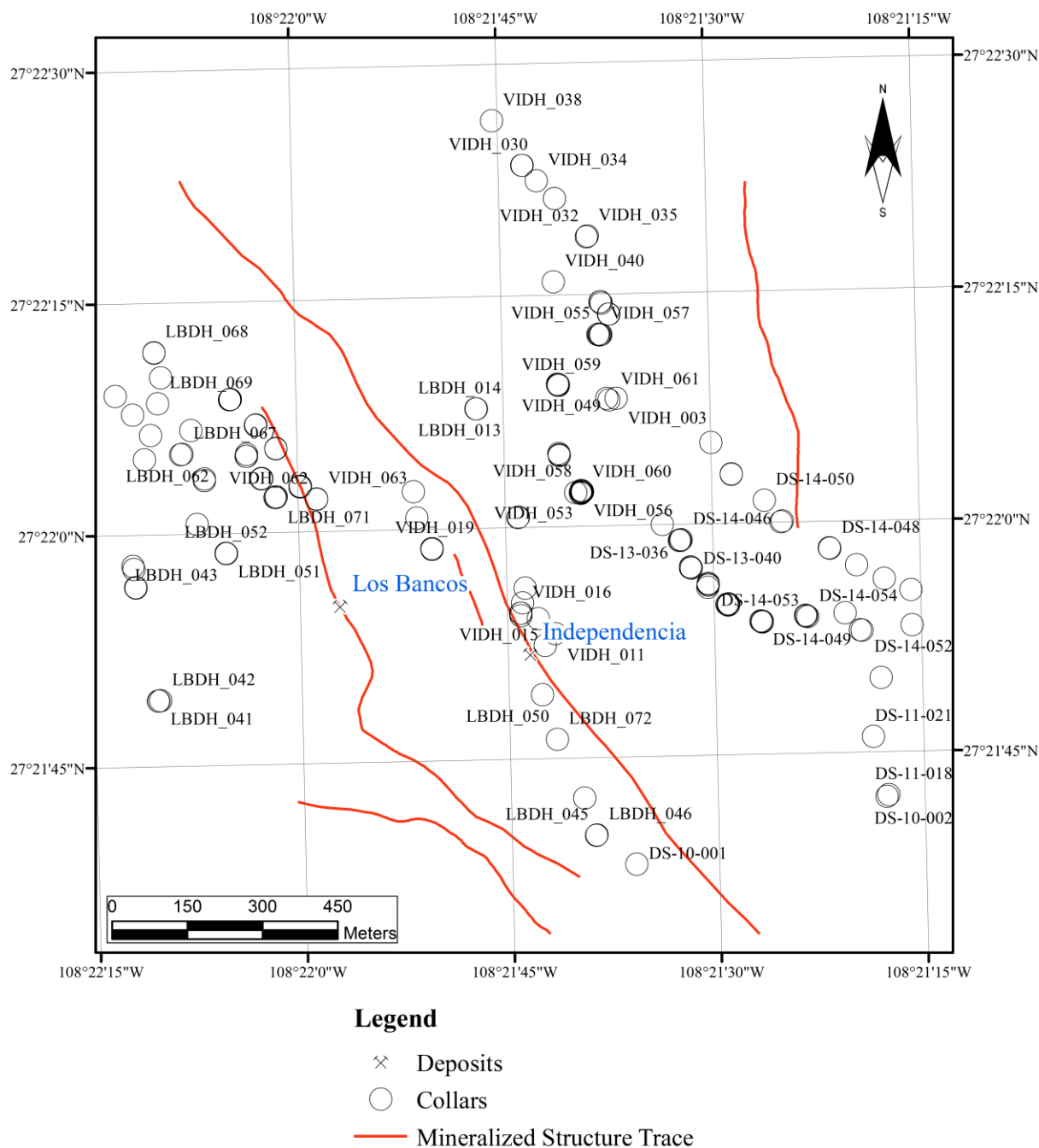


Figure 18. Location map of drill-holes provided by Coeur Mining Inc. from the Los Bancos – Independencia deposits.

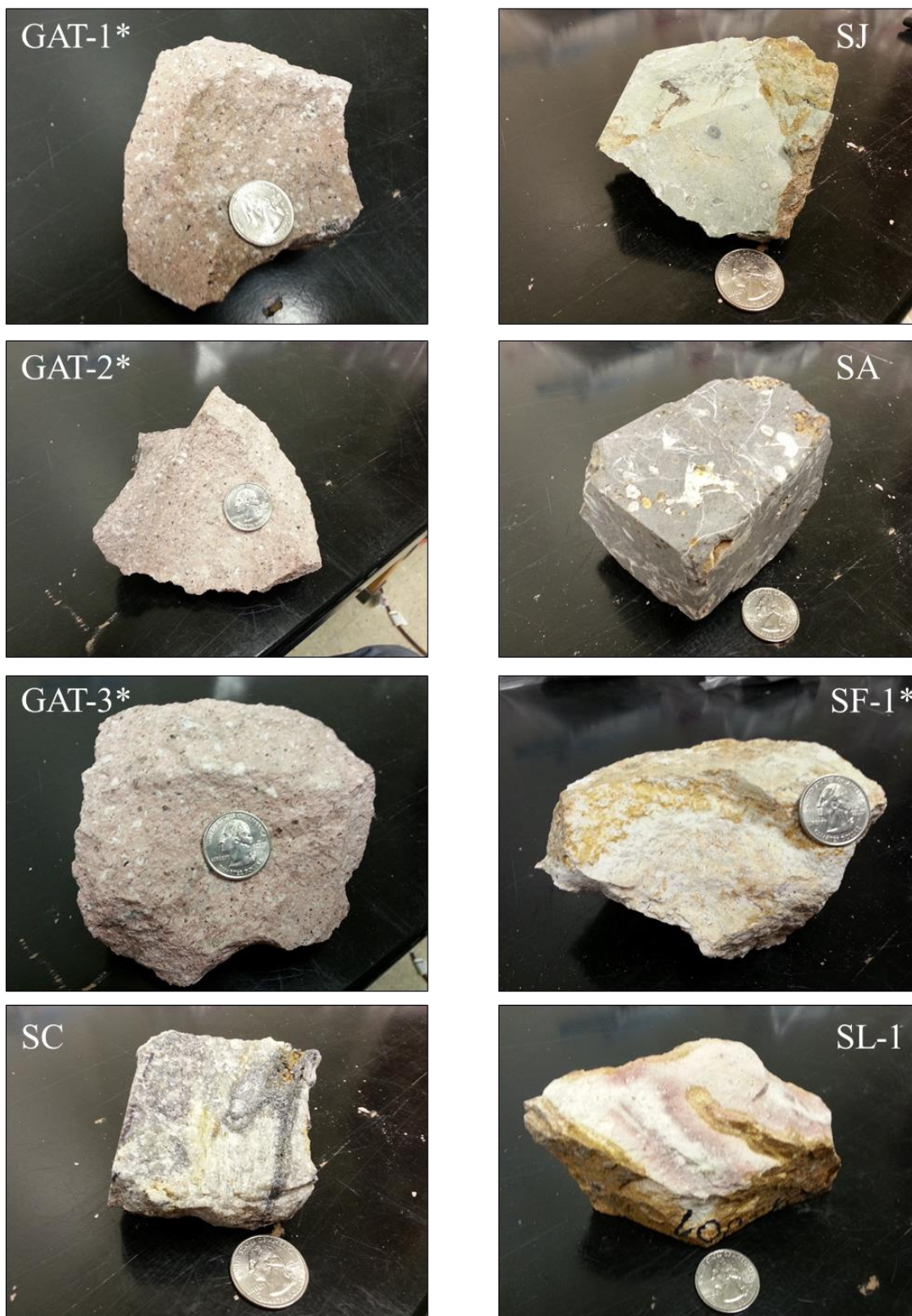


Figure 19. Photos of studied samples with sample identification as reference.*Geochronology and isotopic analyses.

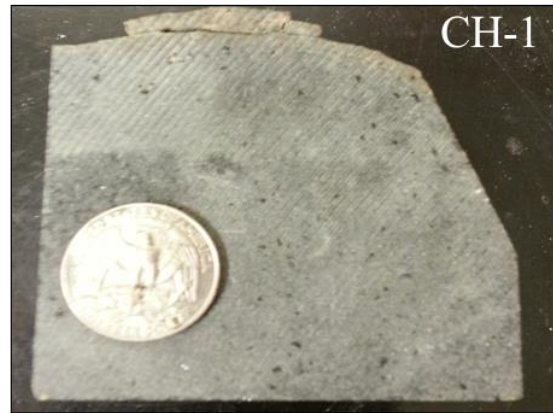


Figure 19 cont. Photos of studied samples with sample identification as reference.
 *Geochronology and isotopic analyses.

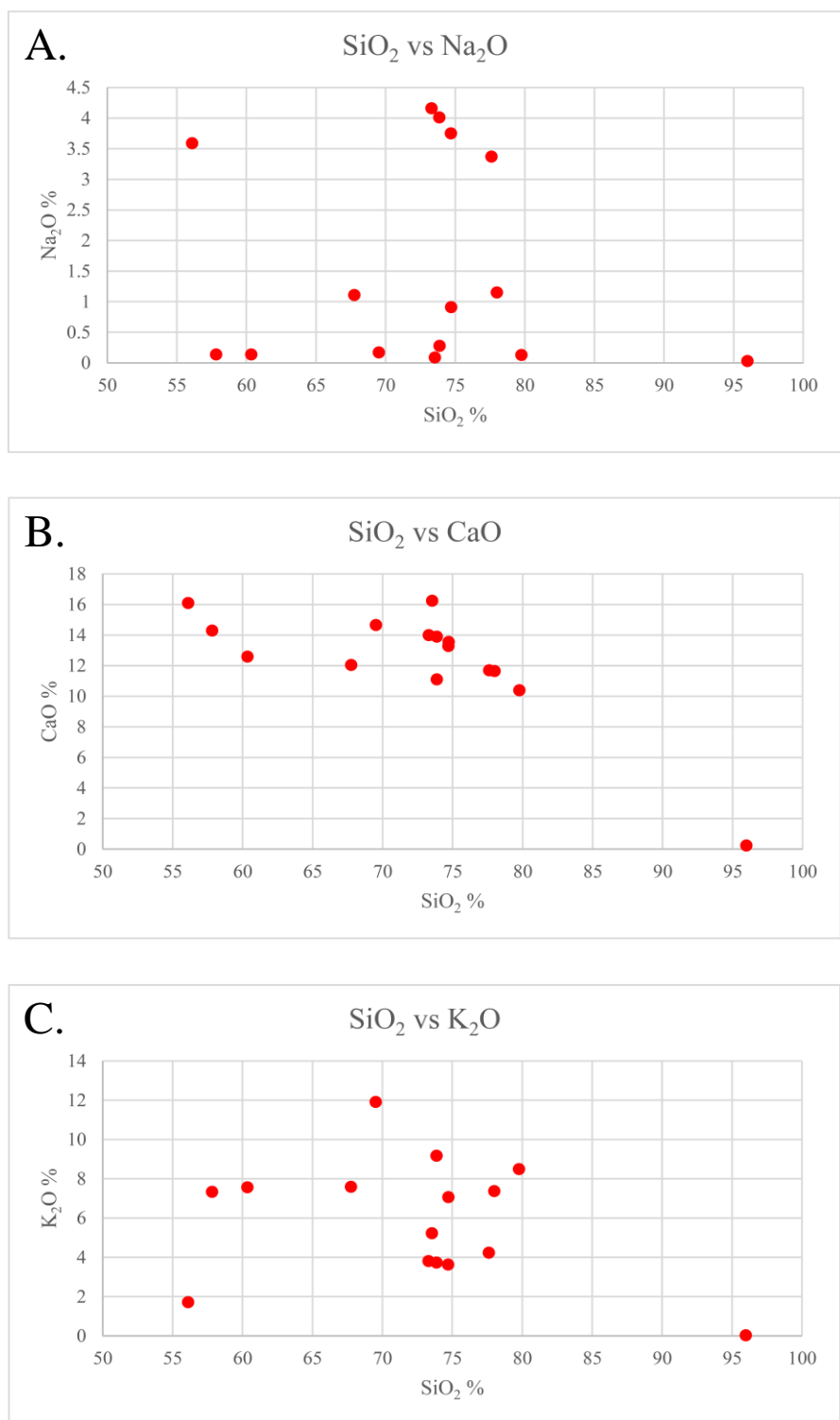


Figure 20 – A-C. Major element variation diagrams

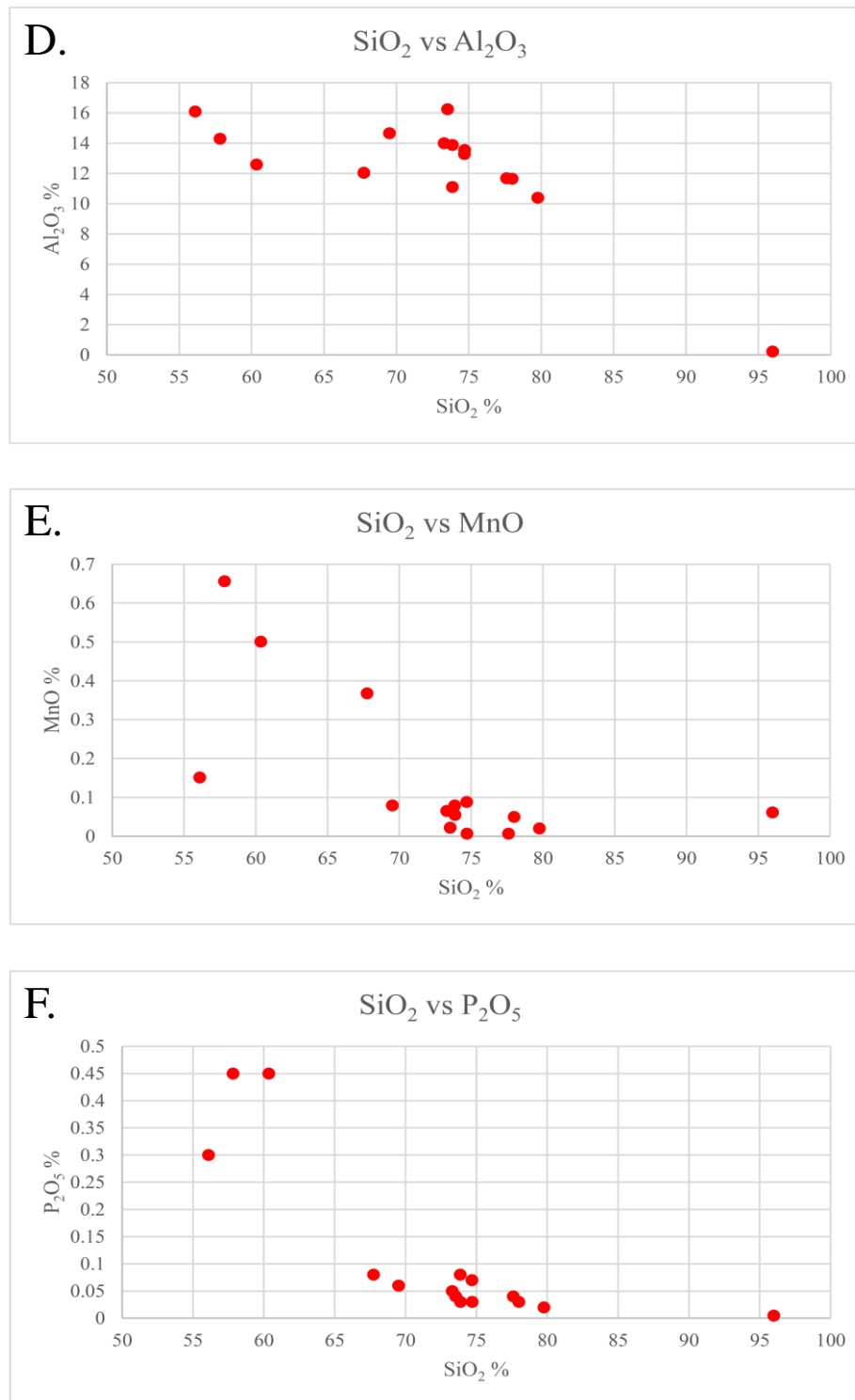


Figure 20 – D-F. Major element variation diagrams.

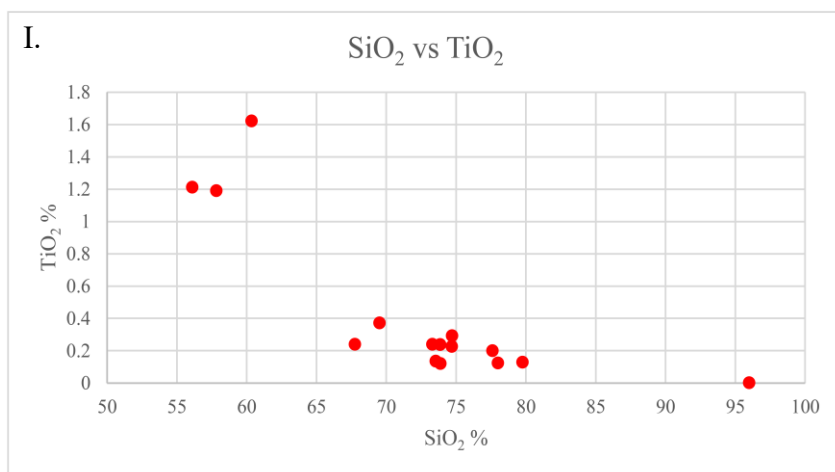
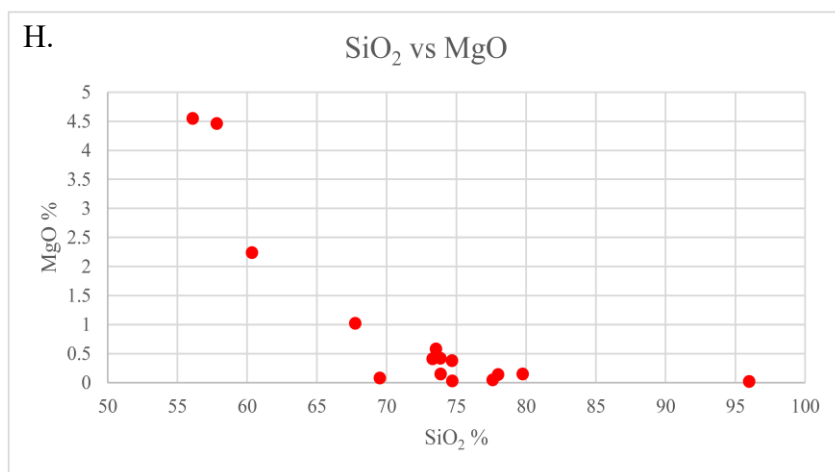
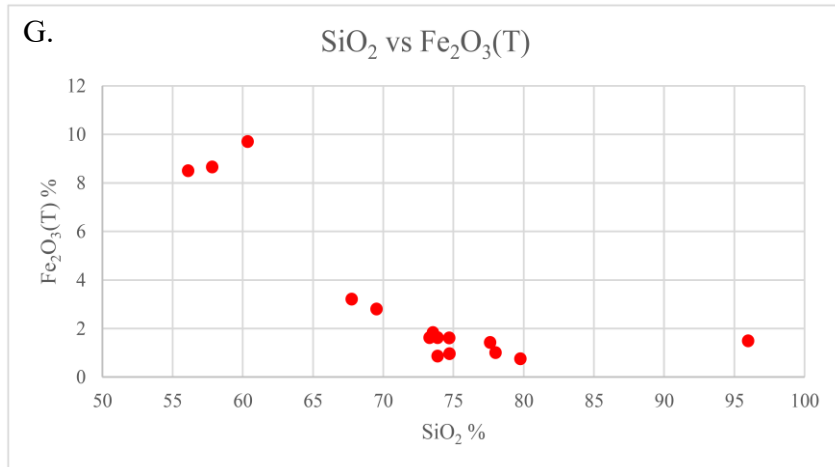


Figure 20 – G-I. Major element variation diagrams.

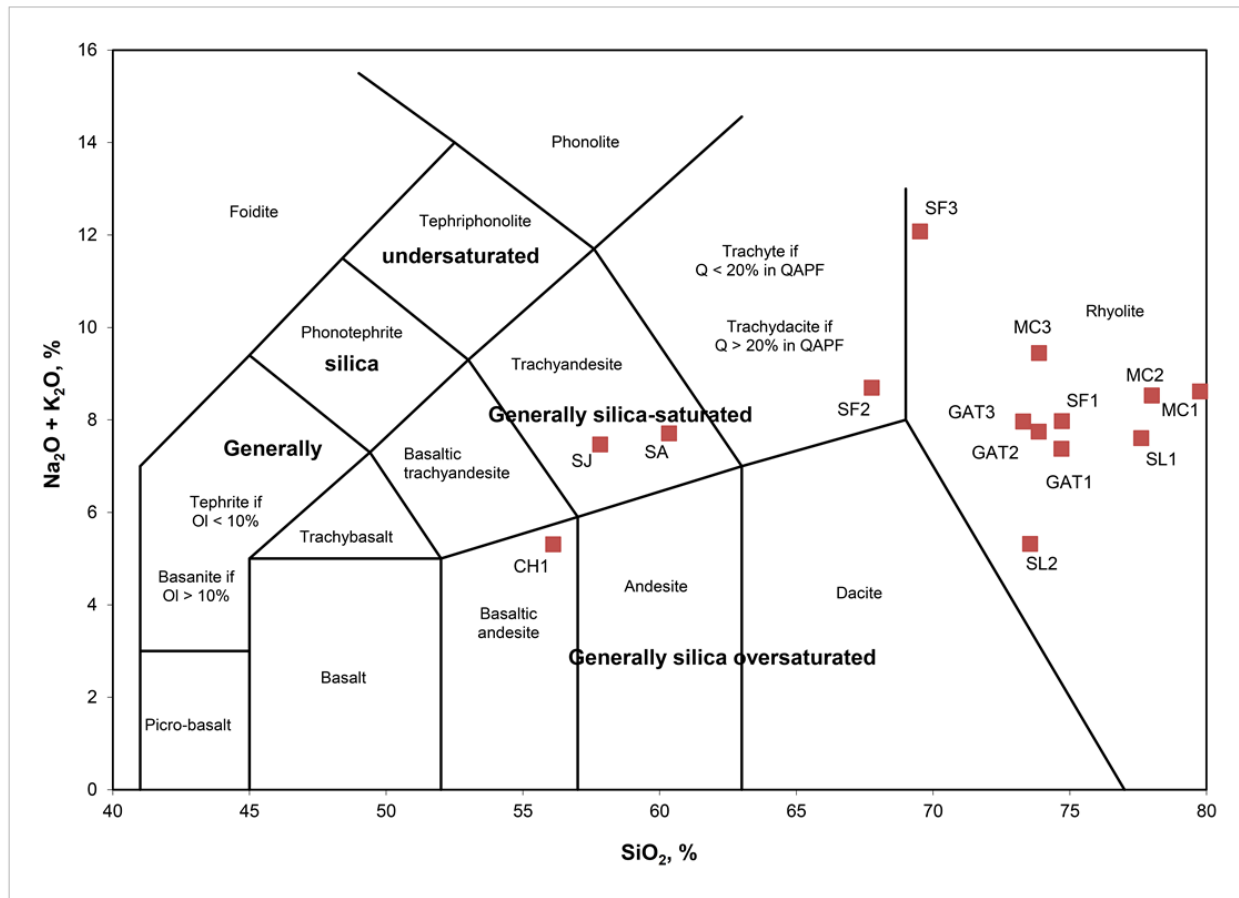


Figure 21. Total Alkali-Silica diagram showing volcanic rock classifications of samples from the Palmarejo district (LeBas et al., 1986).

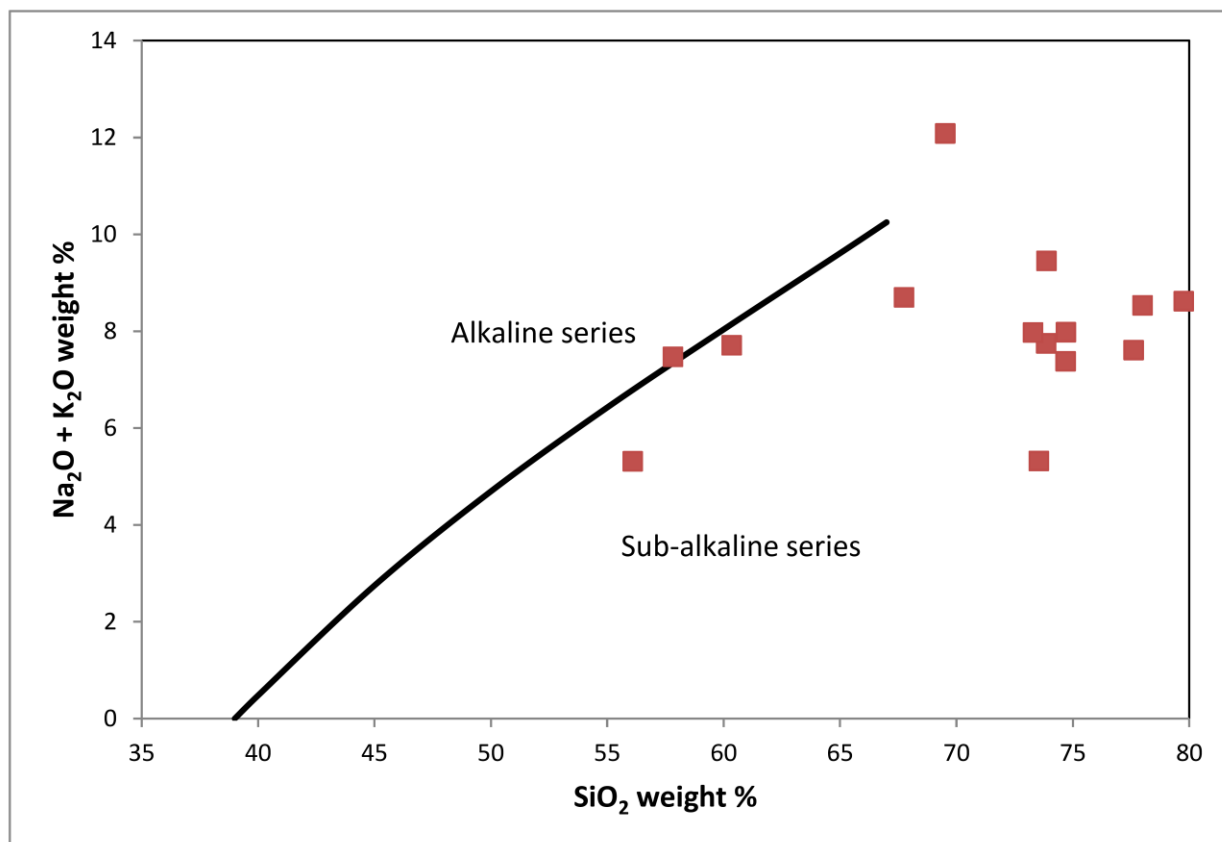


Figure 22. Alkaline and sub-alkaline magma series classification diagram based on major element concentrations in samples from the Palmarejo district (Irvine and Barragar, 1971).

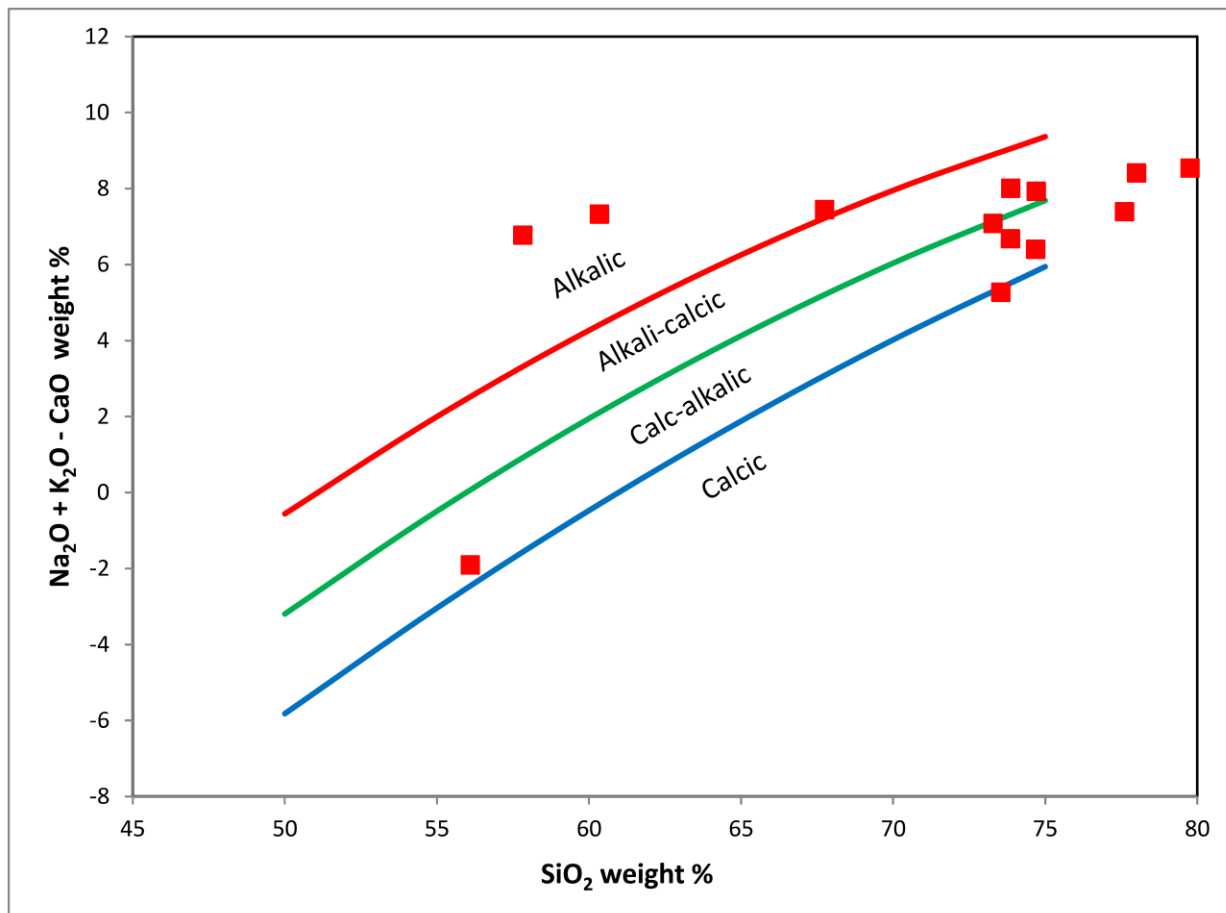


Figure 23. Feldspathic igneous rock classification diagram based on major element concentrations in samples from the Palmarejo district (Frost and Frost, 2008).

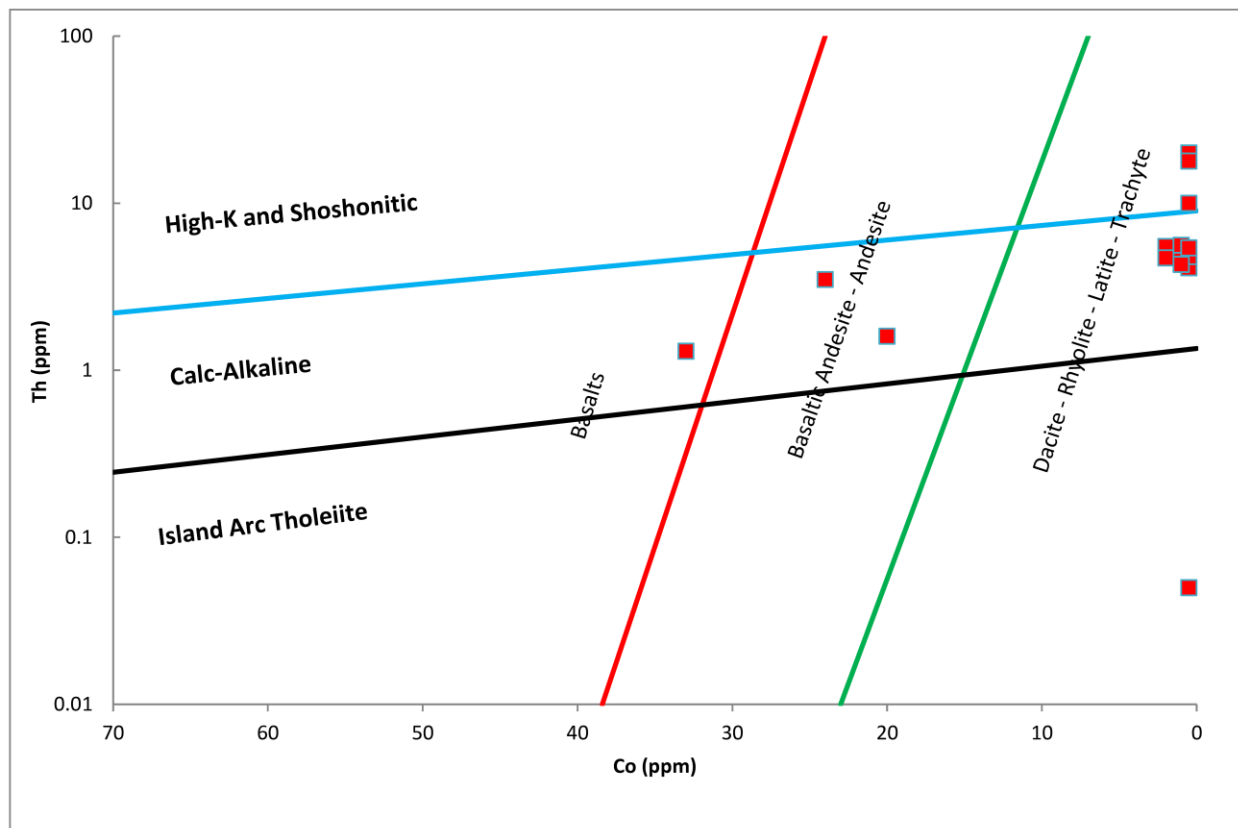


Figure 24. Altered volcanic island rock discrimination diagram based on trace element concentrations in samples from the Palmarejo district (Hastie et al., 2006).

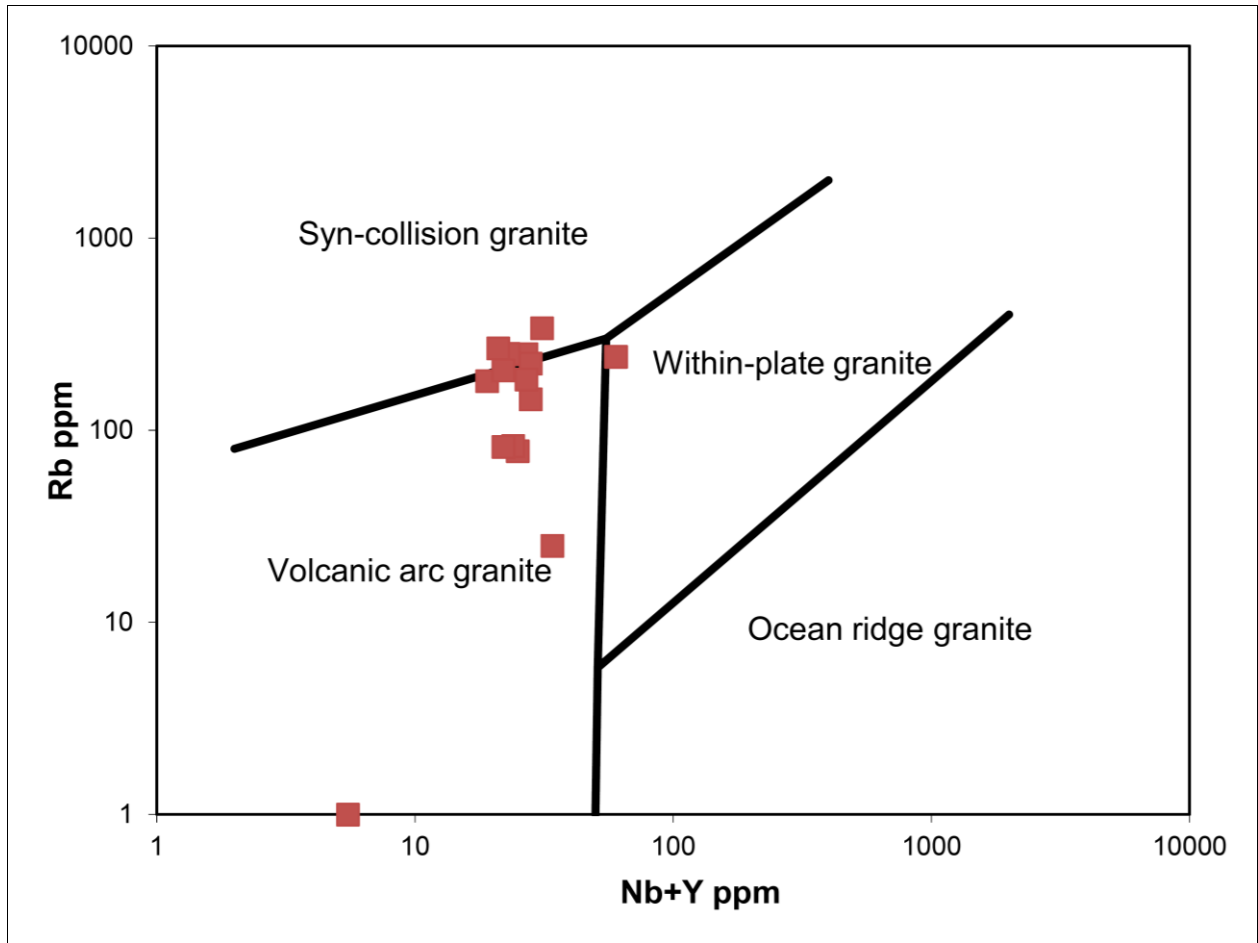


Figure 25. Tectonic setting discrimination diagram based on trace element concentrations in samples from the Palmarejo district (Pearce et al., 1984).

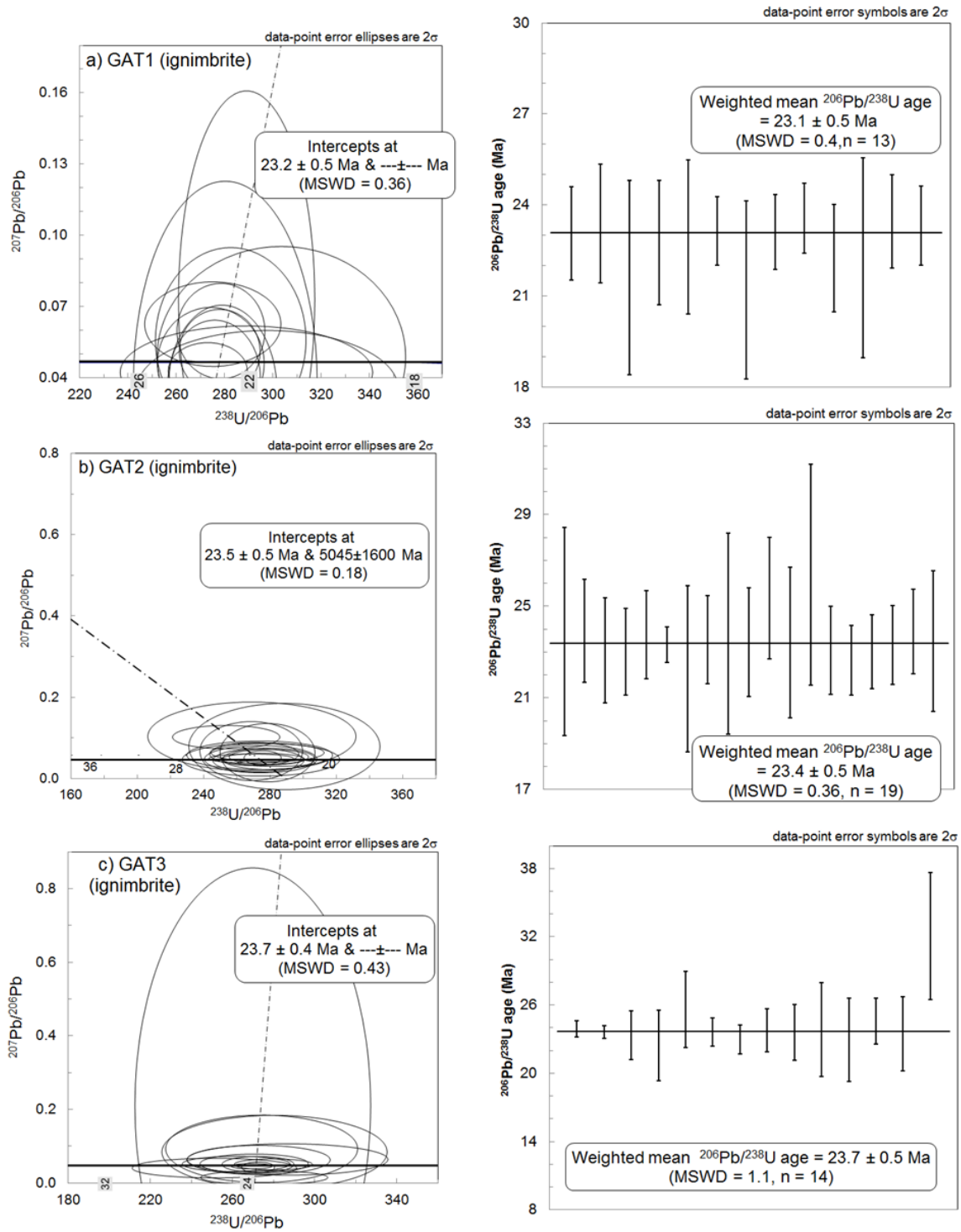


Figure 26 – A-C. U-Pb Tera-Wasserburg plots and weighted mean age plots for the Guerra Al Tirano samples.

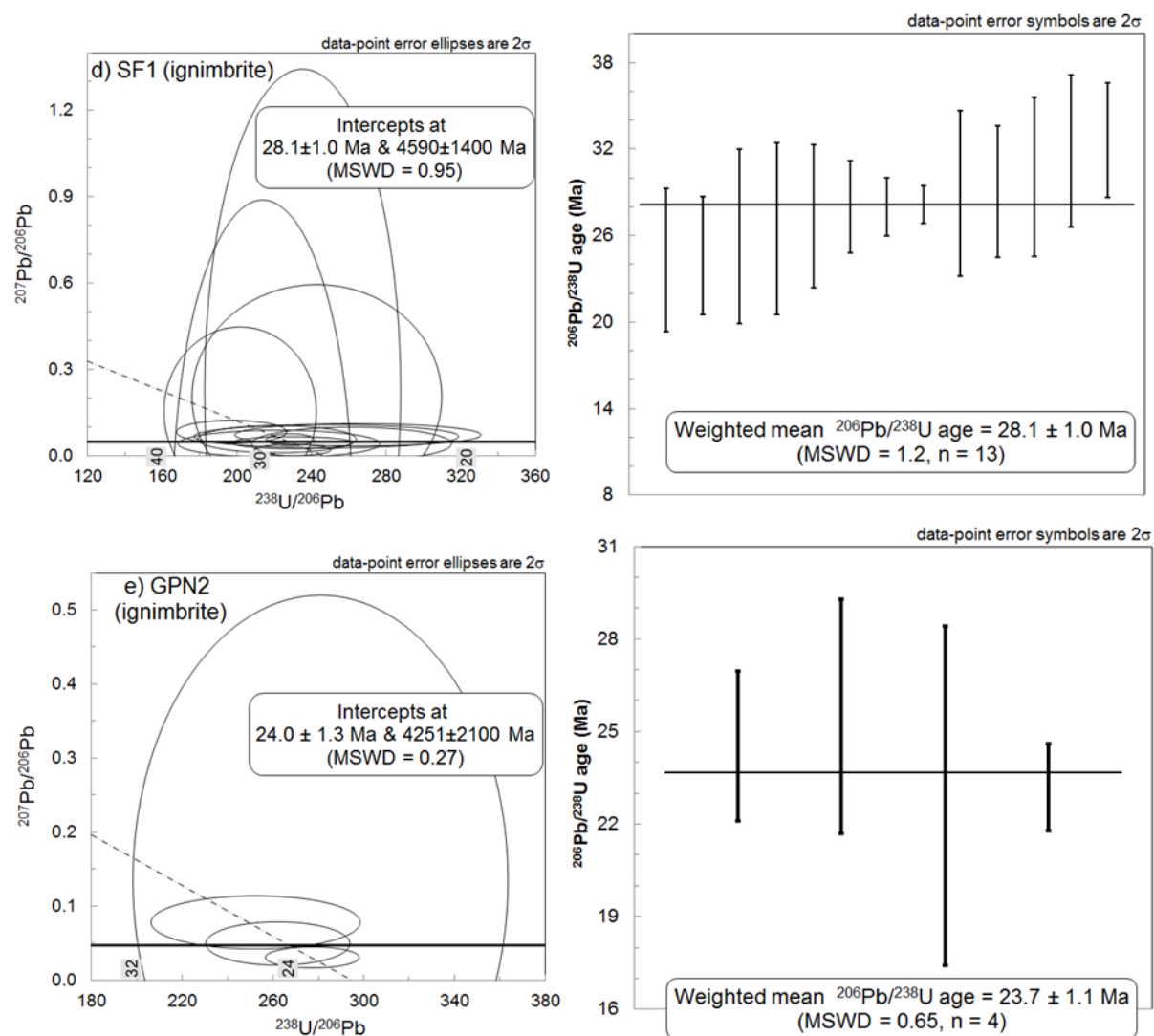


Figure 26 – D-E. U-Pb Tera-Wasserburg plots and weighted mean age plots for the San Francisco (SF1) and Guadalupe Norte (GPN2) samples.

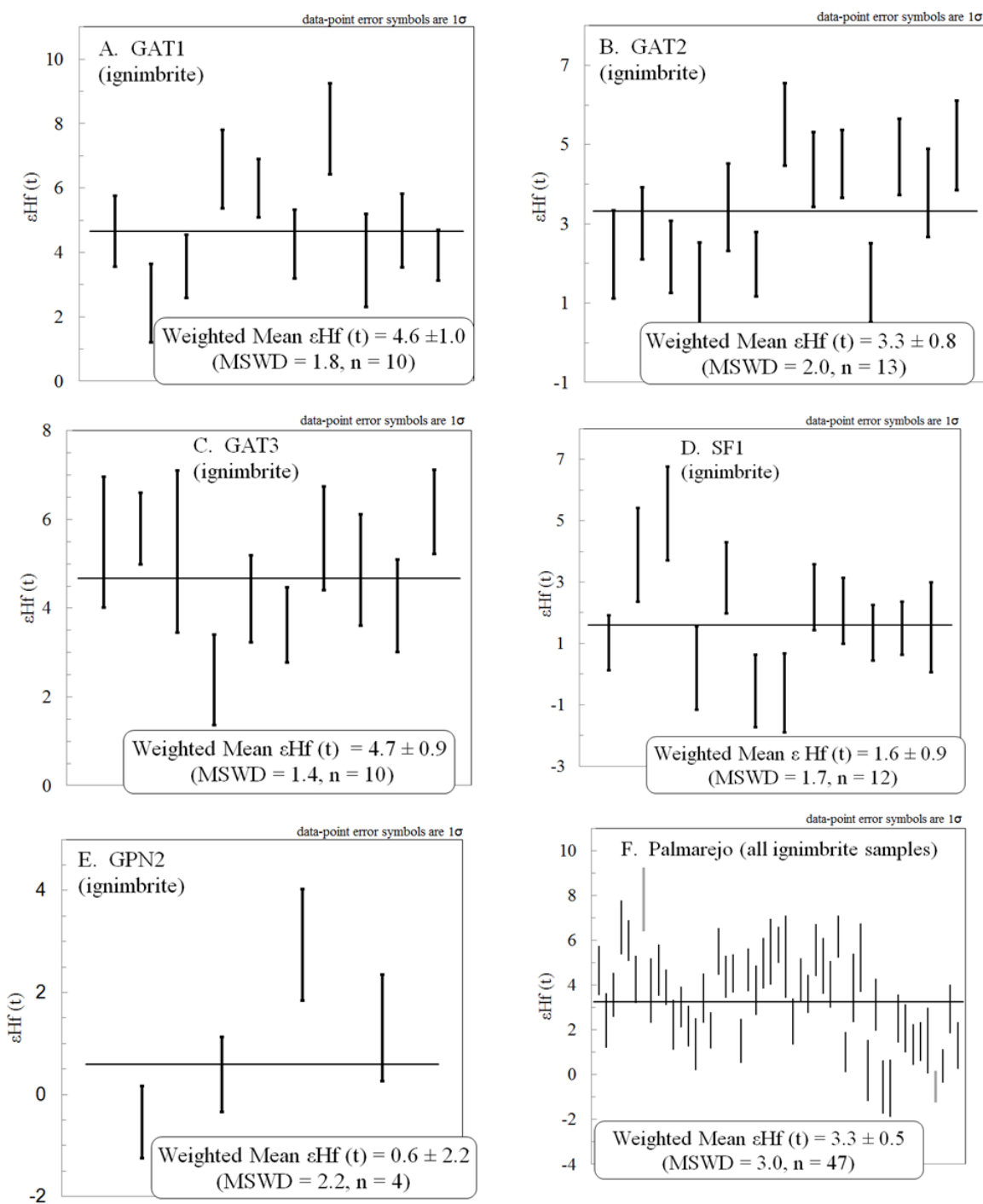


Figure 27 – A-F. Weighted mean $\epsilon\text{Hf}(t)$ compositions of the Guerra Al Tirano (GAT1, GAT2, and GAT3), San Francisco (SF1), Guadalupe Norte (GPN2) and all Palmarejo ignimbrites samples.

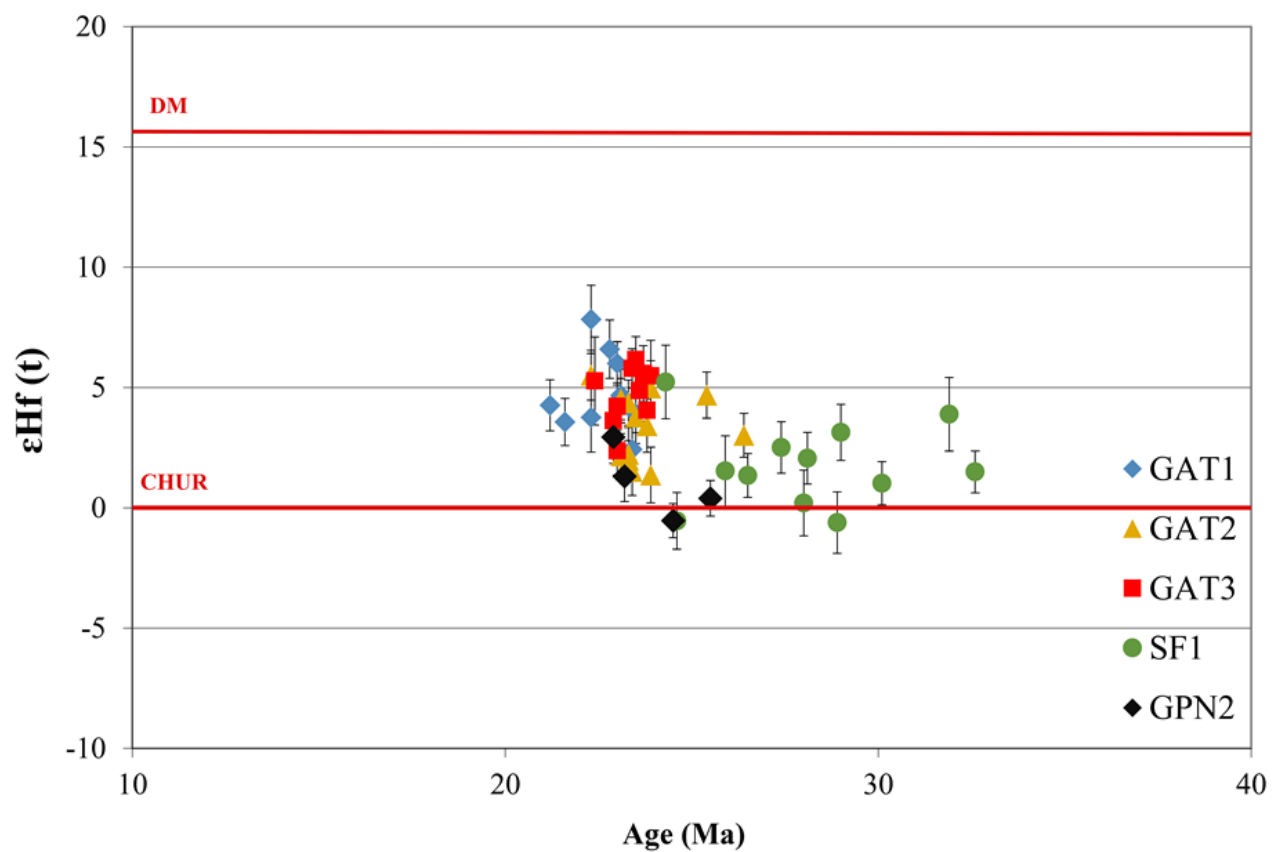


Figure 28. Epsilon Hf (t) against age plot of Palmarejo samples. *DM* – depleted mantle; *CHUR* – chondritic undepleted reservoir.

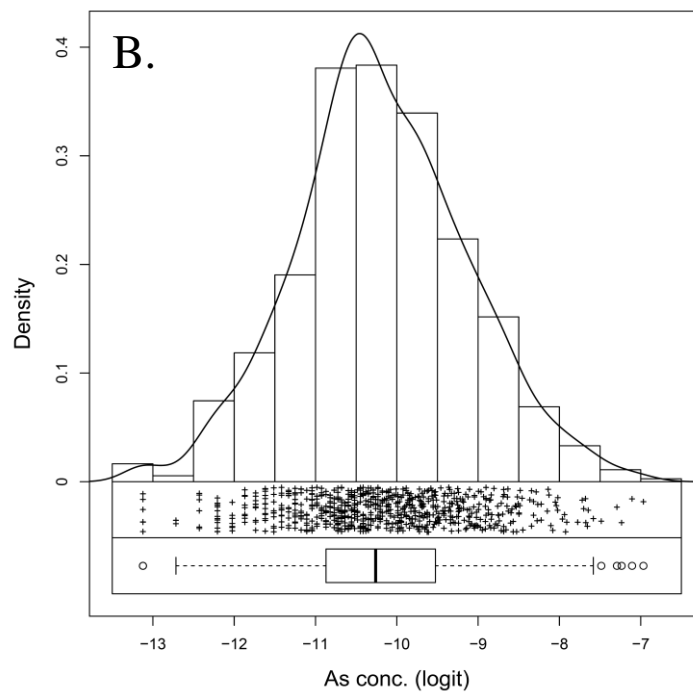
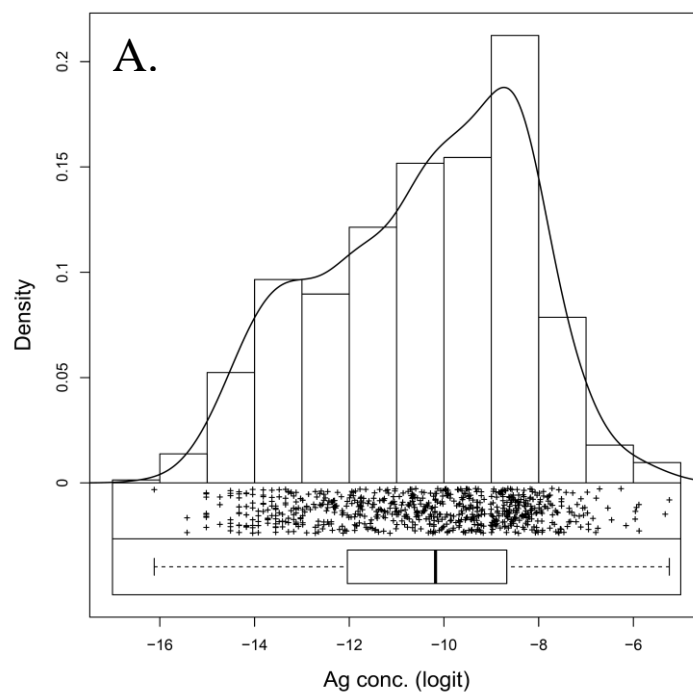


Figure 29 – A-B. Univariate density histograms, one-dimension density plots and box plots for Ag and As logit transformed concentration data (Reimann et al., 2008).

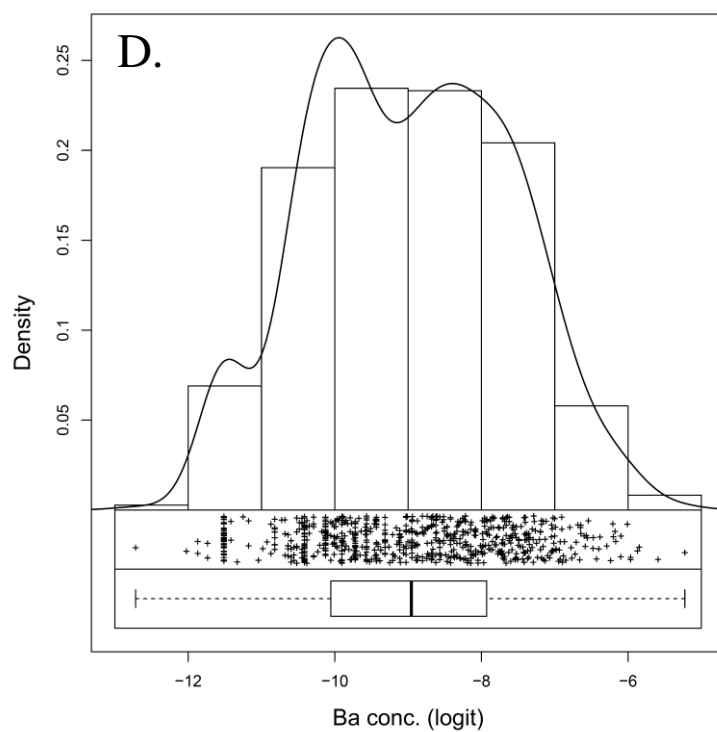
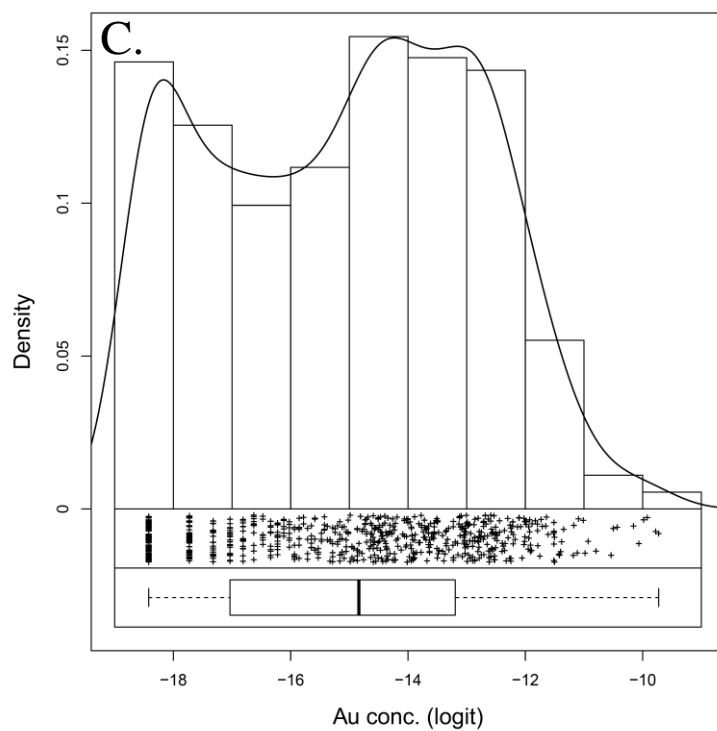


Figure 29 – C-D. Univariate density histograms, one-dimension density plots and box plots for Au and Ba logit transformed concentration data (Reimann et al., 2008).

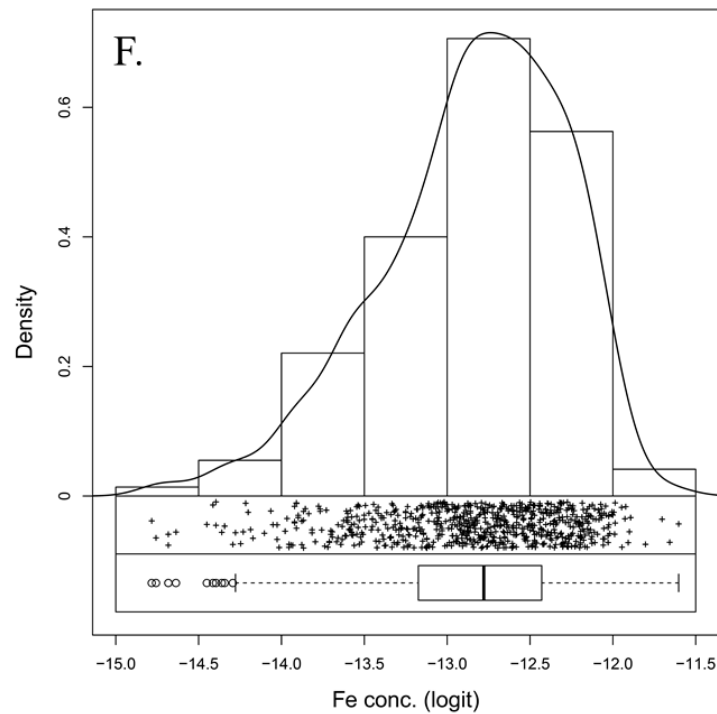
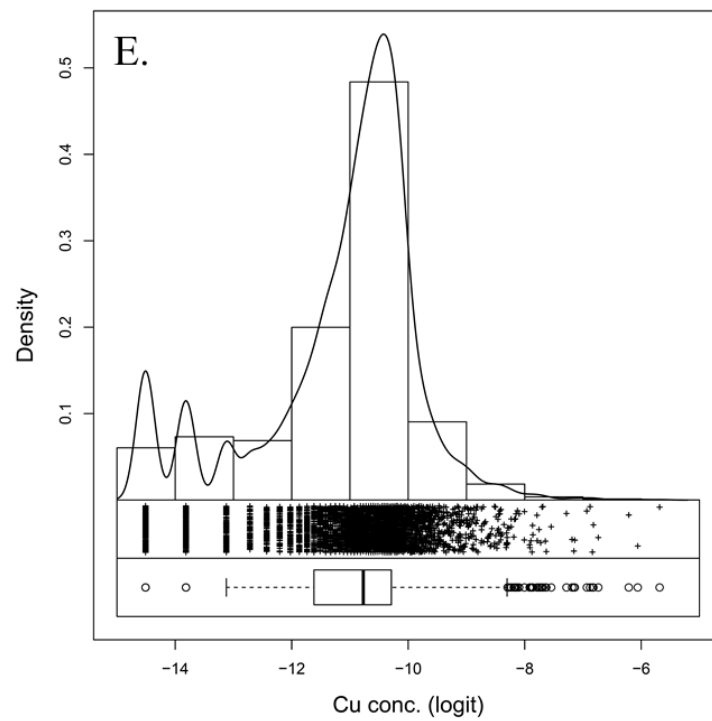


Figure 29 – E-F. Univariate density histograms, one-dimension density plots and box plots for Cu and Fe logit transformed concentration data (Reimann et al., 2008).

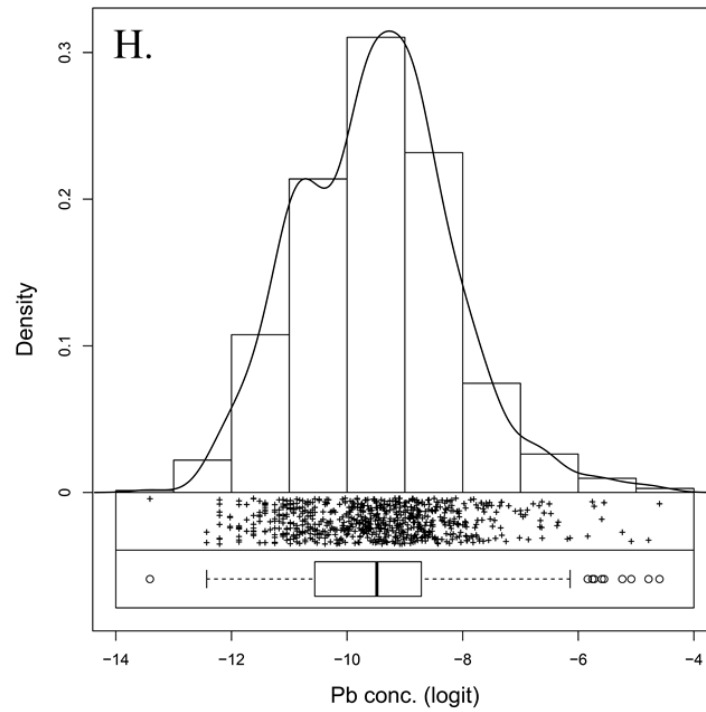
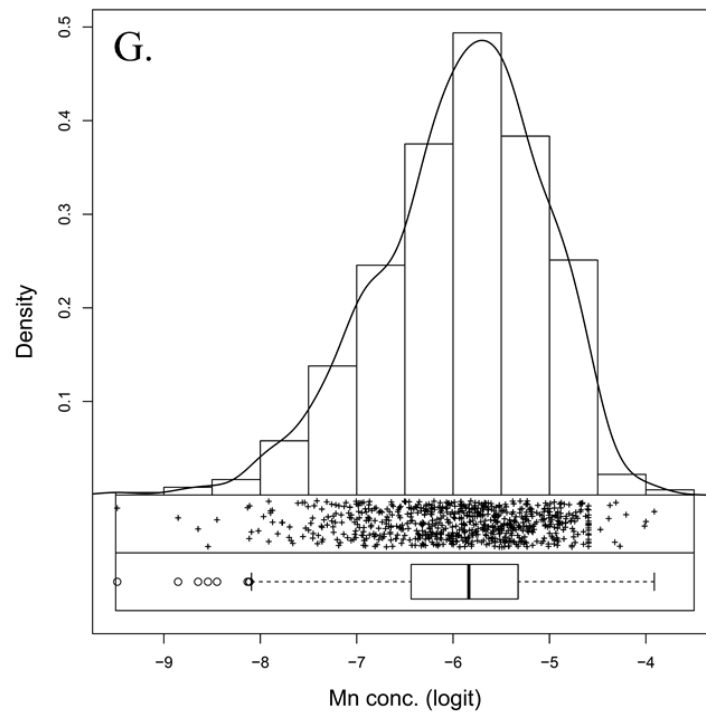


Figure 29 – G-H. Univariate density histograms, one-dimension density plots and box plots for Mn and Pb logit transformed concentration data (Reimann et al., 2008).

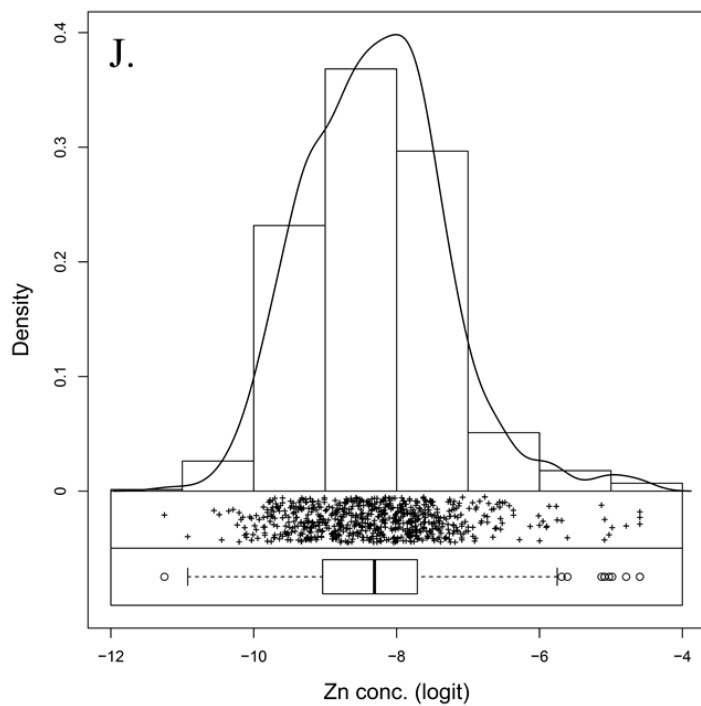
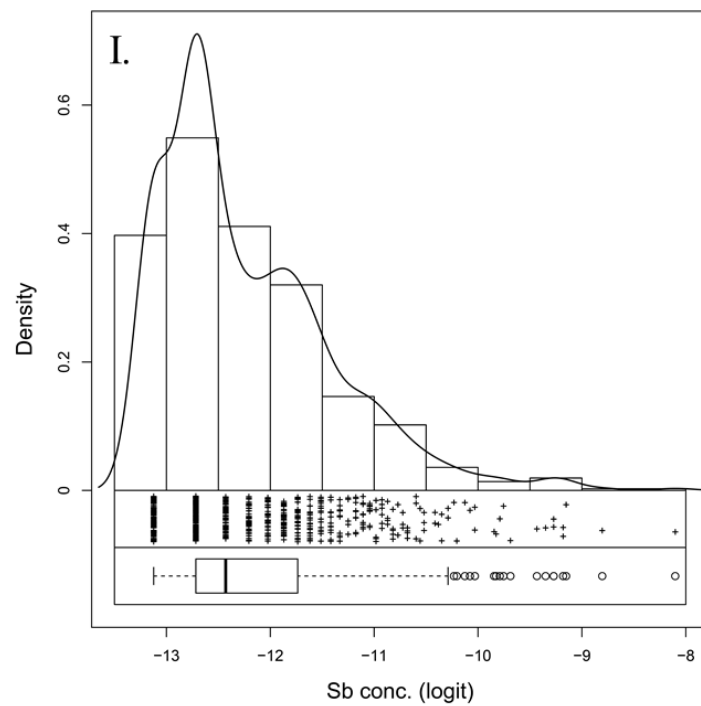


Figure 29 – I-J. Univariate density histograms, one-dimension density plots and box plots for Sb and Zn logit transformed concentration data (Reimann et al., 2008).

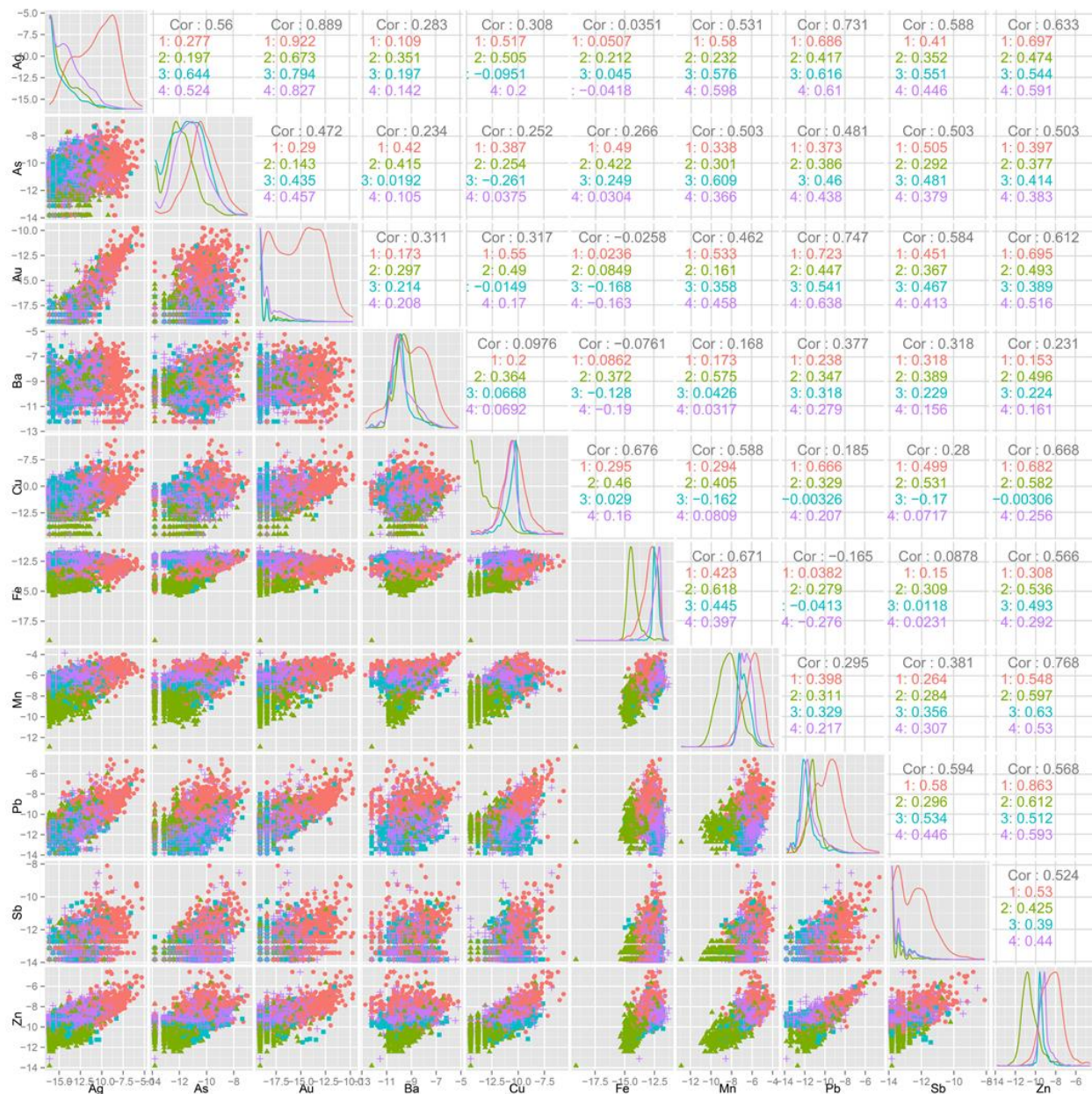


Figure 30. Ten variable scatterplot correlation matrix for logit transformed geochemical assay data from the Independencia vein (Reimann et al., 2008). Red color represents mineralized bodies, green color the rhyolitic porphyry, blue color the andesitic porphyry and purple color andesitic rocks.

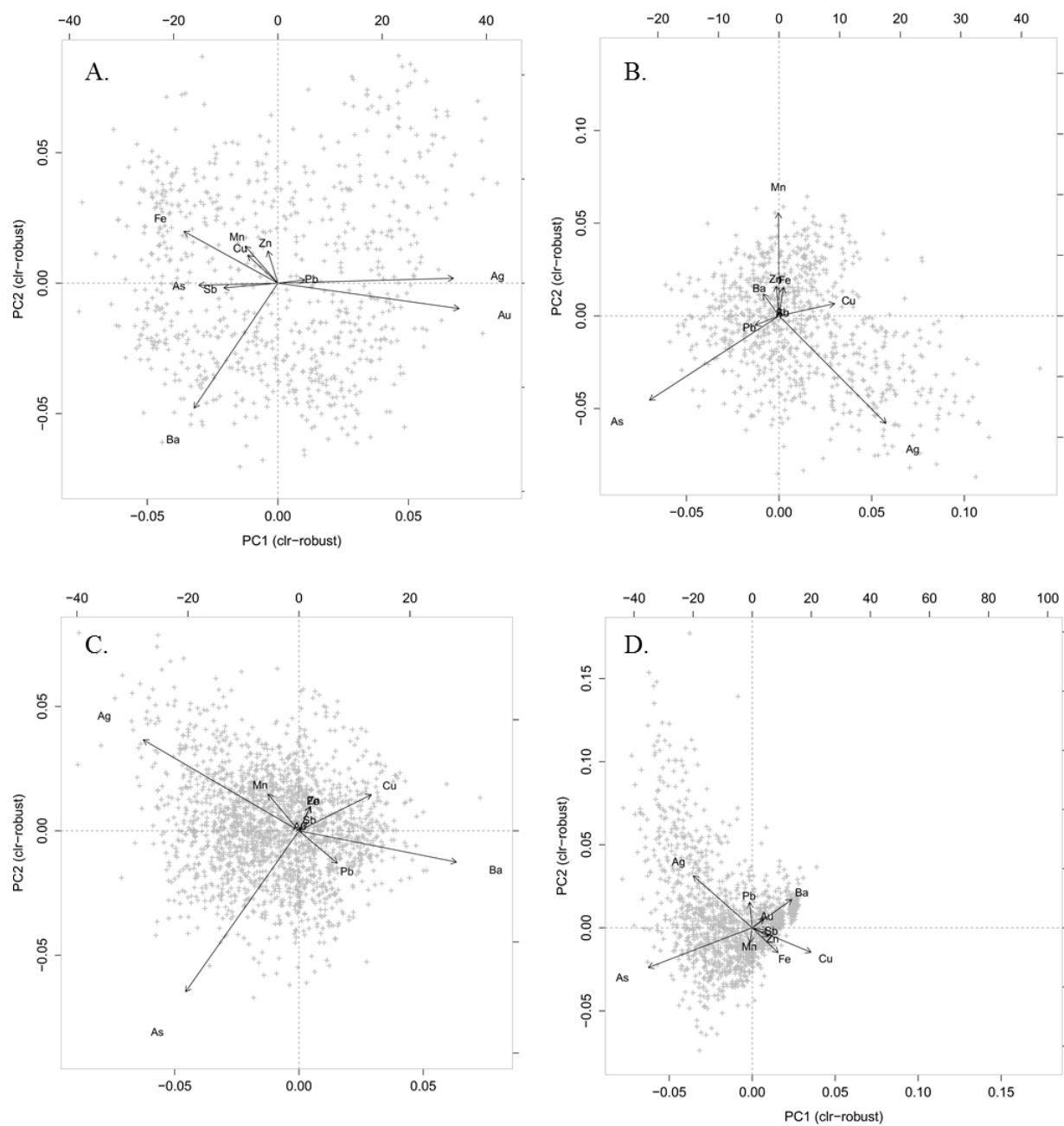


Figure 31 – A-D. Robust Principal Component Analysis (PCA) compositional biplots of centered-log ratio (clr) transformed assay data from the Independencia deposit showing loading vectors (arrows) and scores (gray + signs) (Reimann et al., 2008). A. – mineralized structures. B. rhyolitic rocks. C. andesitic rocks. D. andesitic porphyry.

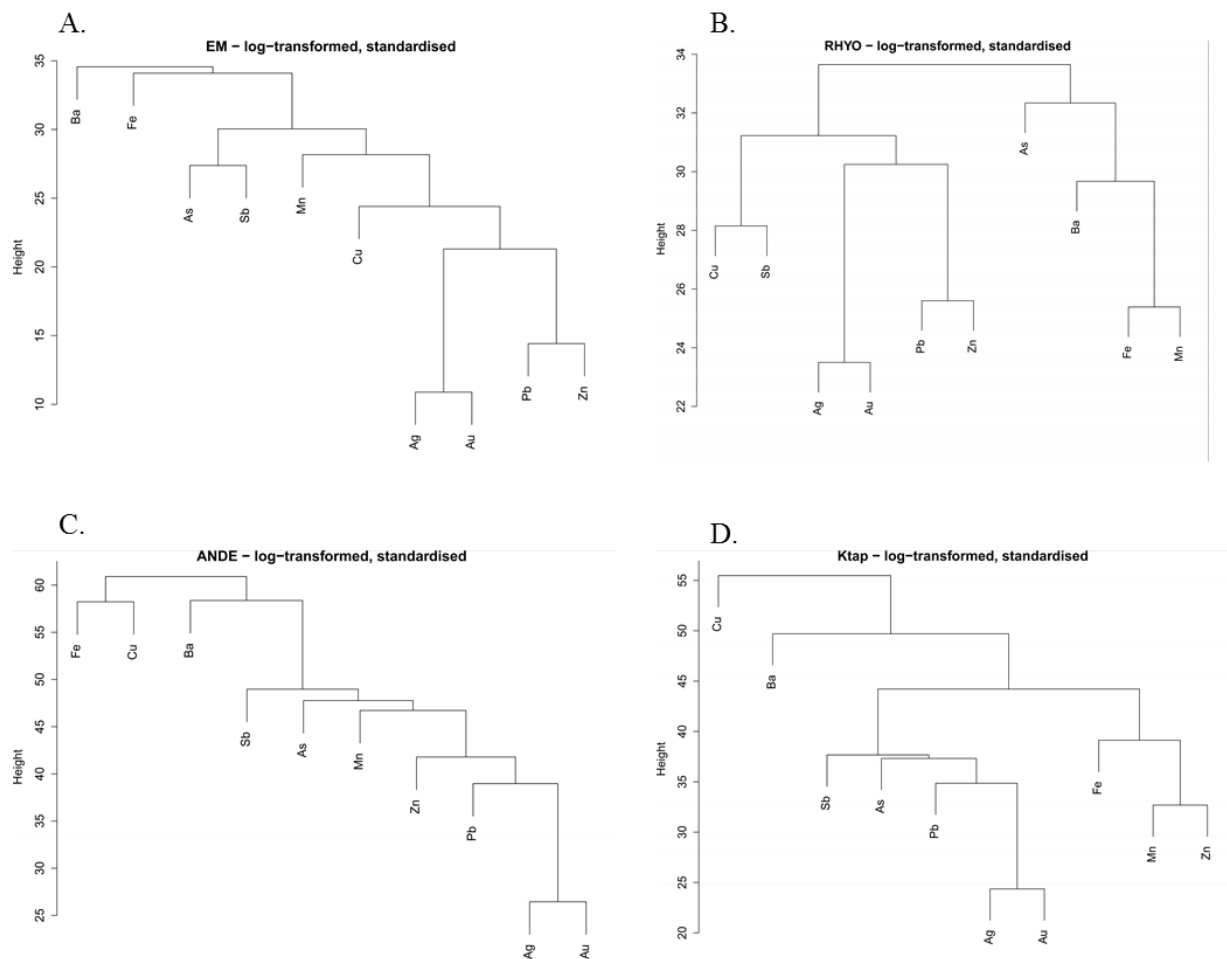


Figure 32 – A-D. Dendrograms for hierarchical cluster analysis of the Independencia vein (Reimann et al., 2008). A. – mineralized structures (EM). B. rhyolitic rocks (RHYO). C. andesitic rocks (ANDE). D. andesitic porphyry (Ktap).

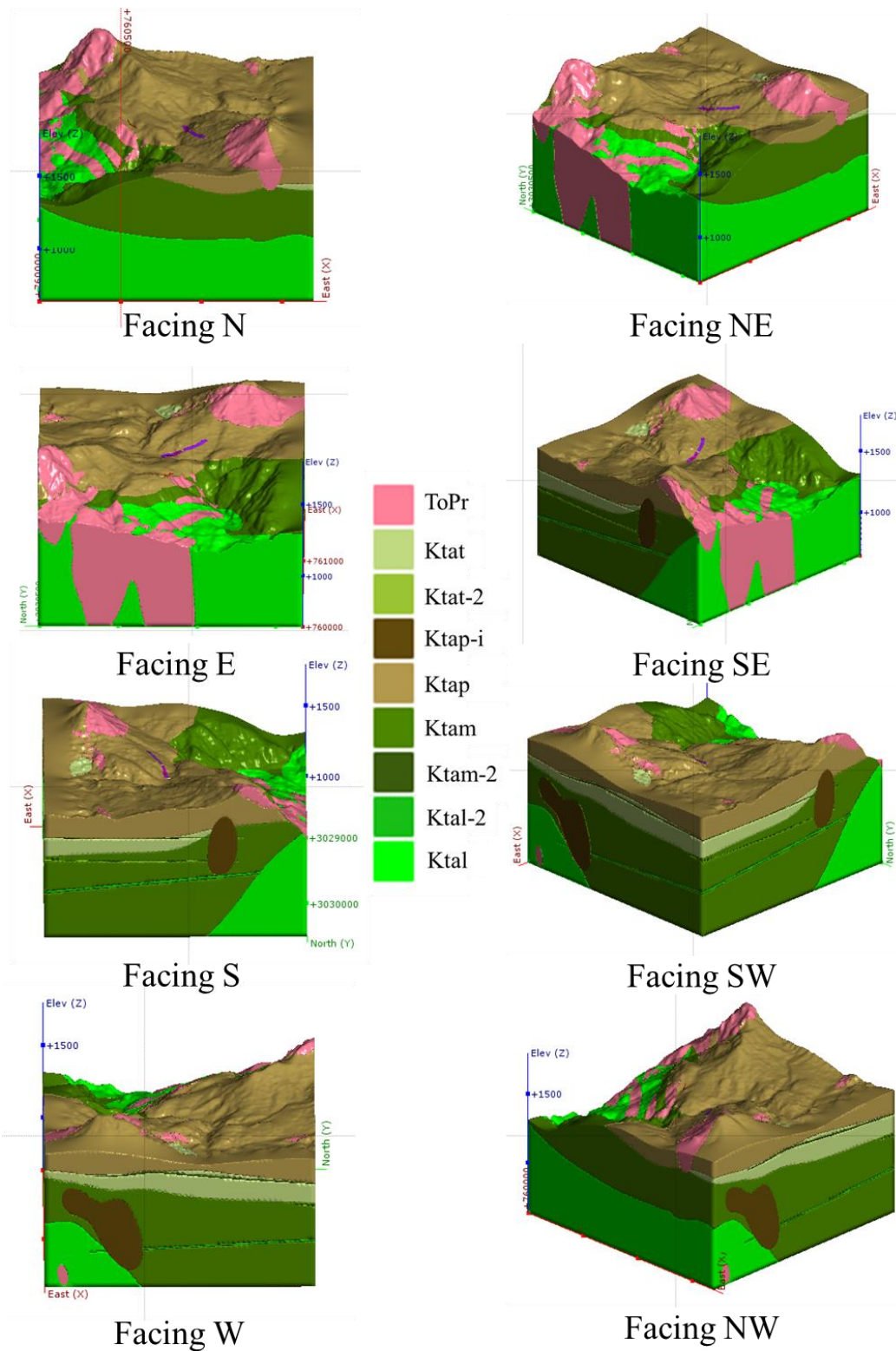


Figure 33. Geologic Model – *ToPr* – porphyritic rhyolites, *Ktat* and *Kat-2* – lithic andesites, - *Ktap* and *Ktap-i* – porphyritic andesites, *Ktam* and *Ktam-2* – amygdular basalts-andesites, *Ktal* and *Ktal-2* – laminar andesites.

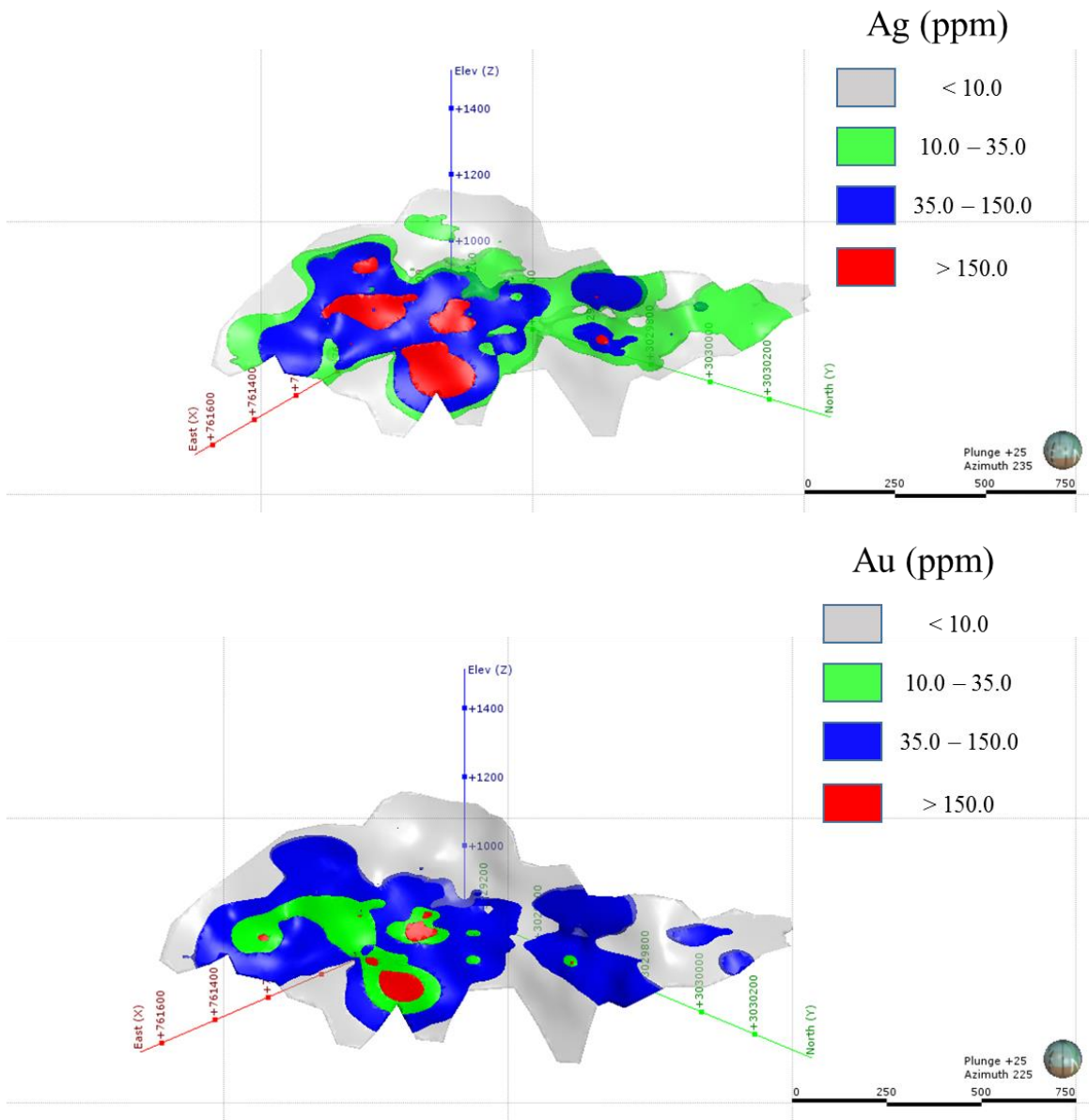


Figure 34. Independencia Ag and Au Interpolation Model, looking SW.

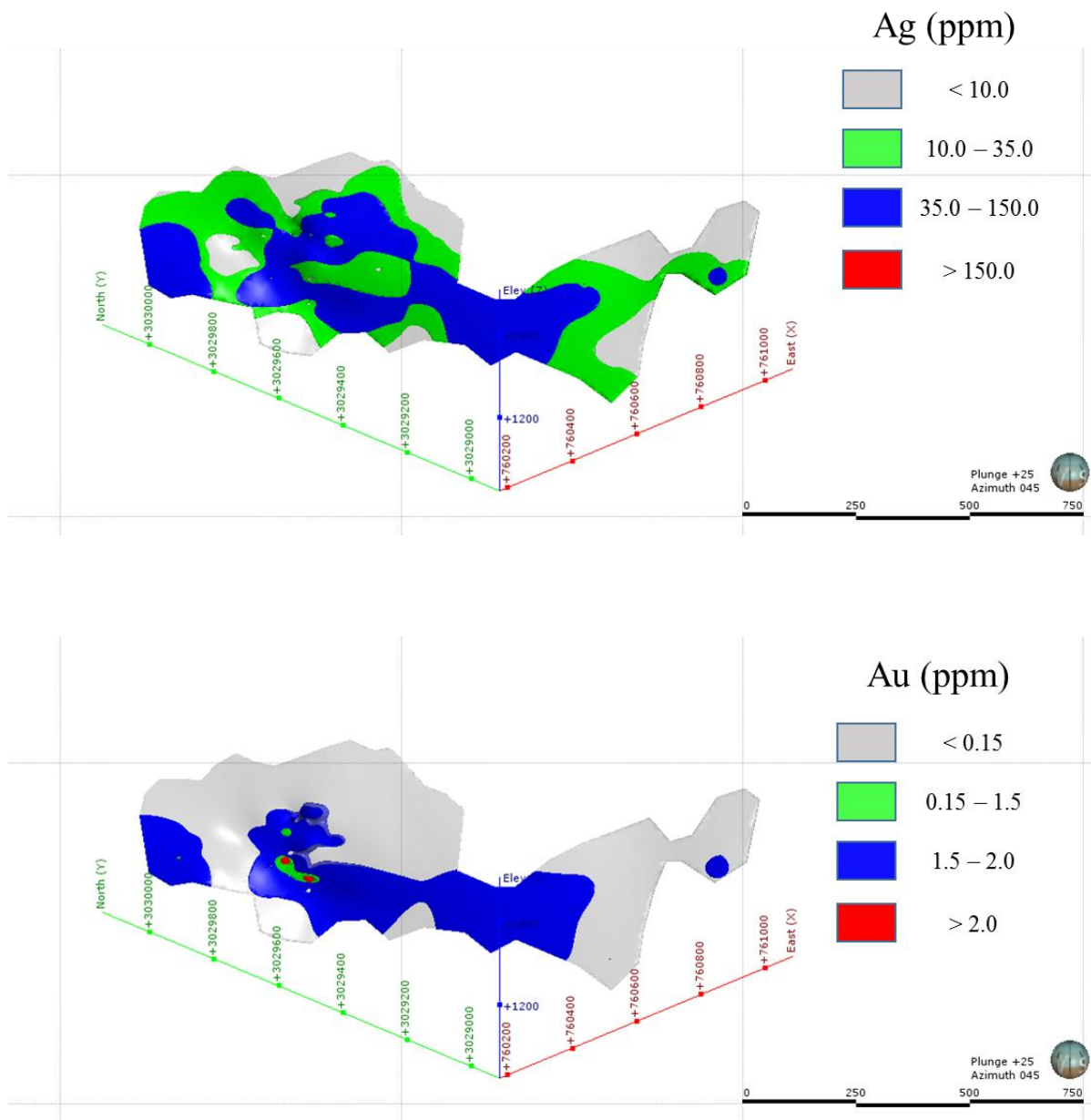


Figure 35. Los Bancos Ag and Au Interpolation Model, looking NE.

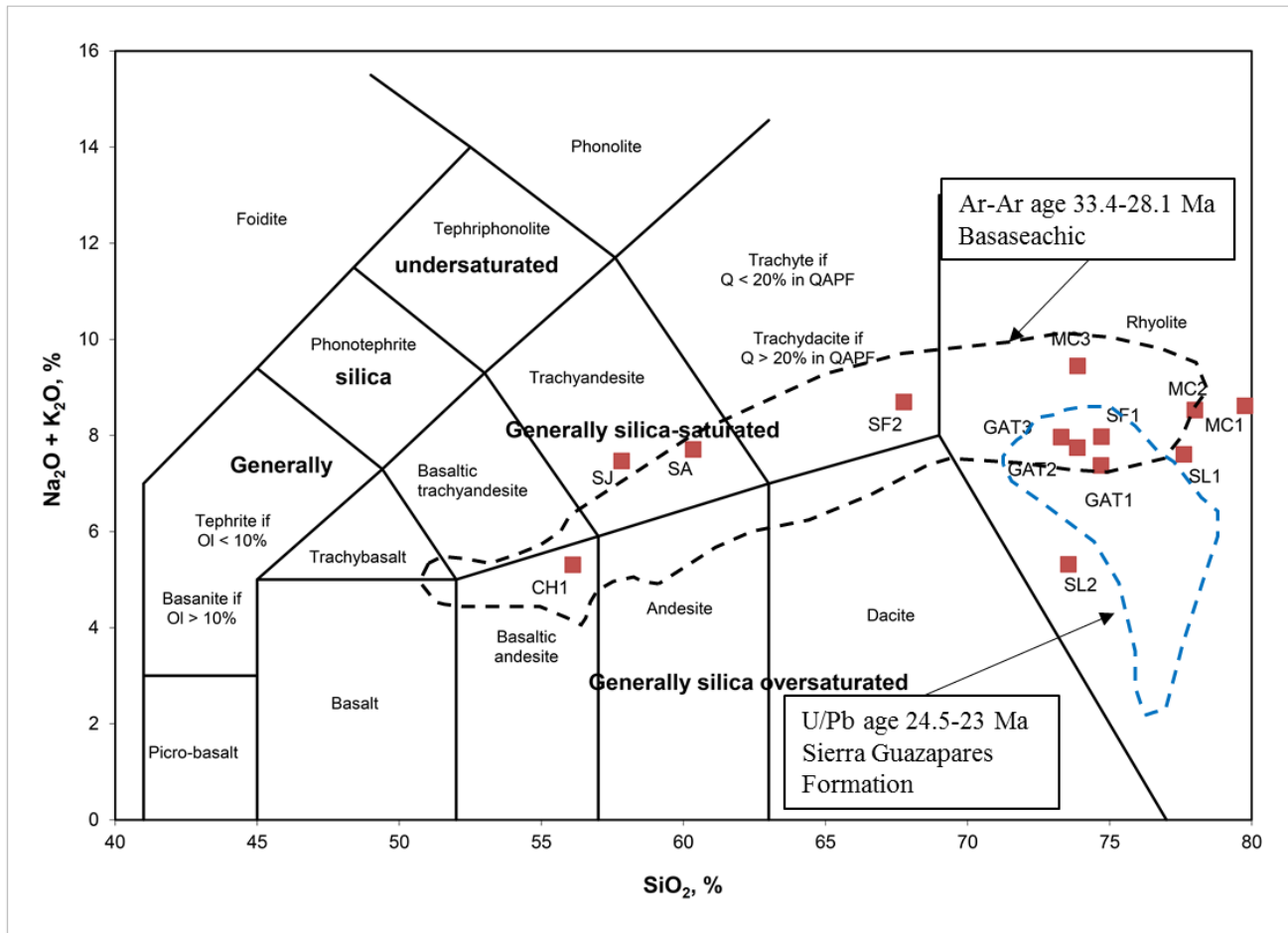


Figure 36. Total Alkali-Silica diagram (after LeBas et al., 1986) showing volcanic rock classifications of samples from the Palmarejo district (red squares). The field of the Sierra Guazapares and Temoris Formation ignimbrites, based on Figure 7 of Murray et al., (2013), is included as a reference (blue dashed line). The field of the main Sierra Madre Occidental rocks, based on Figure 3A of McDowell (2007) is also included (black dashed line).

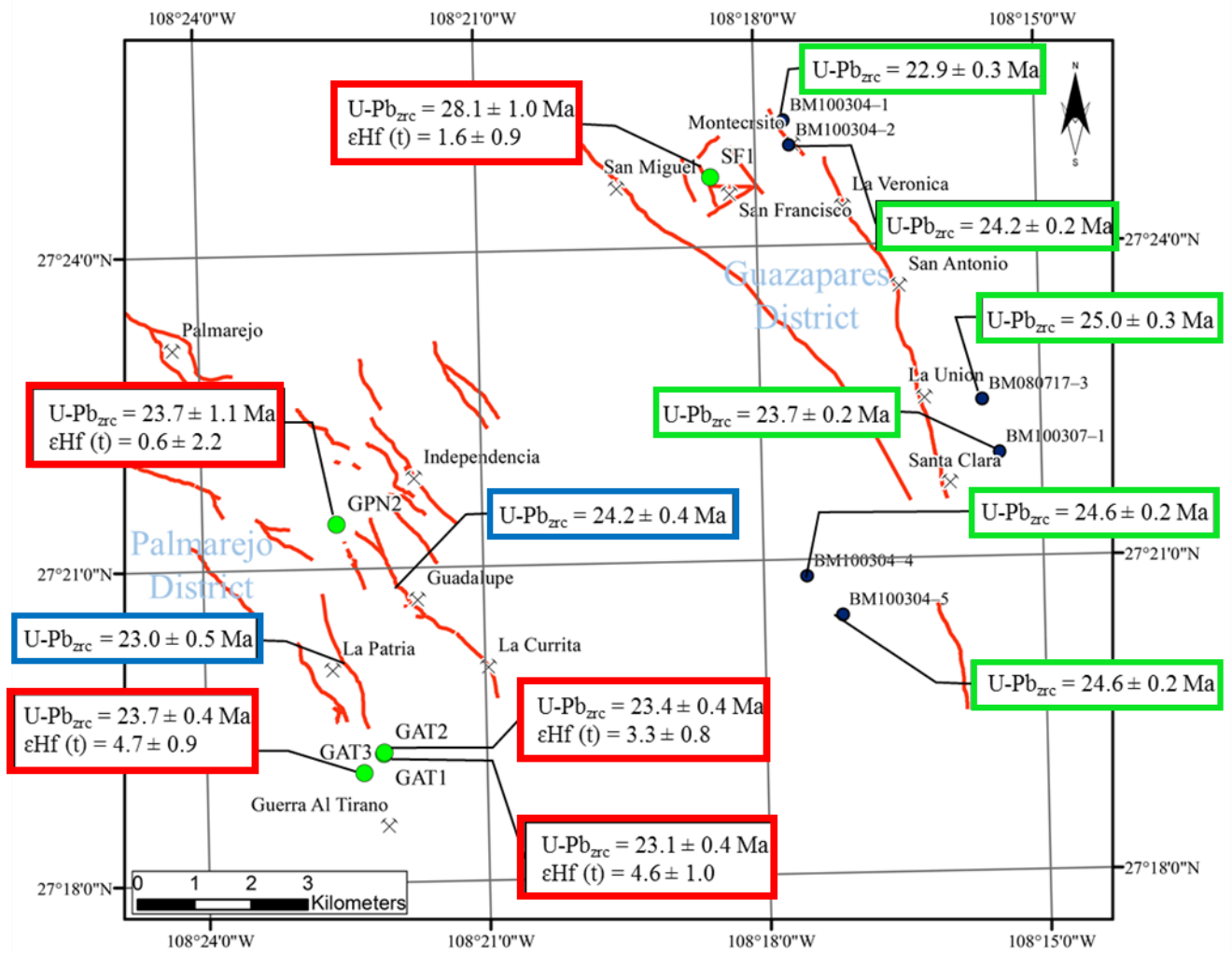


Figure 37. Age data map and $\epsilon_{\text{Hf}}(t)$ across the Palmarejo and Guazapares mining districts (red boxes – this study). Age data from Galvan-Gutierrez (2012) (blue boxes) and Murray et al. (2013) (green boxes).

Post-Laramidic extension related to the ignimbrite flare-up 28 Ma – 23 Ma

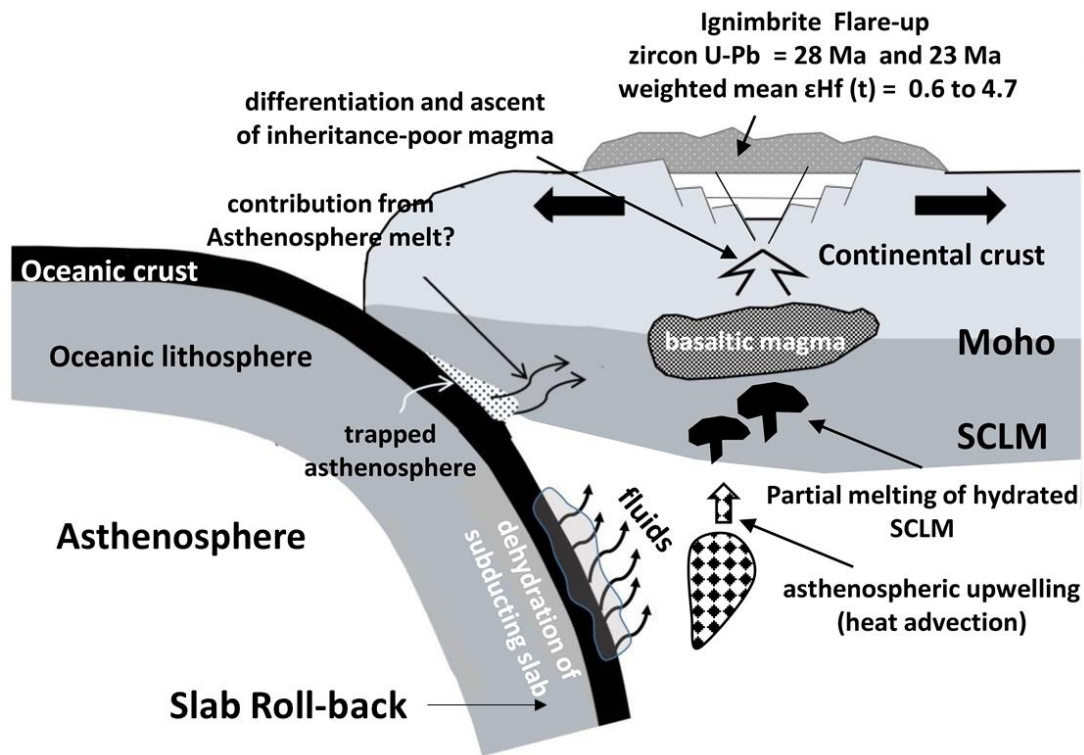


Figure 38. Slab roll-back schematic model for extension, asthenospheric upwelling, partial melting of the sub-continental lithospheric mantle (SCLM) and differentiation of basaltic magma to generate the ignimbrite flare-up.

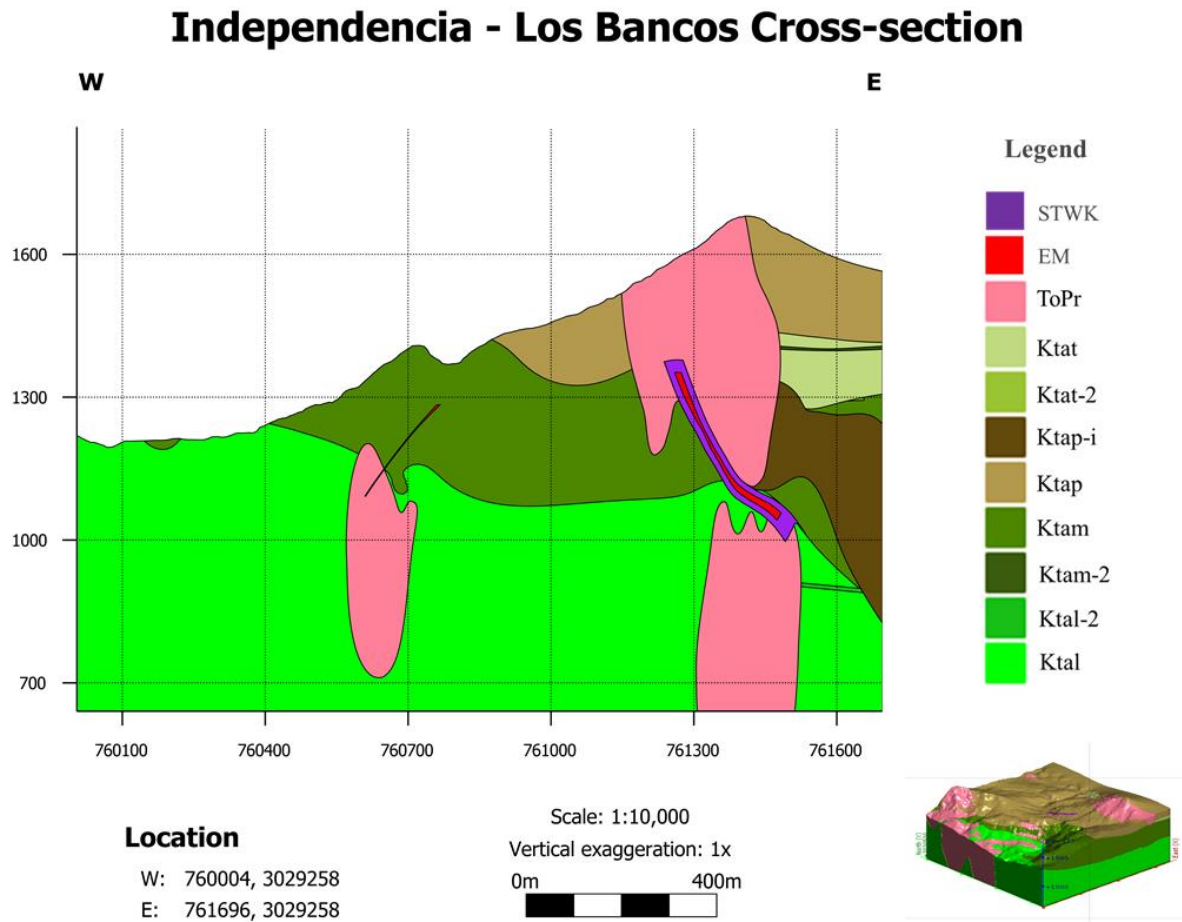


Figure 39. Cross-section of the Independencia – Los Bancos showing cross-cutting relationships of the rhyolitic porphyry (ToPr) with respect to the Independencia and Los Bancos veins. *STWK* – stockwork; *EM* – mineralized structures; *ToPr* – porphyritic rhyolite; *Ktat* – lithic andesites; *Ktap* – porphyritic andesite; *Ktam* – amygdular basaltic andesites; *Ktal* – laminar andesites.

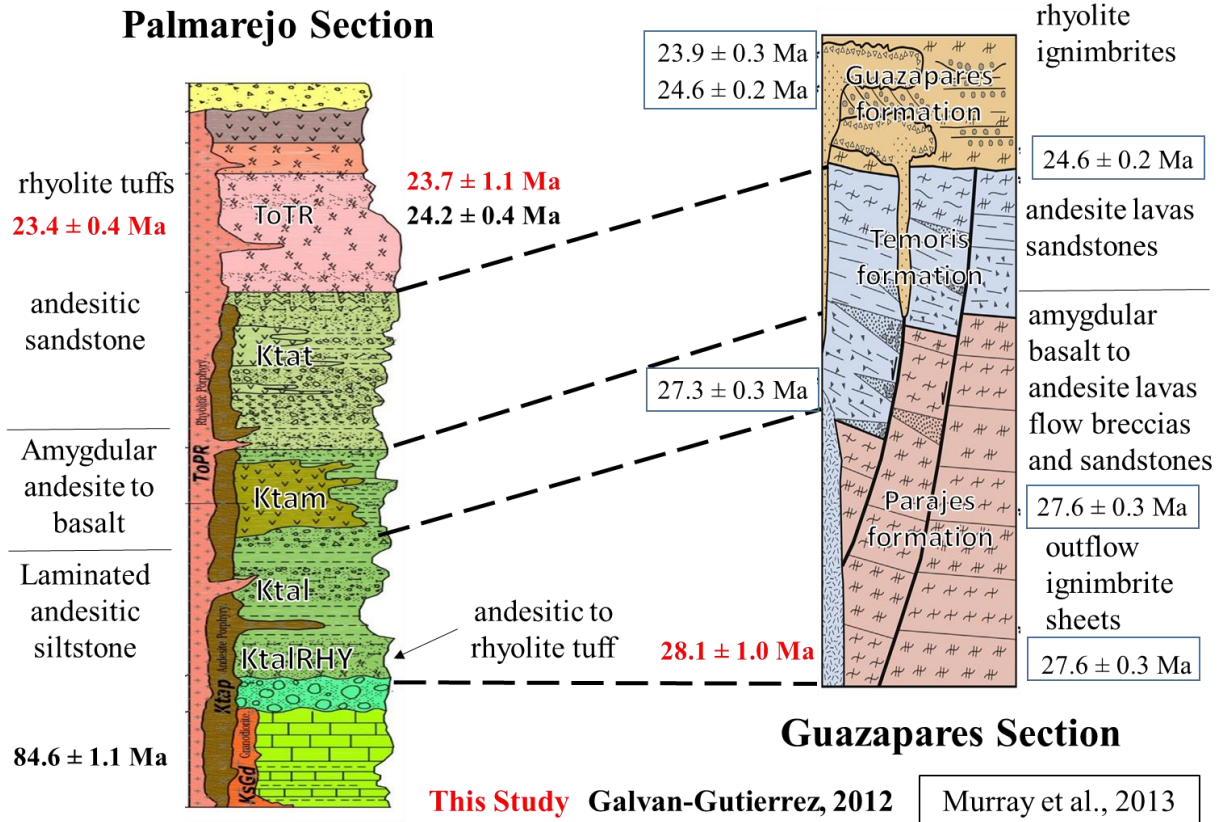


Figure 40. Stratigraphic column correlation between the Guazapares and Palmarejo district suggesting the Upper Volcanic Supergroup (UVS) as the host rock for mineralization based on zircon U/Pb age data from Murray et al. (2013).

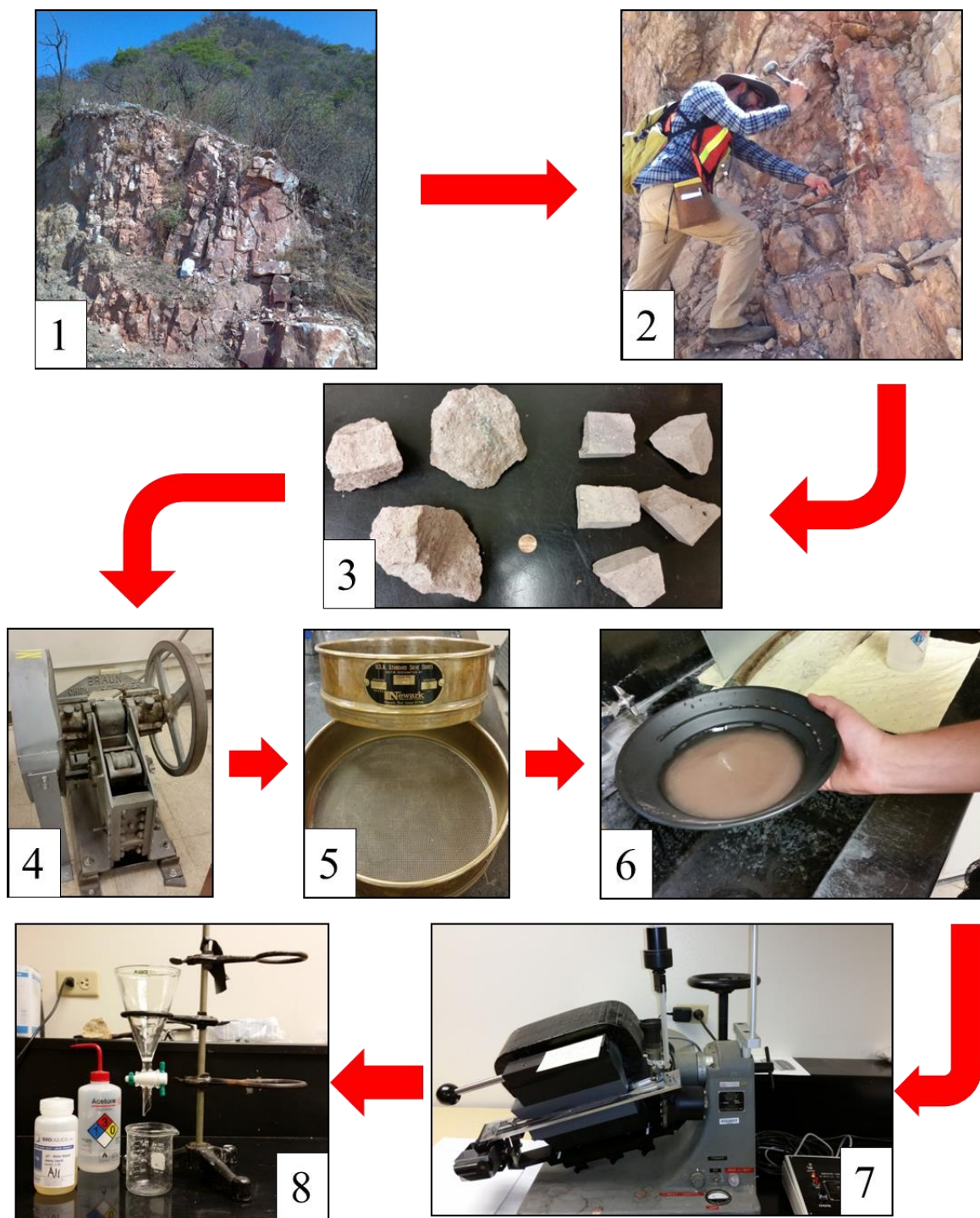


Illustration 1. Sample processing steps for zircon extraction. 1) outcrop selection, 2) sampling fresh rock, 3) cutting sample, 4) crushing rock, 5) 500 µm mesh sieve, 6) gravity separation, 7) magnetic mineral separation, and 8) heavy-liquid separation.



Illustration 2. LaserChron laboratory of the University of Arizona. Laser Ablation Induced Coupled Plasma Mass Spectrometry (LA-ICP-MS) analytical instrument. 1) laser beam focused on the sample surface to generate fine particles, 2) ablated particles are then transported to the secondary excitation source of the ICP-MS instrument for digestion and ionization of the sampled mass. The excited ions in the plasma torch are subsequently introduced to a mass spectrometer detector for both elemental and isotopic analysis.

Vita

Arturo Ramirez was born in Delicias, Chihuahua in Mexico. He earned his geology bachelor's degree from UTEP in 2013, and enrolled for the master's program in that same year. During his graduate studies, he was the teaching assistant for the mineralogy and petrology courses, was involved in various organizations, and received several scholarships from the geology department. Arturo served as the president of the Society of Economic Geologists (SEG) UTEP Student Chapter from 2014-2015, in which he successfully organized field trips, hosted industry guest lectures, and promoted the geosciences to elementary students and the cub scouts of El Paso through various hands-on activities. Arturo was selected by the SEG to participate in the SEG Foundation student field trip to Copiapó, Chile in 2015 and learn about the metallogeny of Northern Chile, which enhanced his abilities to identify characteristics of mineral deposits. He was also funded by the SEG to present his research in the 2015 SEG annual conference in Hobart Tasmania, Australia. Arturo plans on working for mining companies to continue to grow as a geoscientist in the industry sector, as well as contribute to the community by hosting lectures regarding economic geology. Pursuing a PhD is also in Arturo's future goals, as he would like to publish his findings.

Permanent address: 7133 North Mesa Street Apt. 143

El Paso, Texas, 79912

This thesis was typed by Arturo Ramirez.